Energy Measurement Capabilities of the LEDA Cosmic Ray Detector

KAVITA MURTHY

Department of Physics

McGill University, Montreal, Québec

21/3/88

A thesis submitted to the Faculty of Graduate Studies and Research in partial fulfillment of the requirements for the degree of Master of Science in Physics.

Energy Measurement Capabilities of the LEDA Cosmic Ray Detector

TABLE OF CONTENTS

ABSTRACT iv

ACKNOWLEDGEMENTS vi

1 INTRODUCTION 1

2 THE COSMIC RAY DETECTOR 32

(a) General Considerations 32

The Scintillator

The Photo-tube

Light Collection System

(b)Design and fabrication of counter 36

(c) The Final Detector Design 45

(d)Resolution versus PMT size 55

3 THE LEDA ARRAY 39

(a) Location and General Layout 59

(b) The Counters 62

(c) The Electronics 66

(d) Computer Program for Data Taking 77

(e) Preliminary Data Collection 80

(f) Description of the Data Set Used 85

4 DATA ANALYSIS 90

(a) The Maximum Likelihood Method 93

(b) Maximum Likelihood Technique Applied to Shower Data . 96

(c) Monte Carlo of Fitting Routine 99

(d) Analysis of Shower Data 113
(e) Differential Size and Energy Spectra 114
(f) Discussion of Results 122

5 CONCLUSION 129

REFERENCES 131

ABSTRACT

Over the years cosmic ray studies have yielded many new and interesting secrets about the Universe and the Galaxy. Studies of cosmic γ-rays provided direct information about the sources that produce them. Air shower arrays are a popular way way of studying extensive air showers produced by cosmic rays in the 10^{14}eV to 10^{20}eV range. The Large Experiment to Detect Air showers(LEDA) array consists of 19 liquid scintillator particle detectors occupying an area of 20,000m^2. In this thesis, the development of the detector prototype and the performance of the array are described. Finally, the preliminary results consisting of the size spectrum of cosmic rays are presented. From studies of the performance of various detector arrangements, the final scintillator dish with a graded bottom was evolved. The array spacing was chosen to give maximum collecting area for the number of detectors used. The final size spectrum obtained between $10^{4.5}$ and and $10^{16.0}$ corresponding to energies of approximately $10^{14.5}$ and $10^{16.0}$eV shows evidence of the knee, a point where the slope of the spectrum changes by 1.

RESUME

A travers les années, les études de rayons cosmiques ont révelé maints secrets nouveaux et intéressants à propos de l'univers et de la galaxie. Les études de rayons gamma cosmiques donnent de l'information directe sur leurs sources. Les matrices de détecteurs sont un moyen populaire pour étudier les gerbes atmosphériques étendues produits par les rayons cosmiques primaires avec des énergies entre 10^{14}eV et 10^{20}eV, L'expérience LEDA consiste en 19 détecteurs de particules fait de scintillateur liquide et occupe une superficie d'environs 20 000m^2. Dans cette thèse, le dévelopment d'un détecteur prototype et la performance de la matrice sont décrits. Finalement, des résultats préliminaires sur le spectre des tailles des rayons cosmiques primaires sont présenté. A partir d'études sur une variété de configurations de détecteurs, une cuvette pour le scintillateur avec un fond gradué a été évolué. La distance inter-détecteur a été choisi pour donner une surface de collection maximum pour le nombre de détecteurs. Le spectre de tailles obtenu était entre $10^{4\ 5}$ et 10^{6} particules, et démontre le "genou", un point où la pente du spectre change d'unité.

ACKNOWLEDGEMENTS

I am sincerely grateful to my supervisor Dr. David Hanna, for his helpful guidance during the course of this project.

I wish to express sincere thanks to all my colleagues who were actively involved in the in the LEDA project, especially to Sandy Bultena (M.Sc. student) for always being helpful. My thanks to Paul Mercure for his valuable help with the computer hardware and software. Special thanks are due to Robert Nowac for his excellent art work and his help in the construction of the detectors. Thanks also to Peter Neelin (M.Sc. student) for his help in translating the abstract and his helpful tips about Tex.

I wish to thank the Chairman of the Department of Physics, Dr. S. K. Mark, for providing the necessary facilities and permitting me to submit my work in the form of a thesis. My gratitude to McGill University for enabling me to come to Canada as a student to pursue my studies.

Lastly but most importantly, I wish to thank my husband Kishore for his unfaltering moral support throughout these years without which none of this would have been possible.

1. INTRODUCTION

General

Before the advent of the era of big accelerators, cosmic rays were the only particle beams that the particle physicist had, to study high energy interactions. Most of the major discoveries concerning cosmic rays were made in the first half of this century. Interest in these studies was greatly increased when astrophysicists realised what an excellent tool they had for studying the numerous sources of radiation in the universe. The small scale experiments gave way to larger ones involving detector arrays consisting of a large number of detectors occupying large areas, studying details about the arrival direction and the energy of the particles in the hope that these experiments would tell us more about the mysterious sources of cosmic rays that radiated so constantly and furiously.

Section 1(a): Definitions

Cosmic rays are highly energetic particles and radiation that are extra -terrestrial in origin. Their energies extend from thermal up to 10^{20}eV where there is some evidence for a cutoff[1]. Cosmic rays are classified into two: **primary and secondary cosmic rays**. Primary cosmic radiation are particles that reach the earth from their sources. Secondary radiation are the product of the interaction between primary radiation and nuclei in the atmosphere. Primary radiation consist mainly of positively charged particles like protons(Hydrogen nuclei), alpha particles and other heavier nuclei. A small fraction of cosmic ray primaries, about $\frac{1}{1000}$ths are highly energetic γ-rays. **Cosmic ray showers** are triggered when a cosmic ray of very high energy enters the atmosphere. Secondary cosmic radiation are the constituents of these showers. The lateral spread of such showers can extend beyond 1km– leading to the term **Extensive Air Showers** or EAS. The development of EAS will be described in detail in a later section of this chapter.

The energy unit used in cosmic ray studies is electron volt(1eV= 1.602× 10^{-19}Joules). The energy of a cosmic ray shower refers to the energy of the primary that precipitated it *at the top of the atmosphere.* Gamma rays of energies $>10^{14}$eV are called ultra-high energy gamma rays. Gamma ray primaries between 10^{11}eV and 10^{14}eV are called very high energy cosmic rays and those of lower energy are called high energy gamma rays. Thickness of matter in cosmic ray studies is expressed in terms of **mass thickness** which expresses the thickness of matter as the mass of a column of unit area through that layer. The unit of mass thickness is grams per square centimeter. In these units the thickness of the atmosphere is 1000 g cm^{-2}. The **Radiation Length** X_0 of a medium is defined as that thickness of the medium which reduces the mean energy of a beam of electrons by a factor e. In terms of radiation length the atmosphere is 27 radiation lengths in depth and the radiation length of air is 37 g cm^2. The **Critical energy** E_c is defined as the energy at which average radiation loss and ionization energy loss for fast electrons are equal. The **Moliere unit** is a measure of the lateral spread of a shower in a medium. In all material, this spread is of the order of one Moliere unit given by

$$R_m = 21\,\frac{X_0}{E_c}.$$

In air at sea level, the Moliere unit is 70-80 meters.

Amongst the various phenomenon associated with cosmic rays, there are three that require elaboration because of the important roles that they played in helping physicists understand the physics of cosmic rays. These are **the latitude effect, the altitude effect** and **the transition effect.**

(a) **The Altitude Effect**: Discovered as early as 1912, by the Austrian physicist V. F. Hess,[2] this effect is proof of the fact that cosmic rays are extra terrestrial in origin. The finishing touches to this effect were provided by G. Pfotzer in 1936 and the curve of the cosmic ray intensity versus the altitude is called the Pfotzer curve. The curve is actually a plot of the counting rate of a Gieger counter telescope as a function of the pressure of the atmosphere above the apparatus and hence the altitude. It is shown in figure 1.1(a). The intensity rises rapidly with increasing altitude and upon reaching a maximum, falls rapidly with further increase in altitude. The explanation of this effect was provided with the discovery of the transition effect described below.

(b) **The Transition Effect:** This effect was discovered in 1933 by the Italian physicist B. Rossi[3] . The coincidence counting rate of a set of three Geiger counters placed in such a way that several particles are required to discharge them, was measured as a function of the thickness of lead placed above them. It was found that the rate increased with the thickness until it reached a maximum after which the rate decreased with further increase in thickness. The curve is shown in figure 1.1(b). The striking similarity between this curve and the Pfotzer curve led to the interpretation of the altitude effect in terms of the transition effect. Like the sheets of lead, the atmosphere does not act as an absorber but as the originator of new particles until the thickness of atmosphere reaches a critical value beyond which the shower creation process is overshadowed by absorption processes. This in turn, gave rise to the concept of primary and secondary cosmic rays.

(c) **The Latitude Effect**: Discovered by J. Clay[4] in 1927, this effect is important because it shed light on the nature of cosmic ray primary. As the name implies, the effect studied the intensity of cosmic rays as a function of the geographic latitude. The curve appears as shown in figure 1.1(c). As can be seen the cosmic ray intensity is the lowest at the equator (zero latitude), where the horizontal component of the earth's geo-magnetic field is the strongest– increasing gradually towards the poles where the field is the weakest. The fact that the intensity of cosmic rays decreases at the equator implies that most of the primaries must be charged. On the other hand, the intensity does not fall to zero implying that (i) many of the charged primaries must be highly energetic so that they reach the equator despite the field; (ii) in addition to charged primaries, there may be uncharged ones that are unaffected by magnetic fields.

Another interesting effect was **the East-West asymmetry**. It was observed that the intensity of cosmic rays from the west was higher than the intensity from the east at the equator. Assuming that the earth has a perfect dipole field, then all charged primaries can reach the earth along the axis of the dipole. Near the plane of the dipole, only particles with momentum greater than a certain amount can do so. Also, a positively charged particle is deflected by this field differently than a negatively charged particle. With equal numbers of positive and negative particles, there would be no effect observable. The fact that there is a higher intensity of particles from the west is an indication that cosmic rays are primarily positively

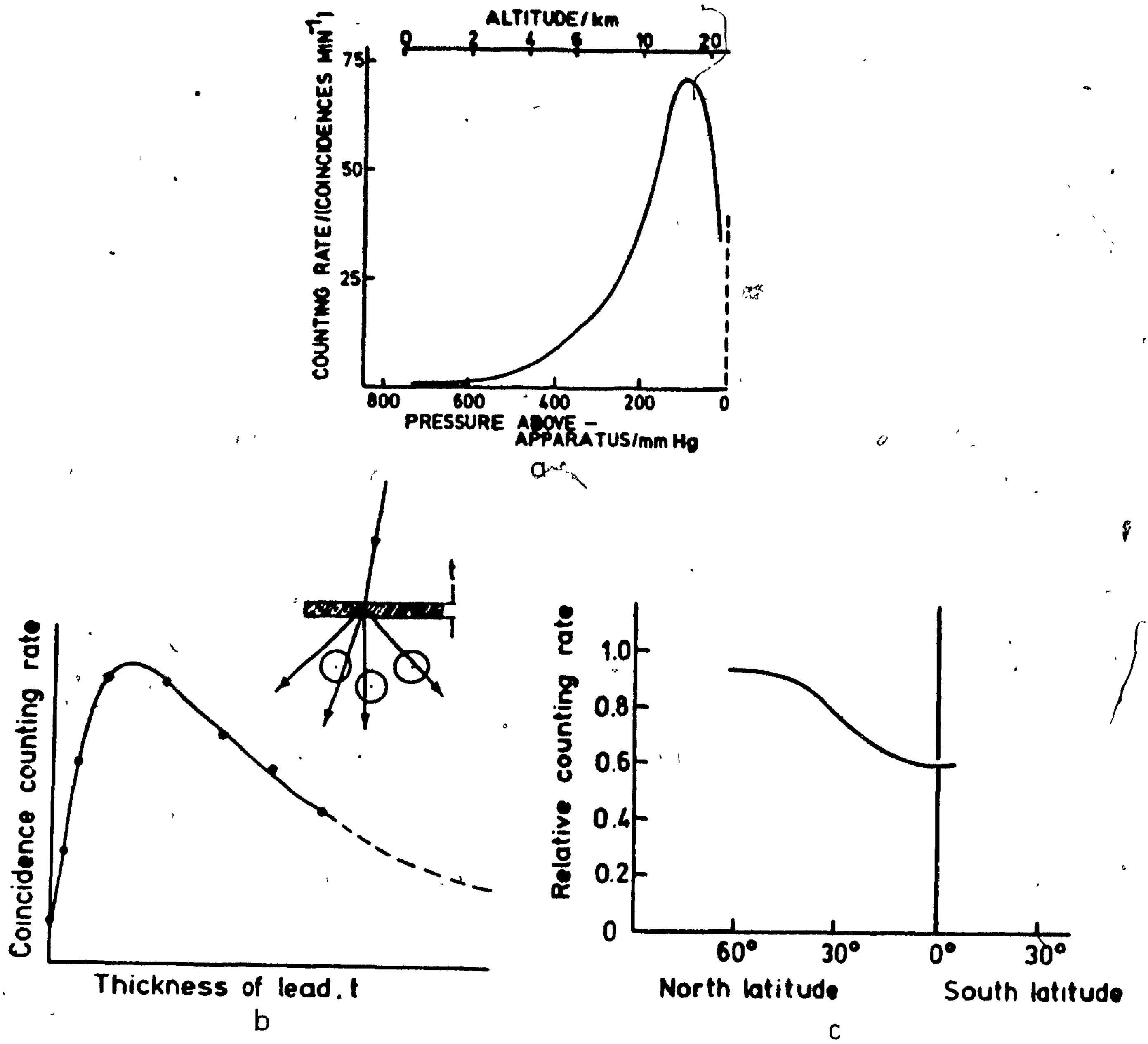

FIG 1.1: (a) Variation of the intensity of cosmic rays with altitude. The altitude in kilometres is indicated at the top of the diagram. (b) The coincidence counting rate of a group of counters placed as shown in the inset is plotted as a function of the thickness t of a sheet of lead placed above them. (c)The variation of cosmic ray intensity with latitude as recorded by airborne counter-telescope measurements. 0° latitude corresponds to the equator

charged nuclei.

The importance of gamma ray primaries was realised quite early in the history of cosmic ray studies. There are countless sources radiating high energy rays over wide ranges of energy in our galaxy as well as in other active galaxies. Most of the radiation consists of charged nuclei which, as they travel in galactic and extra-galactic space experience magnetic fields and as a consequence get considerably deflected from their original direction. As a result, charged primaries can give no useful information about the location of their source. On the other hand, gamma rays being uncharged are unaffected by magnetic fields and suffer very little deviation from their original direction, conveying valuable information about their source. The scientific potential of gamma rays was realised by theoreticians long before the experiments became possible–the experimental development of gamma ray astronomy has been rather slow by the standards of modern day physics. But experimental gamma ray astronomy has led to many interesting results including the discovery of new unsuspected sources of cosmic radiation. Ours is one such experiment, still in its infancy, which hopes to focus on, at a later stage one of the most intriguing sources of cosmic rays: the star CYGNUS-X3. More details about this will be covered in various parts of this thesis.

Section 1(b): The Composition of Cosmic Rays

The study of the composition of cosmic ray primaries has led to some very interesting clues about the matter that exists outside the solar system. Figure 1.2(a) shows the cosmic ray abundances and is drawn in analogy with the relative abundances of elements found in the solar system since cosmic rays have their abundances so similar to the solar system. The same figure can be used for the cosmic ray spectrum with a few modifications shows the actual charge composition of primary cosmic radiation. In general, the charge spectrum shows remarkable resemblance to the charge spectra of the solar system[5] . Figure 1.2(b) summarizes the differences that exist between the solar cosmic ray abundances and the galactic cosmic ray abundances[6].

In figure 1.2, the even Z (Z stands for the atomic number of the element and is equal to the number of protons in the nucleus of that element) elements are connected by solid lines and the odd Z elements by dashed lines. There is clearly an overall abundance of even Z elements over their odd Z neighbours; proof of the fact that pairing effects in the nucleus makes even Z nuclei more stable. In the $10^8 eV - 10^{11} eV$ range, the spectra consists mainly of hydrogen nuclei or protons ($\approx 87\%$) followed by about 12% helium and the remaining 1% consists of heavier nuclei from carbon to the actinides. As the energy increases from 10^9 to 10^{11}eV the ratio of the number of light nuclei (Li, Be, B) to the heavier ones (C, N, O) decreases by a factor of 2.5[7]. In the figure, the solid circles stand for elements for which the arriving cosmic rays are likely to be composed of source nuclei. Open circles stand for the opposite– elements that are fragments of the original element. The abundance of lightly bound and unstable elements like lithium, beryllium and boron is very striking. These elements have only transient existence in the sun where conditions are relatively mild and the fact that they are present in non-negligible quantities in primary cosmic rays implies that they were formed as fragments knocked off larger nuclei during their passage through interstellar matter. The squares in the figure represent the stage when cosmic rays on earth are likely to contain a mixture of both primary and secondary nuclei. The figure shows an excess of the more stable elements carbon, oxygen, nitrogen and specially iron. The

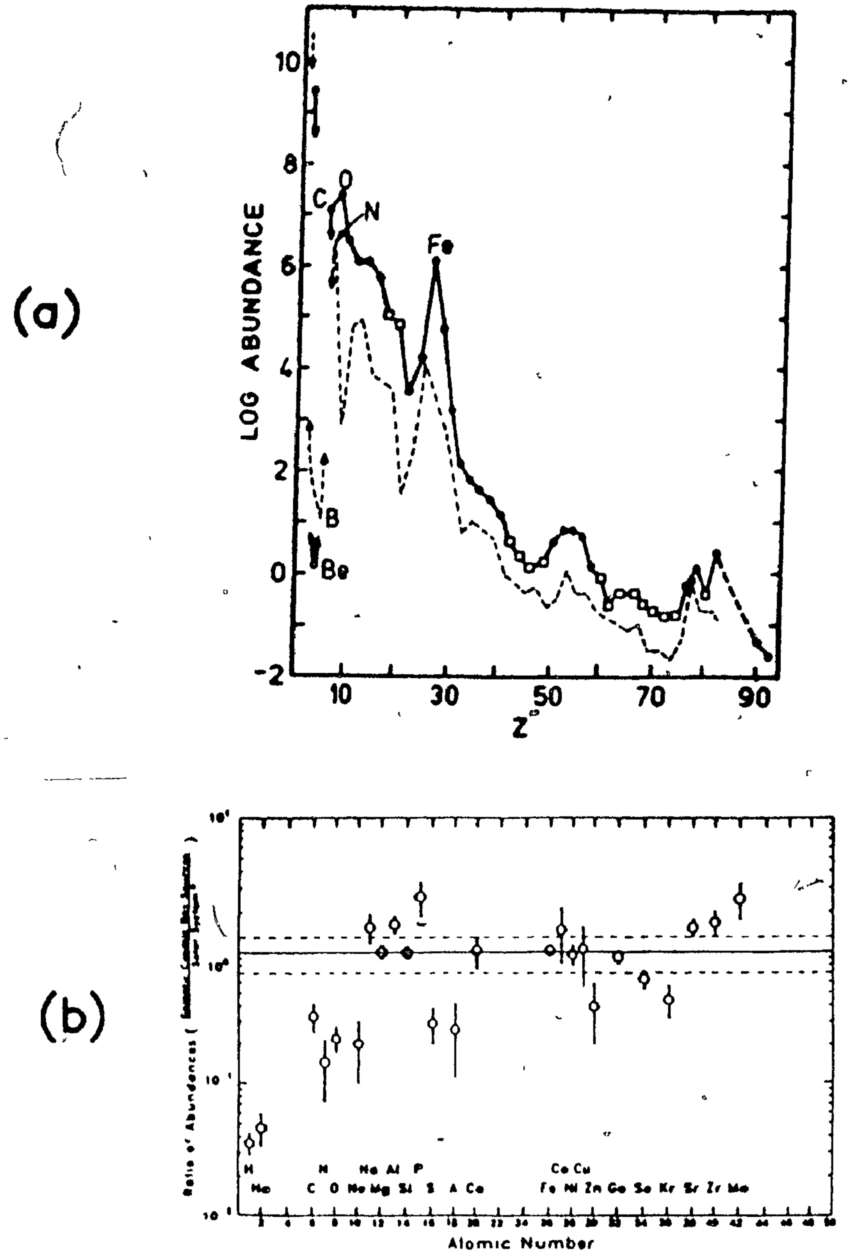

FIG 1.2: (a) Abundance of various nuclei is plotted logarithmically as a function of their Z values. The even and odd Z elements are connected by solid and dashed lines respectively. Solid circles stand for elements that are composed of source nuclei. Open circles stand for fragmented nuclei. Squares stand for primaries that are a mixture of primary and secondary nuclei. (b):The galactic cosmic ray abundances relative to solar abundances.

high iron content is confirmation of the fact that iron has possibly the most stable nuclear configuration.

A striking feature (not shown in figure 1.2) of the nuclear abundance spectra is the abundance of isotopes: a feature that is different from the solar system abundances. In particular, the identification of ^{10}Be which is formed from the fragmentation of heavier nuclei has proven very intriguing. ^{10}Be has a half life of 1.5 million years. If the production rate of the isotope is known, a measure of the abundance would be an indication of the time elapsed between its production and detection and also of the average amount of interstellar matter that the nuclei penetrated. On the basis of this principle, a figure of 10 – 20 million years has been derived for the minimum escape lifetime of cosmic rays from the galaxy and a figure of .1-.3 atom-cm^{-3} has been derived for the interstellar density[6]. There have been found, in the region beyond iron, areas with Z corresponding to the heaviest nuclei found on earth and even a few with Z in the transuranic range. In the range $30 < Z < 60$ there is a substantial abundance of strontium, tin and barium. At $Z > 60$, there is an abundance in the vicinity of platinum(Z=78) and a curious lack of abundance of actinide‡ elements: the ratio of number of 'Pt-Pb' events to the number of actinide events being 100:1. Also, so far there has been no evidence for the the existence of negatively charged nuclei. Cosmic ray electrons constitute .1% to 1% of the incoming particles in the energy range 10-1000 GeV. Thus, though the relative abundances of various elements in the cosmic rays is similar to the abundances found in the solar system, there are important differences

---

‡ **Actinide elements: $_{29}$Th, $_{92}$U, and higher Z elements are classified as actinide elements.**

that are clues to identify the astrophysical sites of cosmic ray sources and the processes that caused the high energy cosmic rays.

Section 1(c): Development of Air Showers

Though our primary interest in cosmic ray showers are restricted to those precipitated by gamma ray primaries it is important to understand the development of proton initiated showers as well to be able to distinguish between the two. The first question to answer is how do these showers originate? The answers are almost as numerous as there are number of sources and specific processes associated with specific sources. The source of particular interest to us is the star CYGNUS-X3. Figure 1.3 shows one theory of the mechanism of the production of high energy gamma rays and protons by this source. CYGNUS-X3 is a binary star system consisting of a dense neutron star and a companion star, situated 37,000 light years from the solar system at the edge of the galaxy The neutron star accelerates the protons to cosmic ray energies ejecting them in all directions. Some of the highly energetic protons strike gas nuclei of the companion star and part of its energy is converted to unstable pions. The charged pions decay into muons and neutrinos and the neutral pion decays into two highly energetic gamma rays that travel along the proton trajectory. A high energy gamma ray can travel from the outer part of the galaxy with very little chance of interacting and reaches the earth's atmosphere virtually unattenuated.

As mentioned before, air showers are created whenever a highly energetic cosmic ray collides with the field of a gas nucleus in the upper atmosphere. Electrons being the most stable and the lightest among charged primaries, have the longest mean free path in the atmosphere, travelling $\frac{1}{13}$th of the vertical atmosphere ($\sim$ 40 km) before

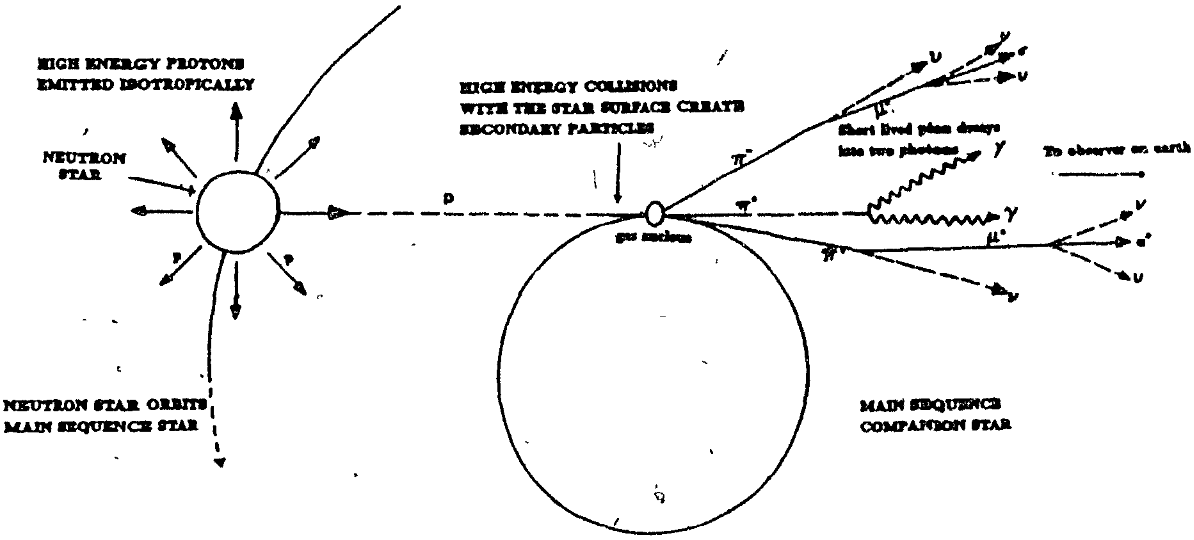

ORIGIN OF COSMIC GAMMA RAYS

FIG 1.3: One possible mechanism of production high energy cosmic rays by the star CYGNUS-X3.

colliding. Gamma ray primaries travel $\frac{1}{40}$th of the vertical atmosphere before they undergo collisions. The collision mechanism follows the same pattern as that shown in figure 1.4, producing mostly pions(π^0, π^-, π^+) along with other heavy particles like the K-mesons, hyperons, nucleons and anti-nucleons depending upon the energy of the primary and the impact parameter of the collisions. After collision, which is not strongly inelastic, the primary proton retains about $\frac{2}{3}rds$ of its total energy and continues its propagation. The secondaries, depending upon their lifetimes, either decay or undergo further nuclear interactions and create a cascade of nuclear particles called the N-cascade. The core contains the most energetic part of the cascade and the direction of the cascade is that of the primary particle.

The π^0 (lifetime $\sim 10^{-16}$secs) decays into two photons which give rise to what is known as the electromagnetic cascade(EM cascade). Each gamma ray of energy E_γ say, converts to an electron-positron($e^- - e^+$) pair each with average energy $\frac{E_\gamma}{2}$. The electron* , after travelling a short distance, is itself deflected by the electric field of a gas nucleus in the air and radiates some of its energy in the form of a gamma ray photon by bremsstrahlung. The secondary gamma rays then produce more $e^+ - e^-$ pairs and the process continues, creating an EM cascade. The process stops when the energies of individual quanta are so low that the absorptive processes take over the bremsstrahlung and pair production processes.

Showers created by gamma rays result in the formation of an EM cascade described

---

* From here onwards, unless explicitly stated otherwise, 'electron' will stand for both electron and positron.

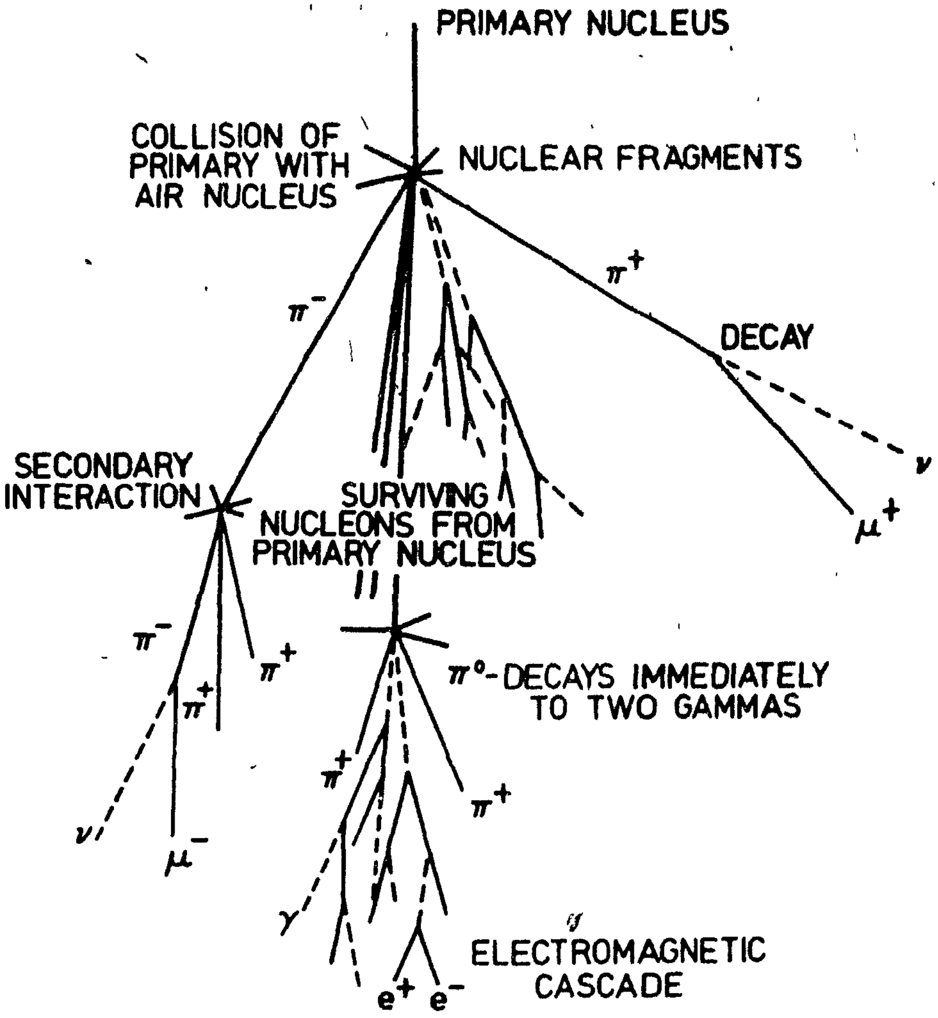

FIG 1.4: Schematic representation of the development of an extensive air shower.

in the previous paragraph. Figure 1.4 also depicts the process of formation of an EM cascade. In the case of proton initiated showers, $\sim 20-30\%$ of particles created in the first and all subsequent interactions are π^0-mesons. As a result the number of photons and electrons is greater by a factor of ~ 20 than all other particles. The $\pi^{\pm}$ and the $K^{\pm}$ that decay in flight before interaction produce muons and neutrinos. The muons have a very small interaction cross length and a relatively large lifetime ($\sim 2\times10^{-6}sec$) and they carry almost the entire energy of the parent meson. Hence they cross the rest of the atmosphere without interacting. At sea level they constitute about 10% of the particles in the air shower. Muons also have the largest spread amongst all shower particles–they can be detected at a distance of 1km from the core of the shower.

The basic features that distinguish a gamma ray shower from a proton or a charged particle shower are : The muon content: The nuclear cascade is rich in muons. It contains twenty times more muons than the EM cascade*[8]. The lateral spread of the particles: Gamma ray initiated air showers have a flatter lateral spread than the charged nuclei initiated showers[9]

Section 1(d): Energy Measurement at Low Energies

The LEDA array consists of particle detectors at ground level and like other particle detector arrays, it is capable of detecting showers initiated by primaries of energy higher than $10^{14}eV$. To detect showers initiated by low energy primaries other detection techniques are used. Showers precipitated by primaries in the range of $10^{11}eV$ to $10^{14}eV$

---

* **Gamma rays of energy $> 10^9$eV can generate π mesons by photoproduction and these pions decay into muons.**

$10^{14}eV$ are detected using arrays made up of optical detectors that detect Čerenkov radiation. Such showers are not energetic enough to reach the earth surface and are absorbed by the atmosphere. Several experiments detecting Čerenkov radiations emitted by air shower particles are currently in operation *[9,10] . The basic technique is as follows: when a charged particle passes through a medium in which its velocity is greater than the velocity of light in the medium, it emits a bluish light called Čerenkov light. Shower particles travel at relativistic velocities in air and emit Čerenkov light in a cone about the shower axis before they are absorbed by the atmosphere. The light emitted is in the visible range and is detected using focussing mirrors that focus it on to photo multiplier tubes.

This is the basic principle of the technique and different experiments achieve different levels of sophistication. The detector at the Fred Lawrence Whipple Laboratory is called the 10-metre reflector and consists of 248 mirrors that focus light onto a hexagonal array of 37 phototubes. The Fly's eye consists of 67 mirror units and 880 phototubes. There are obvious advantages and disadvantages to this method. Such experiments can be carried on only on clear moonless nights and this reduces observation time drastically. Air shower arrays are capable of operating round-the-clock and are totally independent of weather conditions. Čerenkov detectors are also very sensitive to any stray light and extreme care has to be taken when experiment is being performed. Air shower arrays are more stable in that respect. A Čerenkov detector is capable of looking at only a very small part of the sky at one time tracking a given

---

* **eg, The Fly's Eye detector at University of Utah; The Čerenkov light telescope at Fred Lawrence Whipple Laboratory at the Harvard-Smithsonian Centre for Astrophysics.**

object much like an optical telescope. A particle detector has usually an observation area extending to 30° from the vertical.

The Čerenkov technique has some great advantages. Besides being capable of measuring energy in a range inaccessible to particle detectors, Čerenkov detectors are also more accurate. They produce maps of the intensity of light that they detect and since this light is in the visible range there is very little attenuation by the atmosphere. Consequently the energy of the shower can be estimated accurately. Also the arrival direction of the primary in the case of gamma ray initiated showers can be pin pointed accurately. In general, Čerenkov detectors achieve an angular resolution that is a factor of four better than particle detectors[11].

The threshold for earth based detectors is $10^{11} eV$ and below this limit Čerenkov light is too feeble to be detected. Cosmic ray primaries below this energy are measured with balloon borne detectors or with satellite borne detectors. Detectors used in this range of energy are more often particle detectors than optical detectors because the high energy of the photons (in the case of gamma ray astronomy) allows them to be easily detected with scintillators and solid state detectors. Several types of gamma ray telescopes have been developed and flown on balloons. The balloons are usually made out of thin (typically $\frac{1}{400} cm$) polyethylene and have dimensions typically around 3 to 9 million cubic metres in volume when fully inflated. Satellite borne detectors are quite recent- the first experiment to be flown was aboard EXPLORER II around 1965 and consisted of scintillator and Čerenkov counters. Since then there has been a regular stream of experiments aboard satellites. Typically, the modern day gamma ray telescope consists of plastic scintillators sandwiched between layers of spark chambers.

The spark chamber modules are interleaved with thin (.01cm) plates of metal, usually tungsten. In the upper half these plates provide material for gamma rays to interact and produce e^+e^- pairs. In the bottom half they serve to provide pictorial information used to identify gamma rays. This combination of spark chambers and plates provides information about the energy of the gamma rays. A guard scintillator counter that encloses the entire arrangement provides the important charged particle veto. Trigger is provided when there is a coincidence between the scintillator tiles and Čerenkov counters placed below the spark chamber arrangement and there is no pulse recorded by the guard scintillator. Figure 1.5 shows a schematic diagram of the gamma ray telescope flown on SAS-II in 1972.

Section 1(e): Number And Energy Spectra of Cosmic Rays

A high energy particle entering the earth's atmosphere can create a cascade of particles that spreads over a radius of 1000 m or more from the extrapolated trajectory of the primary particle. This is the point where earth based particle detectors enter the picture. The LEDA array is an excellent example of a typical array. It consists of 19 detectors arranged to form a hexagon covering an area of around 20,000m^2 Pulses are recorded whenever a multiple coincidence occurs. Amplitudes of the pulses indicate the density of charged particles that cross the detector and the relative times of the pulses give directional information. This information is sufficient to locate the core of the shower, to determine the shower size (i.e the number of charged particles in the shower) and to determine the direction of the primary. The shower core and size are determined by using known lateral distribution functions and the energy spectrum of the primary is obtained. The most widely used form of the lateral distribution function

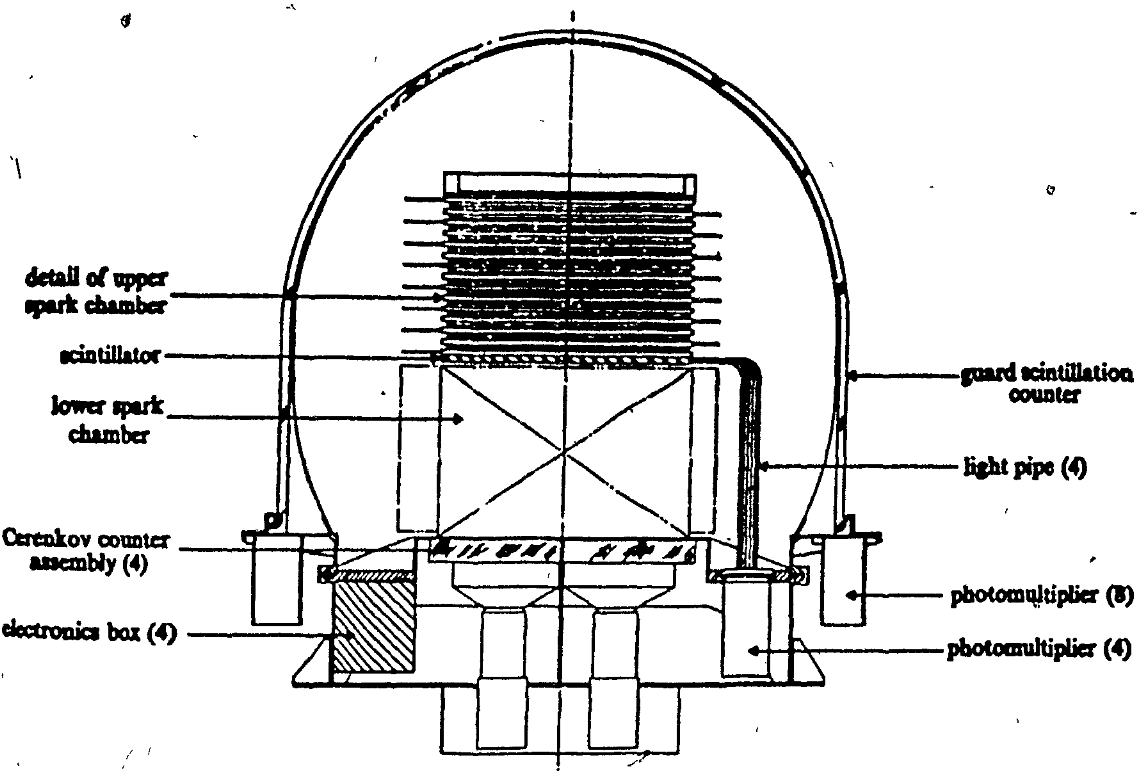

FIG 1.5: Layout of the SAS-II γ ray telescope

is called the NKG function. The exact function was given by Nishimura and Kamata and this was later modified by Griesen hence the name NKG function[12,13 ,14, 15]. The NKG function has the form:

$$f(\frac{r}{r_m}) = C(s)\,(\frac{r}{r_m})^{s-2}\,(\frac{r}{r_m}+1)^{s-4.5} \qquad (1)$$

where C_s is the normalization factor approximately represented by

$$C(s) \simeq .443\,s^2\,(1.90 - s) \qquad (s < 1.6)$$

and

$$C(s) \simeq .366\,s^2\,(2.07 - s)^{\frac{5}{4}} \qquad (1.6 < s < 1.8)$$

where r_m is the Moliere radius and s is a shower parameter called the age of the shower.

The shower age is a very important parameter and it represents the shower as it develops. $s = 0$ at the starting point of the shower ; $s = 1$ at the maximum development of the shower and $s > 1$ at the declining stages of the shower. The NKG function as given above reproduces the real data well in the range $.6 < s < 1.0$ whereas at larger s it is too small when $r < r_m$ but good when $r > r_m$. The relation between the number of particles in the shower at sea level and the energy of the shower primary E_o is given by:

$$\frac{d\,log\,N}{d\,log\,E_o} \sim s$$

In practice, the energy of a cosmic ray shower for cosmic ray showers is taken to be 10^{10} times the number of particles in the shower for the range $10^5 < N < 10^6$.[16]

In the interval 1<r<200m from the shower axis,an approximate lateral distribution function is often used with little loss of accuracy[17,18]. In figure 1.6 both functions are

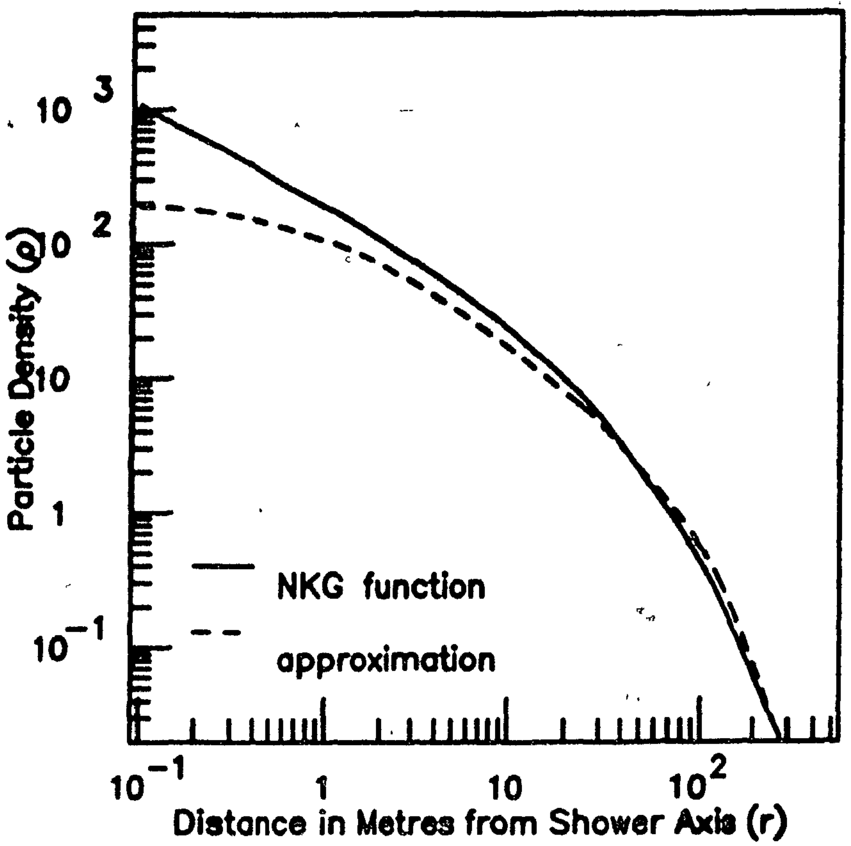

FIG 1.6: Plots of the exact lateral distribution function and its approximate form.

plotted for a shower of age 1.25 the solid line represents the exact function, the dashed line represents the approximation which is given below:

$$\rho(r,N) = \frac{N}{2\pi}\frac{exp(\frac{-r}{r_1})}{(r+1)r_1} \tag{2}$$

where r_1 is called the characteristic shower radius. Values of 10^5 for N and 75m for r_1 have been used to obtain the curve in figure 1.6. The (r+1) term takes care of the singularity at r=0. The shape of the curve is not known to 100% accuracy and it is known to vary with conditions of observation. However, systematic variation in the shape of the curve with shower size and elevation is known to be low. The function (2) fits the lateral distribution of showers of sizes from 2×10^3 to 2×10^9.

The differential energy spectrum J(E)dE can be expressed by the equation

$$J \propto E^{-\gamma},$$

where γ is a slowly varying function of the energy E. J(E) can be derived from the integral energy flux I(E),(i.e, the flux of particles having energy greater than E) which is related to I(N) the integral number spectra. I(E) is given by

$$I(E) \propto E^{1-\gamma},$$

Figure 1.7 shows the integral number spectrum for showers with $10^3 < N < 10^{10}$. The differential number spectrum is deduced from the density spectrum Transformation from N to E can in theory be achieved by determining the total energy spent by showers of various sizes in the atmosphere and underground since the energy of the primary is distributed among the secondary particles. However, such measurements are not feasible over wide ranges of the size and in practice one experiment can provide only one or two points on the energy spectrum. The LEDA array is capable of detecting energies in the range $10^{15} - 10^{16} eV$. At the low end data is limited due to low efficiency and at the high end data is limited due to poor statistics. For a pure EM cascade,

$$\frac{d\log I(E)}{d\log E} = s\,\frac{d\log I(N)}{d\log N}$$

where s is the age of the shower. The behaviour of $\frac{d\log N}{d\log E}$ resembles that of s. Figure 1.8 shows the integral and differential energy spectrum of primary cosmic rays.It is usual, owing to the steep nature of the spectrum, to plot $E^{1.5}I(E)$ or $E^{2.5}J(E)$ instead of I(E) or J(E) so that the peculiarities of the spectra are more visible. The following values for the exponent γ are considered valid[19]:

Between 10^{14} and 10^{15}eV the primary energy spectrum corresponds to an exponent γ=2.5.

At energies above 3.5×10^{15}eV till E=3×10^{16}eV, γ=3.5.

Beyond 10^{17}eV, γ=2.8 to 3.0.

The break in the spectrum is called the 'knee' of the spectrum.

The cosmic ray energy spectrum does have a cutoff and beyond this cutoff the cosmic rays are too energetic to be contained by the galactic magnetic fields. There is evidence for a cut-off of the energy spectrum at energies in the vicinity of $70 EeV^1 (1 EeV = 10^{18} eV)$ and this is in agreement with the fact that there are very few sources in the universe that could accelerate particles to such high energies. Also, the magnetic field of our galaxy in this case would be insufficient to retain a particle of greater energy within its disc. Figure 1.9 shows the size and estimated magnetic field

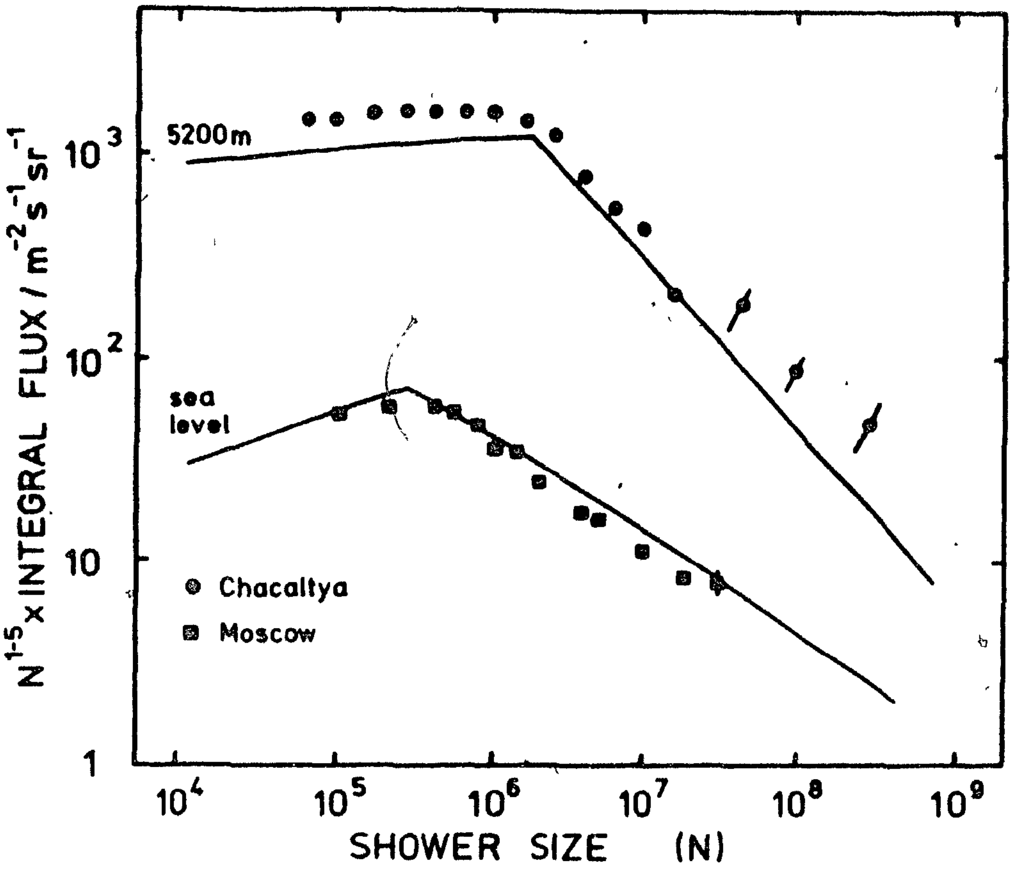

FIG 1.7: The integral shower size spectrum observed at sea level and at an altitude of 5200m. MSU stands for Moscow State University and Chac for the Chacalataya experiment. The lines show the approximate expected flux.

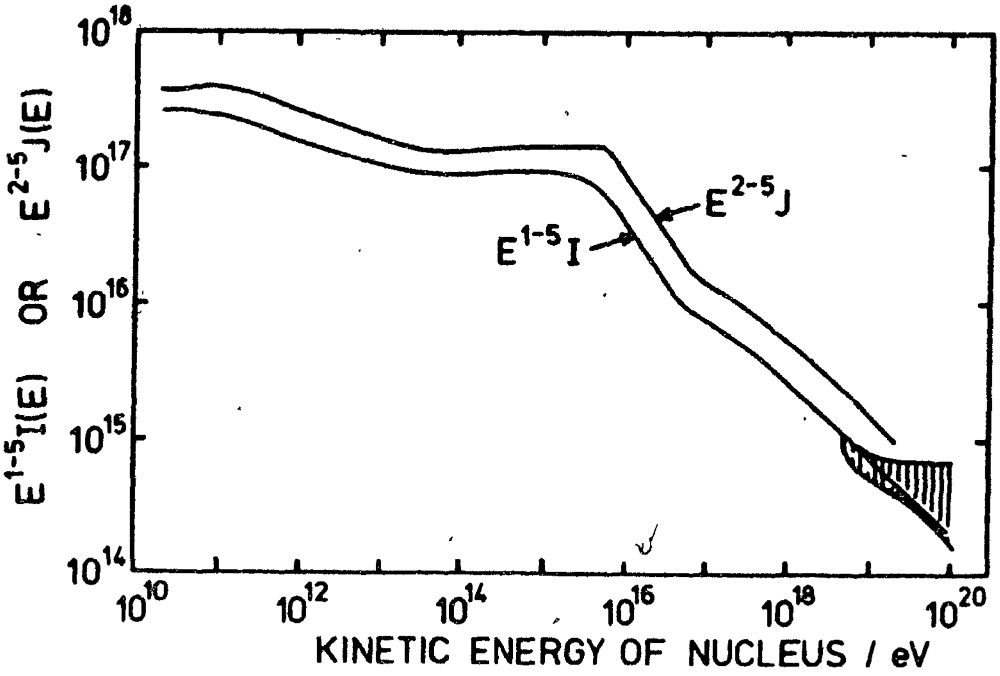

FIG 1.8: The best estimate of the integral and differential energy spectrum of cosmic rays. J is the differential and I the integral flux.

strength of several proposed sources of cosmic rays. The diagonal line is the cut off line and objects below this line cannot accelerate particles up to $10^{20}eV$. The solid line is for protons and the dashed line is for iron nuclei. Clearly there are only a few sources that just barely satisfy the requirements.

The air showers generated by primaries of the highest energy bear striking resemblance to the ones that are generated by lower energy primaries implying that the composition of the high energy primaries is not altered drastically and consist mostly of protons. Studies have shown that the highest energy primaries are mostly protons of extra galactic origin and the general direction of the protons is that of the Virgo cluster of galaxies. If the primaries under consideration were highly charged nuclei instead of protons the possibility of galactic origin (young pulsars,....) would be non-negligible.

There are different theories about the origins of particles belonging to different parts of the energy spectrum. The most widely accepted hypothesis is the following: particles of energy above $2 \times 10^{19}eV$ are extra galactic in origin and particles that are lower in energy originate in our galaxy. There are two main reasons for the first part of the previous statement:

(a) the energy flux in this part of the spectrum shows a marked difference form the rest of the spectrum,

(b) the energy dependence of the anisotropy becomes less apparent as can be seen from Figure 1.10*[20] The arrival directions of the primaries suddenly undergoes a

---

* **According to the leaky box picture (described later) of the galaxy, if particles remain in the box for a period of time T that is longer than the average escape lifetime t of the particles, then an observer situated away from the centre of the box sees an anisotropy proportional to $\frac{t}{T}$ which is also proportional to the energy of the particles.**

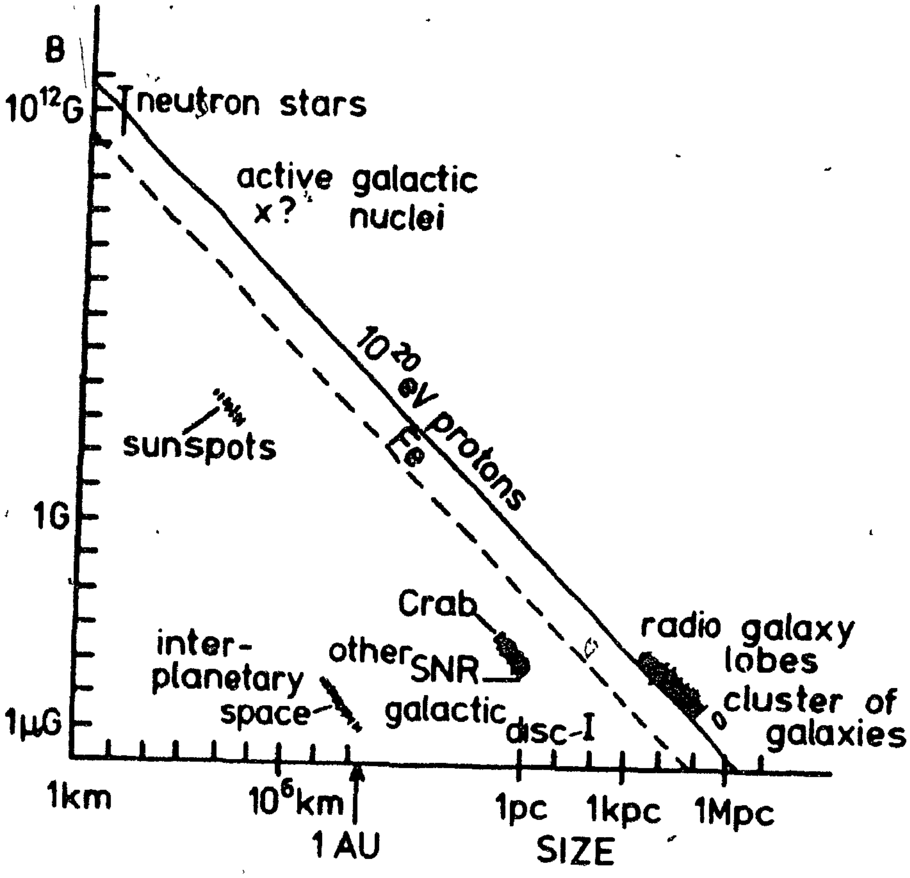

FIG 1.9: A plot the magnetic field strength of several proposed cosmic ray sources and their size. The diagonal line is the cutoff line separating sources capable of accelerating particles up to 10^{20}eV.

change and becomes biased towards northerly galactic latitudes.

The most intriguing part of the energy spectrum occurs at $\approx 3 \times 10^{15} eV$ when the slope of the flux becomes steeper and the anisotropy increases and changes phase (see figures 1.7 and 1.10). For obvious reasons this region is called the "knee" of the spectrum and the region above this is called the "ankle" of the spectrum. Figure 1.11 shows the changes in composition that occur near the knee of the spectrum. Besides the changes in anisotropy and flux, there is also a rapid change in the depth of the shower maximum implying a higher energy per nucleon. This has been interpreted as being due to a change from near iron composition to mainly protons at higher energies. However, the number of muons in the shower is also sensitive to the energy per nucleon and in this range it shows no change in depth, thus implying contradictorily that there is no change in shower composition at this stage. The shower cores also undergo change in this range becoming flatter instead of steeper as energy increases implying that the angle of emission of the hadrons increases. With so many conflicting events occurring in the same interval, it is hardly surprising that there have been so many theories of the origin of the knee.

Section 1(f): Interpretation(s) of the knee in the spectrum

The rapid fall of flux above the knee indicates that the rate of leakage from the galactic box increases. Models of cosmic ray confinement seek to explain the observed isotropy and composition of cosmic ray data. The leaky box model is one of the many models used for this purpose. It is assumed that cosmic rays are trapped inside reflecting boundaries surrounding the galaxy and that the probability of escape into extra galactic

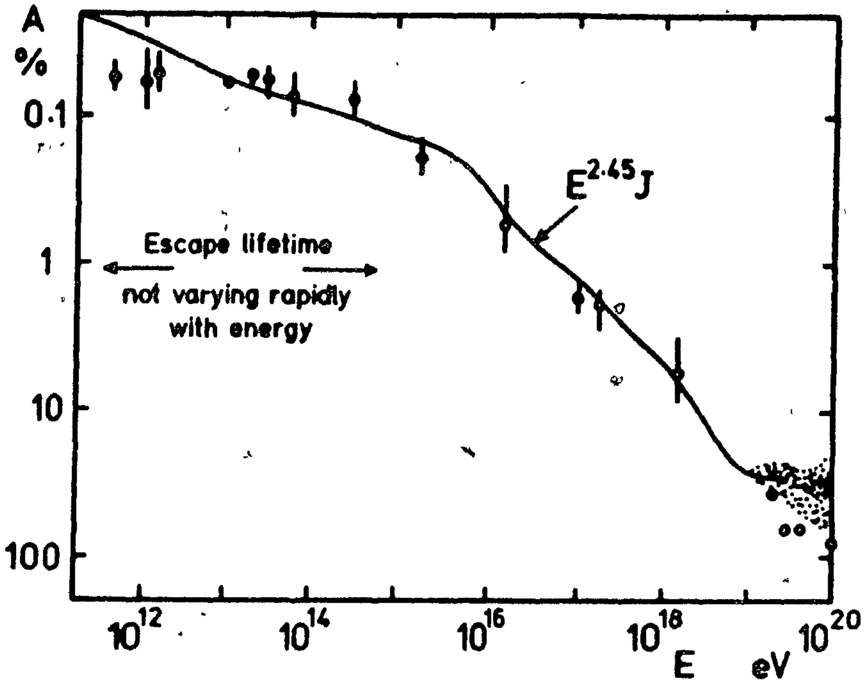

FIG 1.10: Energy dependance of anisotropy.

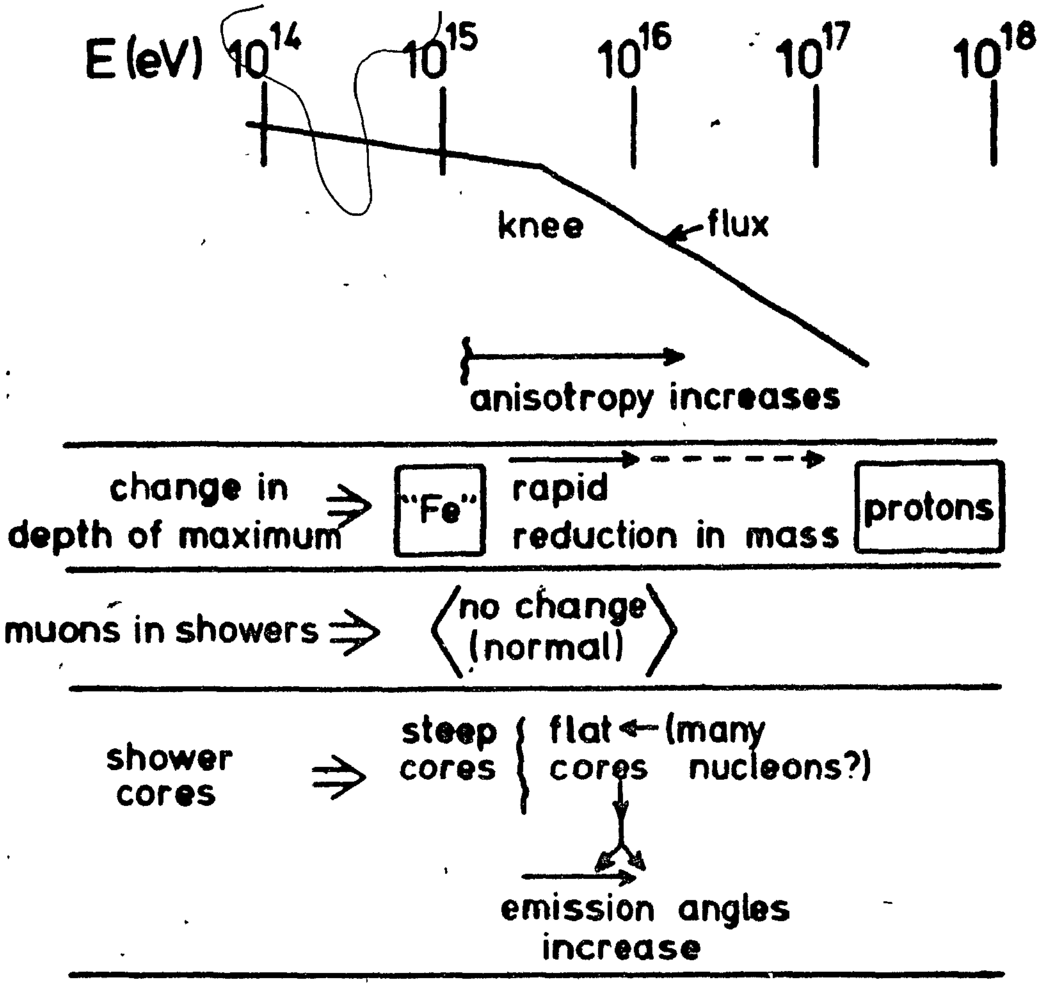

FIG 1.11: Changes in the composition of cosmic rays in the region of the knee in the spectrum. '?' indicates regions where there are conflicting conclusions.

space is finite. The model assumes a uniform density of cosmic rays throughout the volume of the box.Leakage of particles in the "leaky box" model is controlled by the magnetic field and hence the change should occur at an energy $\propto Z$. This in turn implies that the composition of cosmic rays would change starting with the leakage of protons and moving onwards to iron nuclei. The spectrum would bend a little at energy E_p say, and the steepest bend would occur at energy $26E_p$ where all nuclei from hydrogen to iron were leaking away. The fact that the energy spectrum does not show such a two step process indicates that this interpretation is not exact.

A second interpretation relates the knee region to photo nuclear reactions at the source. For instance, as particles from a pulsar escape through the magnetic field of a supernova, iron and protons would be affected at the same total energy. This theory explains the knee successfully but the anisotropy part is still uncertain. The anisotropy part is attributed to the presence of a special component that changes direction at $10^{15}eV$. The possibility of transition from heavy nuclei to protons at the knee raises questions about the nature of the extra galactic particles above 10^{16}eV. Though this would explain nicely the nature of the spectrum there is no irrevocable proof of the fact that the cosmic ray composition above 10^{16}eV is any different from ordinary galactic cosmic rays. The knee position has also been related to the diffusion of cosmic rays which scatter off of magnetized clouds in interstellar medium[21]. Above the knee the deflection of cosmic rays by the cloud could give rise to a change in γ of .9 which is close to the observed values till $\approx 10^{16}eV$. However, to achieve the right amount of anisotropy, the number of such clouds required is so high that it puts the very theory in doubt.

The knee of the energy spectrum still is a region of mystery for which there is no absolute solution. The fact that the knee does occur at the energy indicated above is undisputed. It has been observed again and again by different techniques and different groups. Until a theory is proposed that explains all the observed effects and not just one or two, it will continue to arouse the curiosity of astrophysicists all over.

2. THE COSMIC RAY DETECTOR

Section 2(a):General Considerations

Any detector designed to measure particle density must have two basic characteristics:

(1) a well resolved single particle peak;

(2) uniformity of response.

A well resolved single particle peak is very important for detector calibration: the usual technique of converting pulse heights recorded by analog to digital converters (ADC's) to number of electrons involves dividing the pulse heights by the mean of the single particle spectrum. Inability to achieve a clean single particle peak can lead to systematic errors in determining the number of particles that traversed the detector, causing serious errors in data analysis. This criterion is a function of the light collection efficiency of the photo tube; the light emitting capabilities of the scintillator and the efficiency of the arrangement that directs light emitted by the scintillator to the photo tube. In what follows, each of these factors will be discussed in some detail.

The Scintillator

An ideal scintillator would be one that has a high light output, a short decay time and high quantum efficiency, so that a single particle passing through the scintillator produces a pulse in the phototube of high amplitude that rises to its peak and decays rapidly, giving a pulse output that is distinct and unambiguous. There are two classes of scintillators – inorganic and organic. Sodium Iodide (NaI) is one example of an inorganic scintillator. Light output of these scintillators is very high compared to organic scintillators and there is very little statistical fluctuation in the number of photons; consequently, the pulse height resolution is better. However, besides being more expensive, inorganic scintillators also have very large decay rates- $\sim .2\mu s$ compared to a decay time of a few nano seconds for organic scintillators. Organic scintillators are also less expensive and can be easily cast into any desired shape. These scintillators are most commonly used in the construction of detectors. All organic scintillators have two active components – the primary fluor which has molecular levels that get excited and emit ultra violet light during de-excitation; a secondary fluor which is essentially a wavelength shifter (with the absorption spectrum the same as the emission spectrum of the primary fluor), that shifts the ultra violet light to visible region so that it can be detected by a photo tube. These two components are either dissolved in a suitable liquid yielding liquid scintillators, or are mixed with a suitable substance and polymerized using aromatic or aliphatic polymers giving Poly Vinyl Toluene (PVT) or acrylic (PMMA) scintillators, respectively. Acrylic scintillators have light outputs much lower than liquid or PVT scintillators but they are comparatively inexpensive and are fast gaining popularity as particle detectors replacing PVT detectors in many cases. Liquid and PVT scintillators are comparable in all respects except price: liquid scintillators cost much less. This experiment uses liquid scintillator BC-533* which has a light output of 51% Anthracene and a decay time of 3 nano seconds(ns) compared to 60% and 3.3ns for the popular NE110 plastic scintillator.

PVT and acrylic scintillators have one very distinct advantage — they are more convenient from the point of view of breakages. In general liquids need more care in

---

* Bicron Corporation, Newbury, Ohio, USA.

handling than do solid scintillators. Liquid scintillators are hydroscopic and have to be well protected from moisture. They can absorb the small quantities water in the air and under warm and humid conditions, water can dissolve in the scintillator. When cooled, the water condenses forming a fine fog of droplets or ice crystals in the liquid[20]. Liquid scintillators also have to be tested for stability in the presence of materials used to build the containers. For optimum performance, they have to be de-oxygenated prior to use. All things considered, the choice of scintillator for any experiment is dictated by two factors - the [illegible] of use and financial resources available to the project. An important factor to be kept in mind when constructing a particle detector of this type is the volume or the amount of scintillator to be allotted to each detector. This is an factor is important because one has to achieve an optimum level: too thin a layer would give a very low light output and with too thick a layer interactions that take place in the scintillator would have to be taken into account.

The Phototube

A photo tube with a dome shaped or a hemispherical surface has collection over a large surface area. The shape of the photo-sensitive surface of the photo tube plays an important role in the timing efficiency of the photo tube. With a hemispherical photo tube, the transit time for photo electrons from all parts of the photo cathode is the same. Also, the efficiency of the photo cathode is uniform over the entire surface.

The Light Collecting System

Ideally, all the light that is emitted by the scintillator should be directed to the phototube with as little modification as possible. Depending upon the detector configuration and the use to which they are put, this goal is achieved by different groups in different ways. The ideal solution to the problem would be to have the photo tube at the focus of parabolic dome, perfectly reflecting on the inside so that all the light incident on the dome would be reflected and arrive at the photo tube to be detected. This concept not easy to realize in real life because of the inherent difficulties associated with constructing a perfectly parabolic dome. The second alternative is easier to realize and is consequently very popular. The scintillator surface is coated with a highly reflective coating and light guides are attached to the scintillator at suitable points with a photo tube fixed at the other end of the guide to detect light. A third method involves having a light collecting cone or a pyramid with the inner surface polished so that all the light that is emitted reaches the photo tube by multiple reflection. This is the approach that we adopt in this experiment.

The second characteristic that a detector must have is uniformity of response - two identical particles with identical energies, upon passing through different parts of the detector must, in the ideal case, produce identical pulses in the photo tube. This is not true in general. This factor is the function of the detector geometry and the following statistical factors:

(i) Photo-electron statistics: The conversion of photons at the photo cathode and their subsequent multiplication at the dynodes, especially the first, is a statistical process that shows fluctuations. These fluctuations are intrinsic to photo tubes and cannot be controlled by experimental arrangements.

(ii) Landau statistics: Energy loss of charged particles in a scintillator is also governed by statistics and as a result this factor also shows fluctuations.

The detector geometry plays an important role in achieving a uniform response from any detector. In general, photons that are emitted from the centre of the scintillator or the part that faces the the photo tube directly are collected more efficiently than those emitted from the more remote parts of the detector. Again, the method chosen to achieve uniform response from a detector varies, and depends upon the ingenuity of the experimentalist. One of the common methods involves having more than one light guide-photo tube assembly looking into the detector and then summing up the pulse heights to get rid of any non uniformity.[21]. An alternative method consists of scribing thin lines on the face of the scintillator and effectively attenuating light from the high efficiency areas. The approach taken by this experiment is the opposite — instead of throwing away excess light, the amount of light generated is controlled by varying the amount of scintillator in different parts of the detector. Details are given in the next section.

Section 2(b): Design and Fabrication of the Counter

The counters used the LEDA array consist of three main parts: the scintillator dish, the light collecting cone and the photo multiplier tube. The dishes are 1m^2 in area moulded out of 6mm thick white acrylic. The acrylic was tested by us by exposing it to both to the liquid and its vapours for extended periods of time and no evidence of deterioration was detected. The choice of 1m^2 for the area has two simple reasons. Firstly, it has become a standard choice in EAS experiments. Secondly, the acrylic used to for the dish comes in sheets of 1.2m×2.4m and two dishes can be moulded from one sheet with very little waste of material. The formation of the dish takes place in two steps. First the mould for the dish is constructed out of plywood at the workshop in the Physics department. The plywood cast is taken to the Carleton University School of Industrial Designs in Ottawa and the dishes are moulded there. The School of Industrial Designs at Carleton University is the facility closest to McGill equipped with a moulding machine big enough to mould the detector. The operation of moulding takes about 25-30 minutes. The dish is then trimmed leaving a lip of about 2 cms around the rim. A clear 3mm thick acrylic window is glued on to the dish using di-chloroethane as a solvent type cement. Ideally the detector should be circular in shape, but octagon is a good approximation to a circle and an octagonal dish is much easier to implement in plywood. So this was chosen as the shape of the detector. The reason behind desiring a circularly shaped dish will be discussed shortly.

The light collection cone is an eight faced truncated pyramid made out of white PVC which appears as shown in figure 2.1. Each panel is trapezoidal in shape and the the eight panels are joined using strips of PVC bent at an angle, with holes for screws to enable attachment to the panels. In arriving at a final design three constraints had to be satisfied:

(1) The top of the pyramid which is an octagon, had to be big enough to fit the 130mm (5″)photo tube without leaving too much gap in between.

(2) The bottom of the pyramid sits on the dish containing the liquid scintillator and so the lower edge each panel of the assembled pyramid had to align with the sides of the dish (which is 580mms).

(3) For the best response the phototube should be as high above the detector as possible without making the detector physically bulky. The reason for this constraint is discussed in section (c).

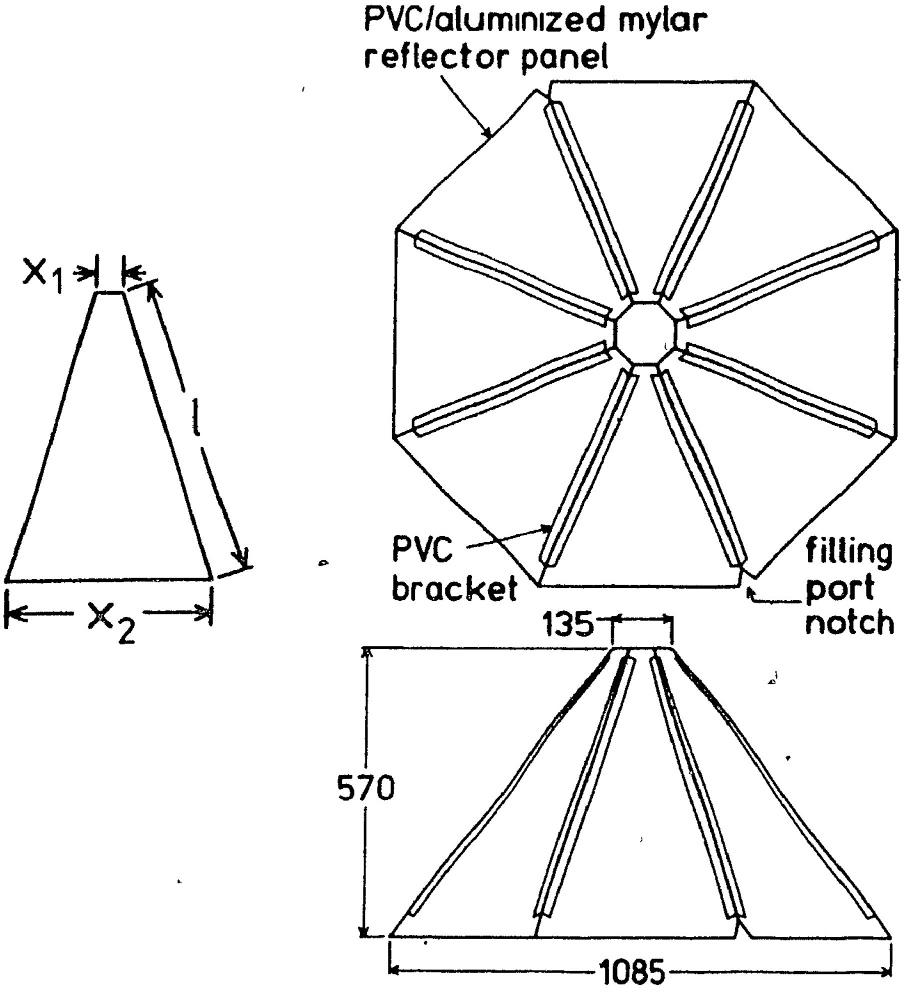

FIG 2.1: Plan and side view of the light collection cone used for detectors in the LEDA array

The first constraint yielded (ref figure 2.1) $x_1 \sim 54mm$; the second yielded $x_2 \sim 580mm$. The third constraint led to $l = 1000mm$.

Two pyramids were constructed and tested, one with no coating on the inside and the other with a mirrored inside, constructed using mirrored PVC. The pulse height spectrum in each case was obtained and fitted with a Landau curve. The results are shown in figure 2.2 and 2.3. Since the scintillator dish is semi-translucent, light losses occur due to particles passing through the bottom of the dish. To test the degree of seriousness of this factor, the response of the detector with a sheet of reflecting mylar was compared with the response obtained without the mylar sheet. The result is the plot 2.4. – showing considerable increase in the mean of the pulse height spectrum. It is clear that a mirrored cone has a much better light collection efficiency than the white cone even without the sheet of mylar. Since mirrored PVC is expensive, a layer of aluminised mylar was glued on to white PVC and the response of the detector tested. The results is shown in figure 2.5. Since there is not much change in the detector response, aluminised mylar was substituted for the mirrored PVC.

The photo tubes used in this experiment are 5$''$ R2218 Hamamatsu photo tubes with hemispherical photocathode shown in figure 2.6 The photo tube operates well between -80^o to +50 ^{o}Celsius and has a maximum voltage rating of 1800 vdc, a current amplification of 1×10^8 and 13 dynodes arranged in the venetian blind fashion. The hemispherical surface photo cathode allows light collection over almost the full 2π solid angle. On the other hand, the size of the tube is small enough to allow us to neglect the variation in electron collection efficiency of the first dynode[22].

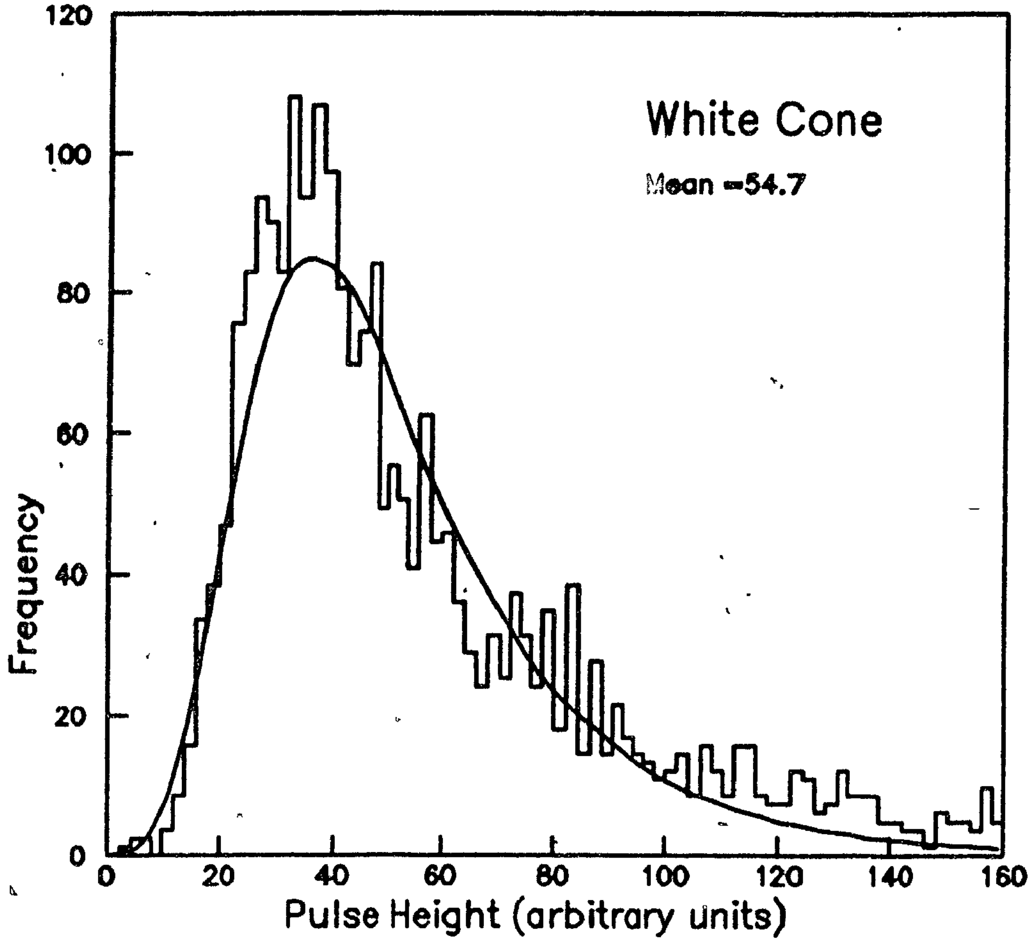

FIG 2.2: Pulse height distribution obtained with light collection cone made of white PVC with no coating inside.

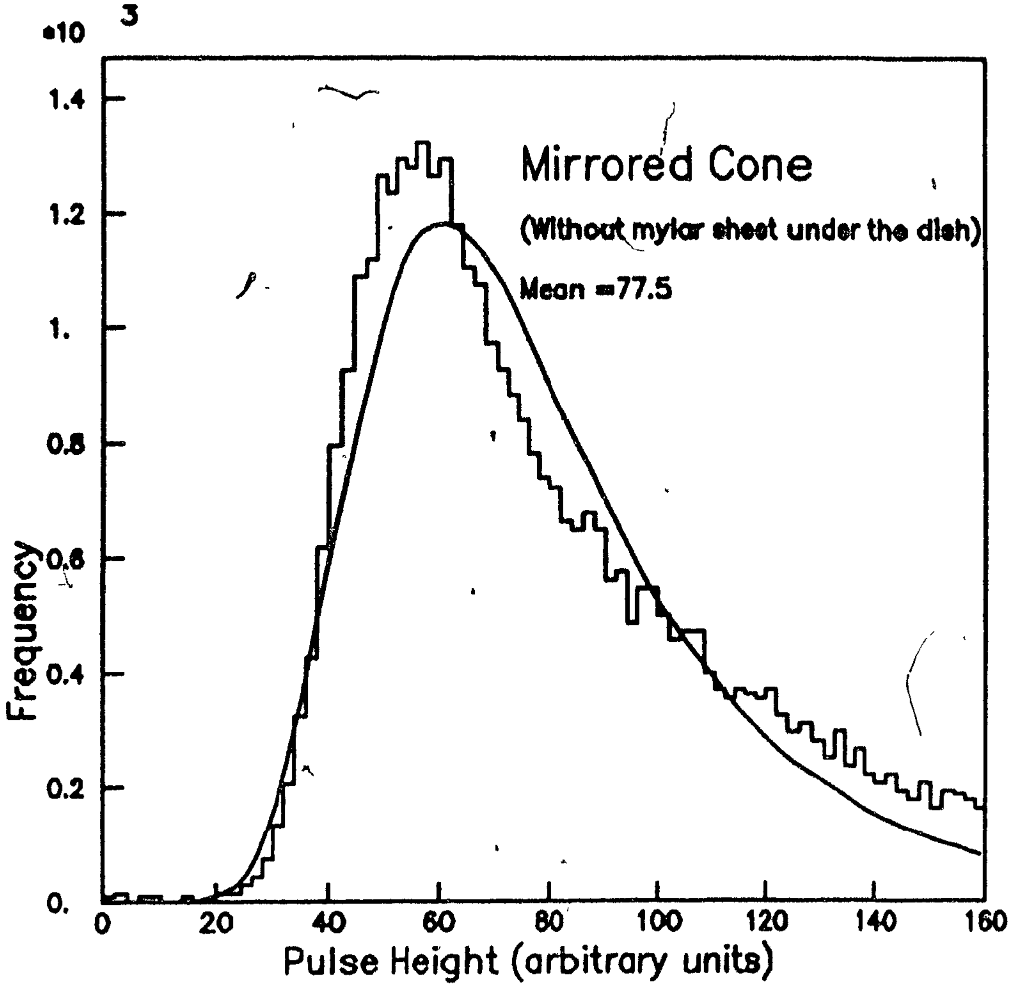

FIG 2.3: Pulse height distribution obtained with light collection cone made of mirrored PVC .

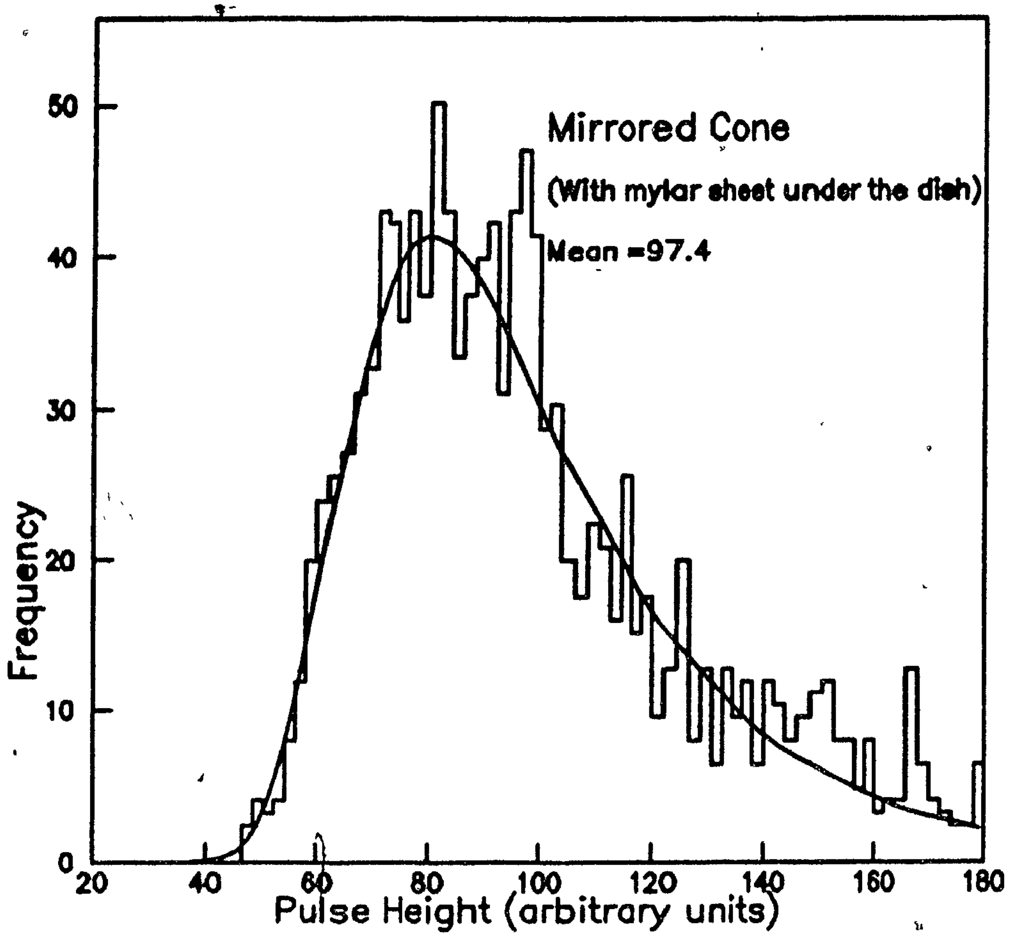

FIG 2.4: Pulse height distribution obtained with light collection cone made of mirrored PVC and a sheet of mylar under the scintillator dish.

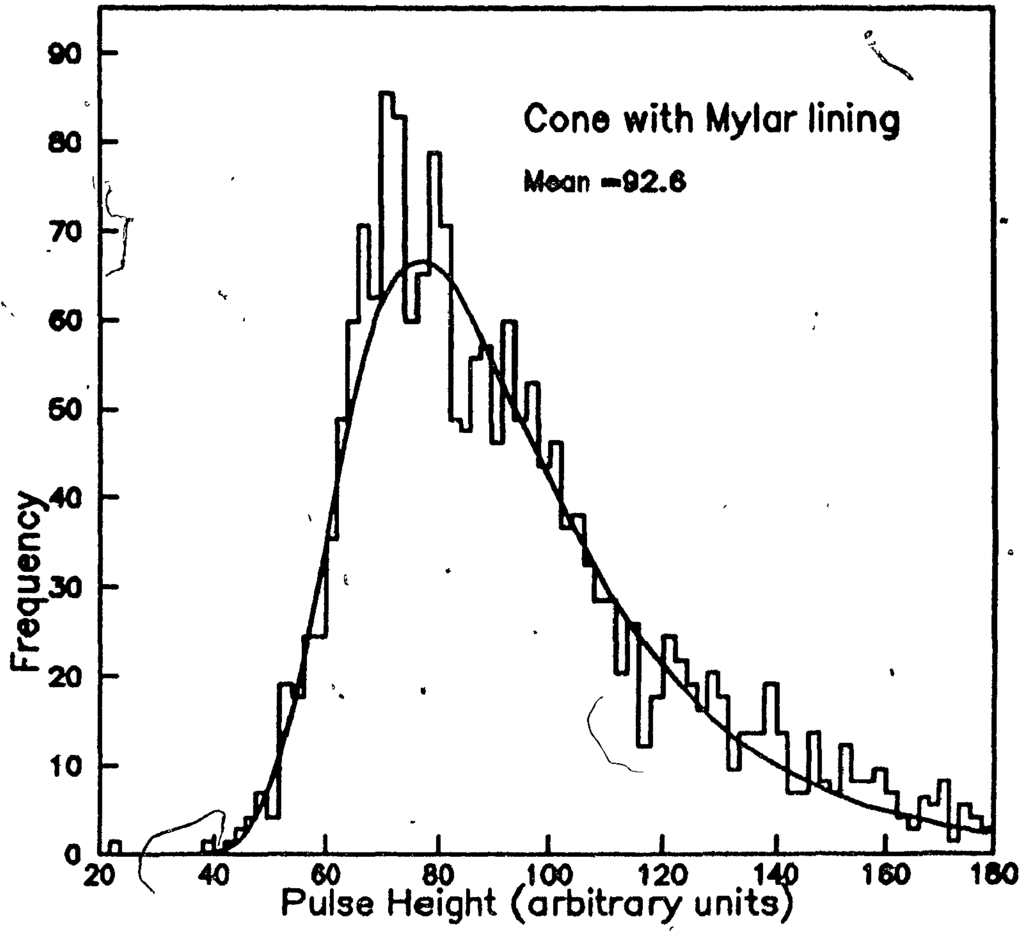

FIG 2.5: Pulse height distribution obtained with light collection cone made of PVC with a layer of mylar on the inside and a layer of mylar under the dish

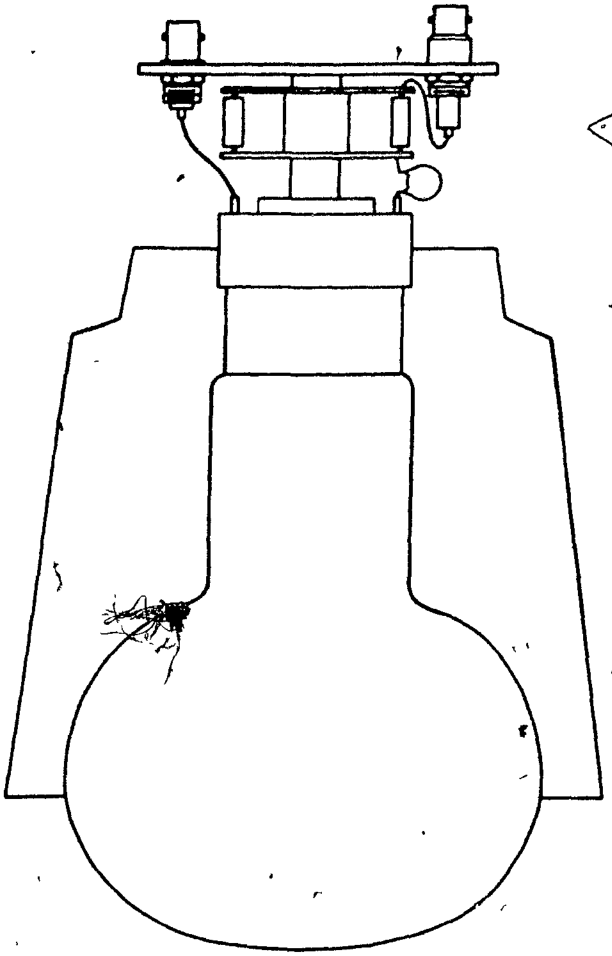

FIG 2.6: A cross sectional view of the phototube mount. The base is attached to an inverted PVC cup which rests on the light collection cone

Section 2(c): The Final Detector Design

In arriving at the final prototype for the dish and the light funnel, a great deal of very useful information was extracted from the paper by R. W. Clay and A. G. Gregory[23] entitled "Light collection from a $1m^2$ scintillator for cosmic ray work". Using a 12cm diameter scintillator as a gating or a triggering device for a multi channel analyzer, they did a very comprehensive study of the the outputs obtained under different conditions when the trigger was placed in ten different positions above the $1m^2$ scintillator. Their experimental setup and the trigger positions are shown in figure 2.7(a) and (b) Tests were done with 5 different heights of the of the light collecting pyramid and twelve different coatings for the inside of the pyramid. Their results for different detector geometries with NE-560 coating on the inside of the pyramid are shown in Table 1. The column showing the percentage variation of pulse amplitude at different gating positions from the position 1 has been added on.

An ideal detector would give the same output at gating position 1 and at gating position 10. As can be seen from the figures in column three, with the photo tube 300mm from the scintillator, there is a difference of 57% between the two outputs; at a distance of 600mm however, this difference reduces to ~40%. No doubt that the uniformity could improve with further increase in the distance between the photo multiplier and the scintillator, but at this point the physical size if the detector arrangement becomes considerably bulky. There is another remarkable feature that can be noticed from the figures. A circular detector of area 1 m^2 would pass through the positions indicated by the dotted lines. It is clear that the response of a circular detector would be more uniform compared to a square detector. The authors also did a comparative

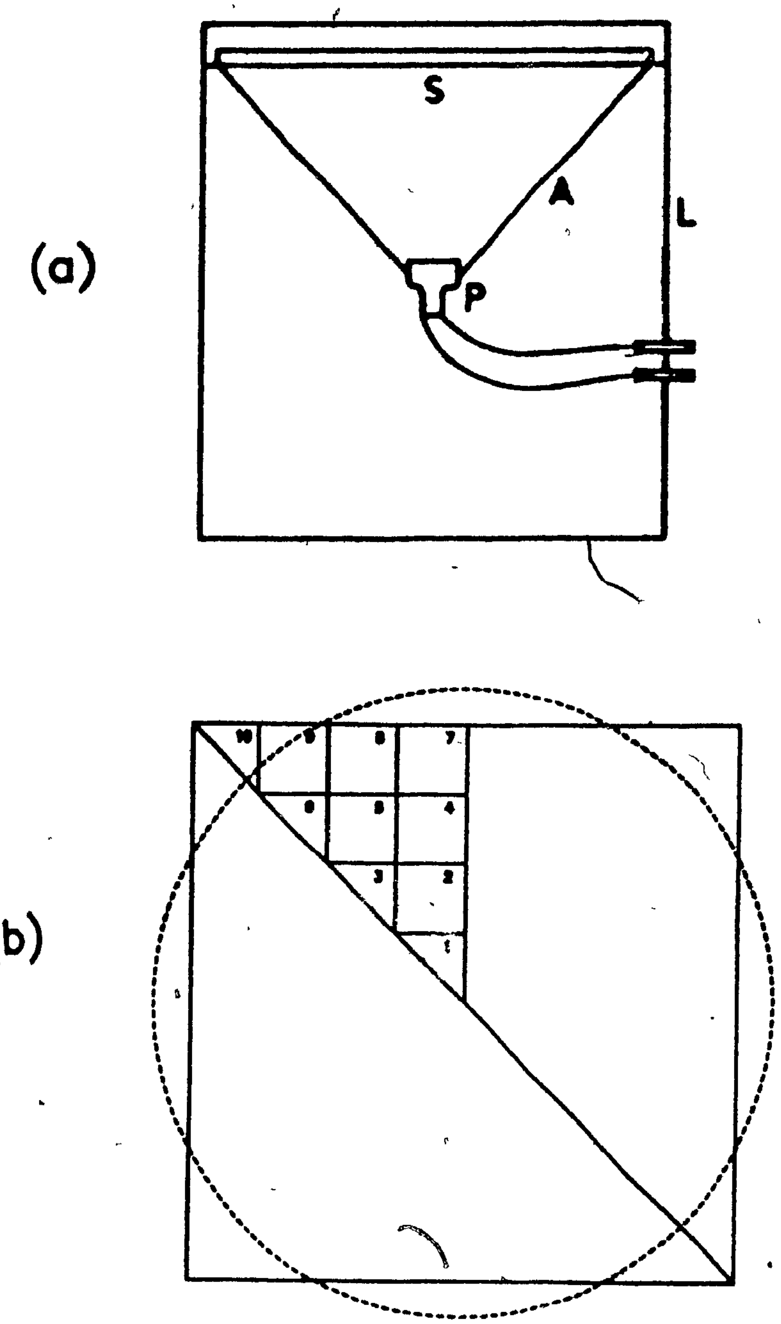

FIG 2.7: (a) Schematic diagram of the experimental set up used by Clay and Gregory. A-aluminum pyramid with coating on the inside; L-a light tight box containing the detector; P-photomultiplier; S-scintillator. (b) The different gating positions which correspond to the positions of the gating detector placed above the scintillator

study of the effect of changing the surface coating of the pyramid keeping the photo tube distance fixed. The results obtained for aluminised mylar coating and that for the expensive NE-560 are shown in Table 2. While the resulting amplitude for the NE-560 is slightly higher on the average, the uniformity of response shows only a 10% difference between the two coatings— the mylar being better.

Having decided upon an octagonal dish with a light funnel 57cms high, a dish with a flat bottom was moulded, the detector assembled and its response tested. In this case since the detector is roughly circular, more than half its area lies beyond a radius of 40cms; so uniformity of response across the radius is a very important factor. The dish was filled with ~40 litres of liquid scintillator. The arrangement was made light tight by draping a black cloth over it and enclosing the detector in a plywood hut. A trigger counter was constructed out of a 4cm wide, 100 cm long, 2cm thick strip of plastic scintillator and two 2″ photo tubes, one at each end of the strip. The trigger counter* was placed under the detector along its diameter. Output from the three photo tubes were fed to ADCs and through a discriminator to Time to Digital Converters(TDCs) as shown in figure 2.9. Outputs T_1 and T_2 from the counters go to an AND gate. Essentially this means that a start pulse for the TDC and the gate for the ADC are generated only when a pulse is recorded by the trigger counter. An additional delay is added on to T_2 so that the clock starts only after a signal from T_2 is received.

A plot of the mean detector pulse height versus the difference between the times

---

* **To avoid confusion, from this point onwards the term detector in this chapter will stand for the actual detector assembly and the term counter(s) for the trigger counter(s).**

Table 1

(a)

Pyramid coating		NE560					
PMT distance (mm)		300		400		600	
		counts	% diff	counts	% diff	counts	% diff
Gating position	1	63	0.0	44	0.0	38	0.0
	2	52	17.5	38	13.7	37	2.6
	3	45	28.6	36	18.1	35	7.8
	4	44	30.1	33	25.0	35	7.8
	5	41	34.9	32	27.3	34	10.5
	6	38	39.7	29	34.1	32	15.8
	7	37	41.1	30	31.8	30	21.0
	8	35	44.4	27	38.6	29	23.7
	9	31	50.8	23	47.7	29	24.7
	10	27	57.1	23	47.7	23	39.5

Table 2

(b)

Pyramid coating		NE560		Aluminized mylar	
PMT distance (mm)		400		400	
		counts	% diff	counts	% diff
Gating position	1	44	0.0	39	0.0
	2	38	13.7	35	10.3
	3	36	18.1	33	15.4
	4	33	25.0	32	17.9
	5	32	27.3	32	17.9
	6	29	34.1	28	28.2
	7	30	31.8	27	30.7
	8	27	38.6	27	30.7
	9	23	47.7	26	33.3
	10	23	47.7	22	43.6

FIG 2.8: Output pulse ampltude with scintillator at the gating positions indicated and (a) PMT at different distances; (b) different coatings on the pyramid surface.

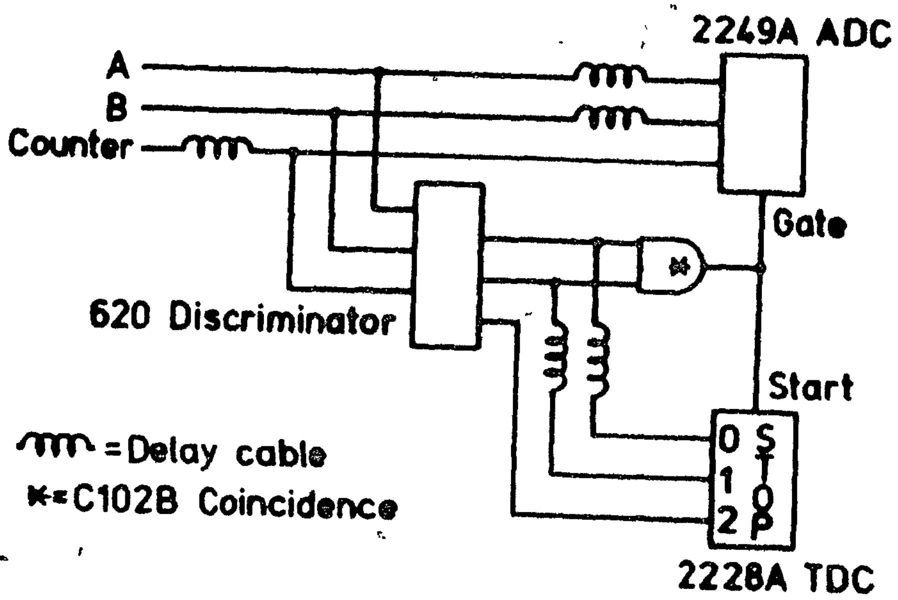

FIG 2.9: Schematic of the electronics used to study the unformity of response of the test detector. A and B refer to the two trigger counters. Counter here refers to the test detector.

at which T_1 and T_2 recorded the passage of the same pulse gives direct information about the uniformity of response of the detector. The trigger counter and the detector are separated by a distance of only ~2-3cms and so a particle that passes through the center of the detector passes through the center of the trigger counter. In this case, the difference $(T_1 - T_2)$ would be zero. Similarly, negative value would signify the passage of a charged particle through a particular section of the detector and a positive value the passage through a section on the opposite side of the center of the detector. In effect, this is the same as having a small trigger counter under the detector and recording coincidences between the detector and the trigger counter. By having a longer trigger counter spanning the entire detector end to end, we eliminate the need to move the trigger counter from one position to another. At the same time, data can be obtained from essentially all the points along the diameter of the dish. A plot of the pulse height versus the distance from the centre of the detector is shown in figure 2.10. For a detector with a flat bottom, the response of the detector shows considerable variation over the radius of the dish.

Our solution to the problem lay in modifying the design of the bottom of the dish from perfectly flat to one with different levels in it. The central part of the dish from which the photo tube efficiency is the highest, was elevated to a height of 25mm with respect to the flat version. As a result, the layer of scintillator in this part of the dish is less thick and the light output from the dish is automatically reduced. In its final design, the dish consists of five levels and appears as shown in figure 2.11. The pulse height response of the modified dish is also shown in figure 2.10; the average radial variation in the response is greatly reduced.

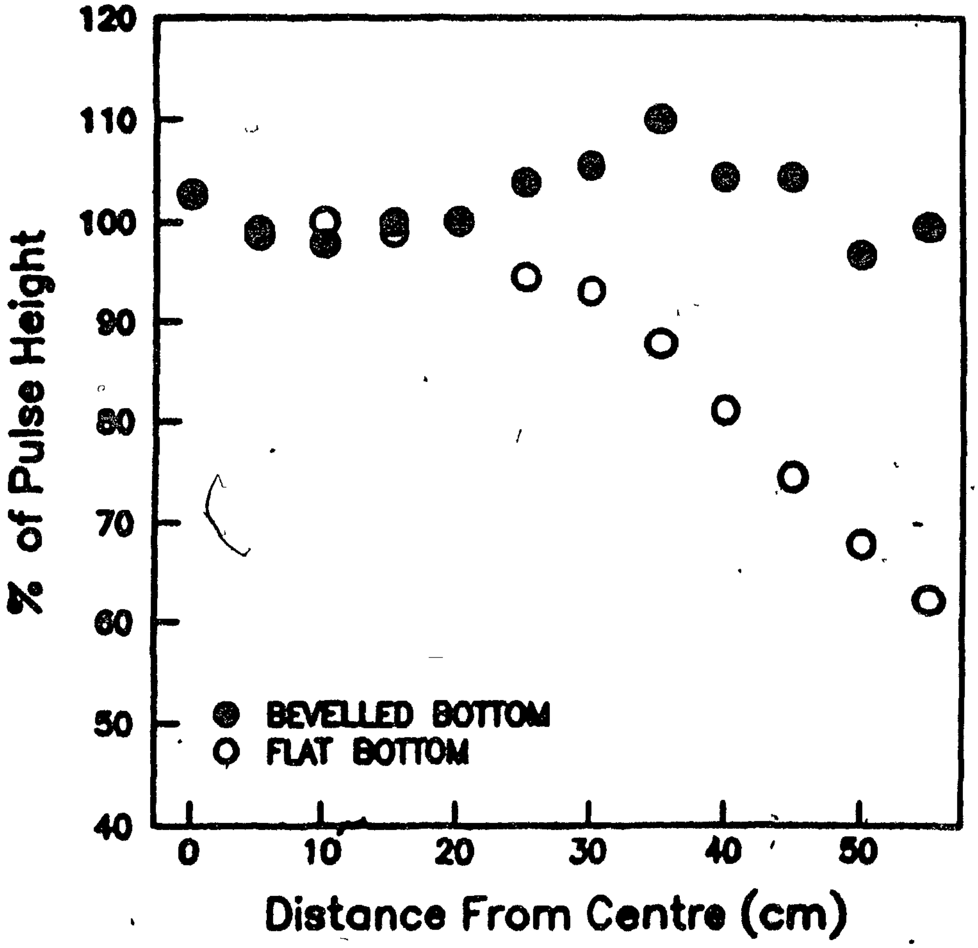

FIG 2.10: Mean pulse height versus distance from the centre of the detector for a flat bottomed scintillator dish as well as a dish with the structure shown in frgure 2.10

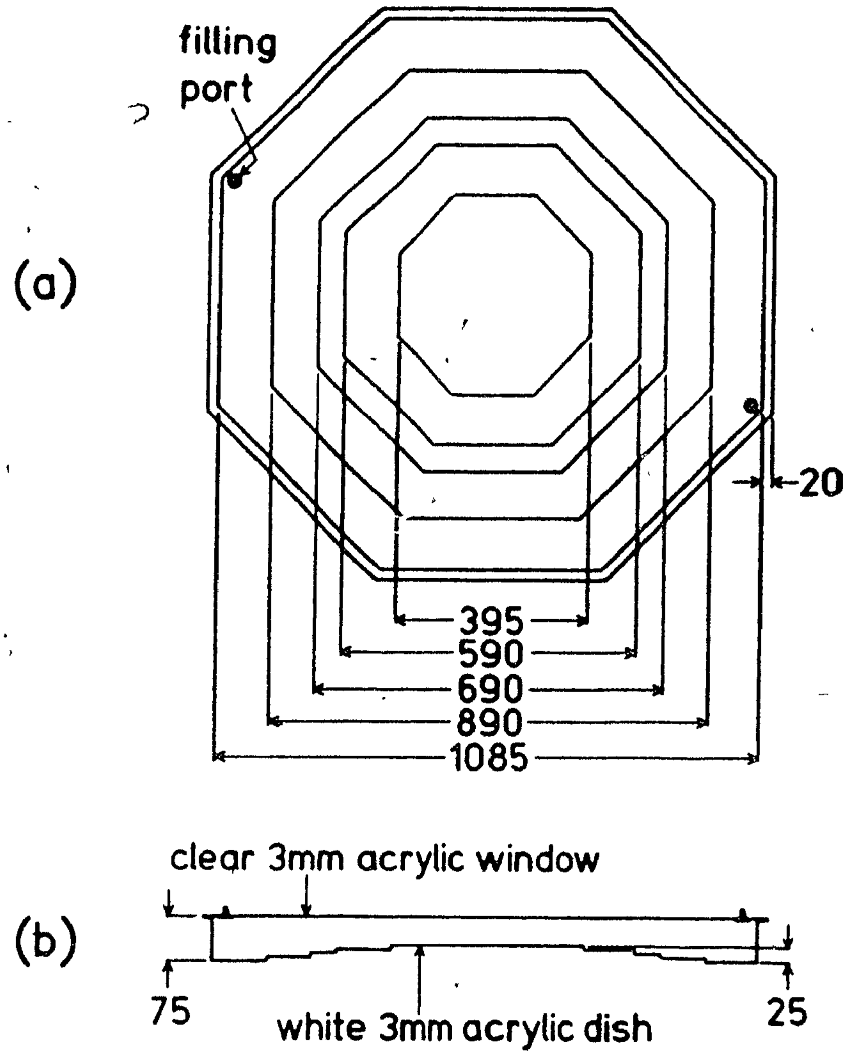

FIG 2.11: (a) Plan view of the final scintillator dish developed for the experiment. The distances are indicated in centimetres. (b) A vertical cross section of the dish.

Resulting Pulse Height Spectrum from the Final Detector

The single particle pulse height spectrum necessary for determination of the single particle spectrum was obtained by replacing the long trigger counter used to test the uniformity of response, by two small $7cm \times 9cm \times 2cm$ plastic scintillator blocks separated by a block of lead of the same dimensions. Each block of scintillator was viewed by a photo tube attached to one end. Trigger was provided only upon coincidence of the two photo tubes. The block of lead served to stop the soft components (e^+,e^-,etc) of air showers so that only high energy particles could pass through and trigger the detector. The trigger counters had small enough area that the probability of more than one particle passing through them simultaneously is small. The pulse height spectrum resulting from the data collected is a single particle spectrum and it shows a Landau distribution — rising rapidly and then decaying with a relatively long tail. The standard deviation was calculated by fitting a Landau curve to the distribution which is expressed analytically as follows:

$$\Psi(E) = const \times exp[-\frac{1}{2}(\lambda + e^{-\lambda})]$$

where, $\lambda = \frac{(E-E_P)}{\sigma}$,

E_P = most probable energy loss or mode of the distribution,

σ =standard deviation of the distribution.

The mean of the Landau distribution is given by:

$$E_m = E_p + 1.27\,\sigma$$

The single particle pulse height spectrum with the Landau fitted to it is shown in figure 2.12.

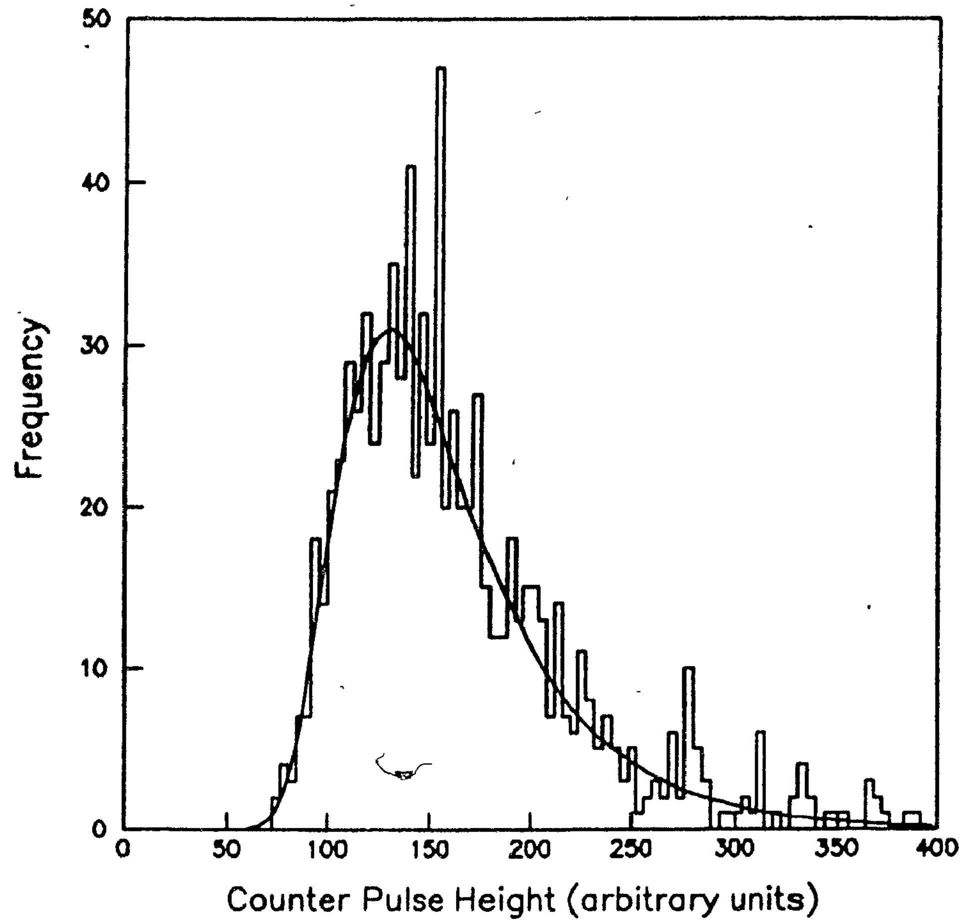

FIG 2.12: Pulse height distribution obtained with the prototype detector with an external triggering arrangement

Section 2(d): Effect of the Photo Tube Size on the Pulse Height Resolution

Having achieved a fairly high degree of uniformity of response and a well resolved single particle peak, a study was conducted to determine what effect the photo tube size had on the these factors. The procedure adopted was essentially the same as that described in the previous section. In determining the uniformity of response, using a small trigger counter meant moving the trigger counter beneath the detector to different pre marked positions. The data collected in this case could be read directly in terms of distance from the centre of the detector instead of time difference. The advantage of following this procedure is that detector resolution and its uniformity of response could be tested with the same set of data thus saving time. Data was collected with the bare tube and the trigger counter at four different gating positions: 0cm, 15cms, 30cms,and 50cms from the center of the detector. The size of the photo cathode was reduced by covering the photo tube with a thick opaque piece of black plastic with a circular hole in the center. Three different sizes of the photo tube were tested in this way using plastic with holes 10cm ,8cm and 6cm in diameter.

The mean pulse height at each position was plotted as a function of the distance from the center of the detector for each size of the hole to determine the effect of the photo tube size on uniformity of response. The results are shown in figure 2.13(a) and it is clear that there is no change in this factor with change in photo tube size. Amplitude of the pulse at zero position as the tube becomes smaller, does show a decline as can be seen from figure 2.13(a). The standard deviation also becomes smaller (figure 2.13(b)) showing that the single particle resolution (see figure 2.13(c)) which is the ratio of the standard deviation and the mean, is independent of the photo tube size.

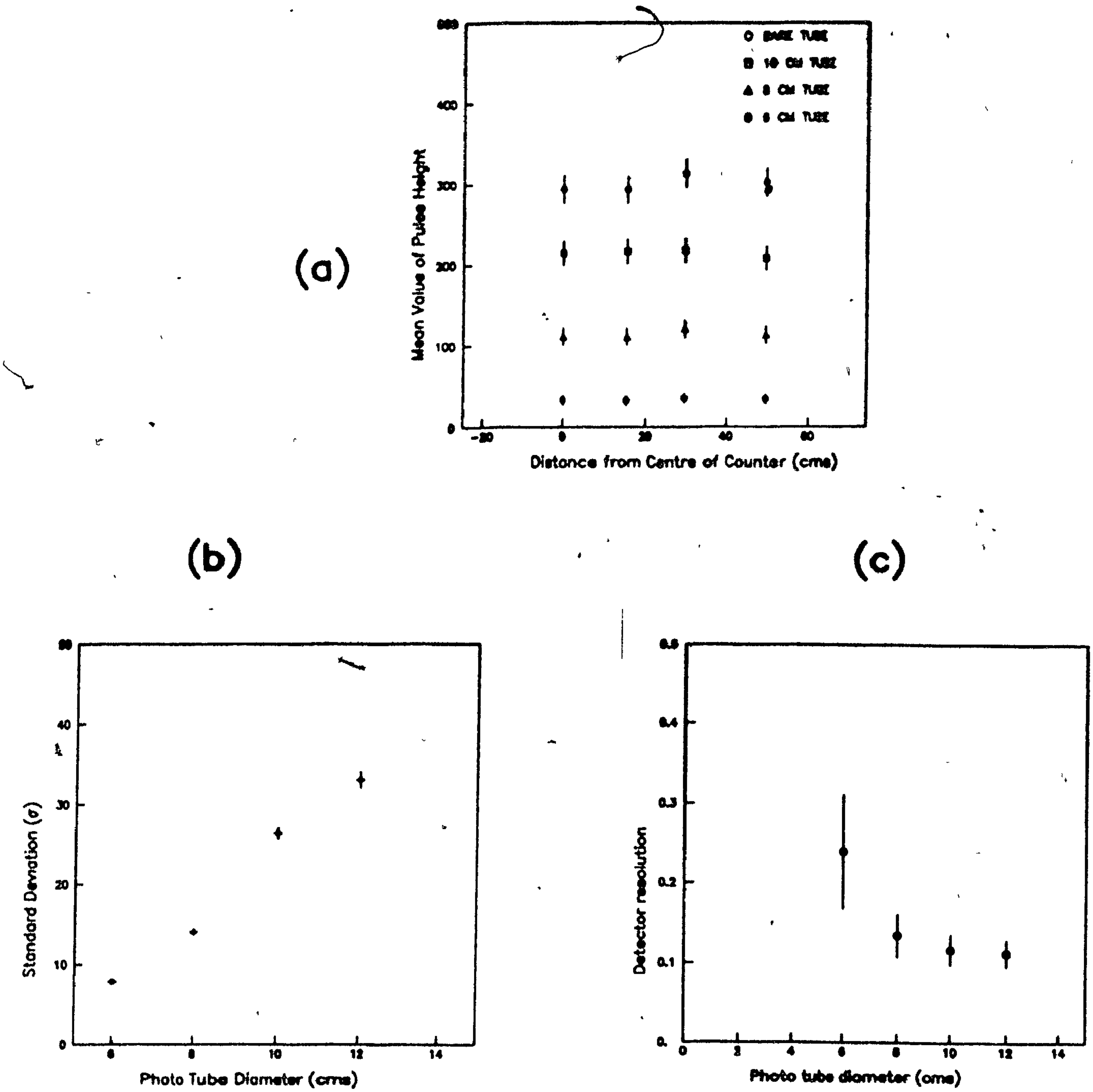

FIG 2.13: Effect of photo tube size on pulse height resolution of the detector. (a) Plot of the mean pulse height; (b) the standard deviation of the pulse height spectrum and (c) the detector resolution are plotted as a function of the photo tube size. The bare tube is equivalent to a 12 cm hole.

Temperature Dependence of the Detector Response

Since the actual array is located on a stretch of land with no weather protection, it was important to test if the detector functioned as well at low temperatures as it did under normal conditions. Pulse height spectra were obtained at six different temperatures, ranging from 0°C to 18°C. The resulting plot is shown in figures 2.14(a) and (b). The detector clearly shows no temperature dependence — the photo tube as well as the the scintillator obviously function well at low temperatures. This result did not come as any great surprise however, because of the fact that the scintillator that we use was specially developed to perform well at temperatures as low as -40°C. The photo tube is also designed to operate well at low temperatures. However, this study did confirm one important fact: di-chloroethane which is used to join the window to the dish is an excellent sealant and it succeeds in keeping the liquid scintillator well protected against moisture.

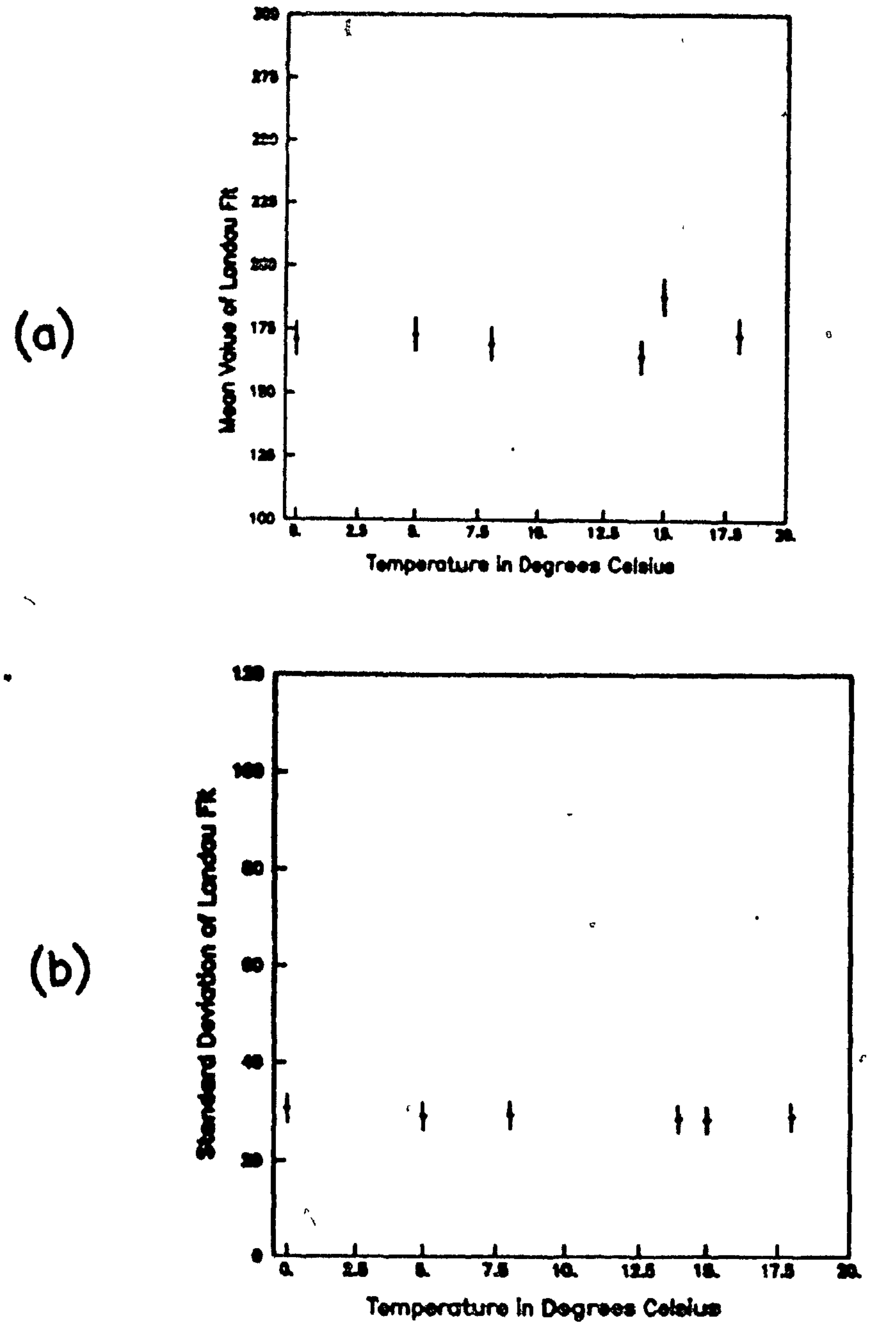

FIG 2.14: Effect of the temperature of the surroundings on the detector response. (a) Plots of the mean and (b) the sigma of the landau fits were obtained at five different temperatures.

3. THE LEDA ARRAY

Section 3(a): Location and general layout

The experiment is carried on using detectors identical to the one described in the last chapter. There are 19 detectors at present in the array arranged in the form of a regular hexagon with the central (longest) row consisting of 5 detectors (see Figure 3.1). There is a distance of roughly 43 metres between each detector and its nearest neighbour. So the longest row is 172 metres in length. The strange choice of grid size is due to the location of the experiment since we are bound on one side by a steep cliff and on the opposite side by a country road(the grid size was intended to be 50 metres, not 43). The experiment is located on land belonging to the McGill School of Agriculture, the Macdonald College, and is next to the McGill Weather Radar Observatory (the Radar center, in short) . The site is about 40 kilometres west of McGill University near the town of St. Anne de Bellevue. The land that is not occupied by the detectors is still used to grow corn and around August, it is a major feat to be able to locate the detectors amidst the tall stalks of corn.

One of the advantages of this site is that the land is approximately level and the maximum vertical height difference being less than a metre; this allows for equal acceptance in all directions and also means that timing considerations at the trigger level are simplified. But the biggest advantage by far is the fact that such a large area($\sim$ 20,000 m^2) of unoccupied land allows us to have a symmetrical array. A symmetrical array allows us to have as simple a trigger as we choose, besides making acceptance uniform over the face of the array. A counter array with unsymmetrically located

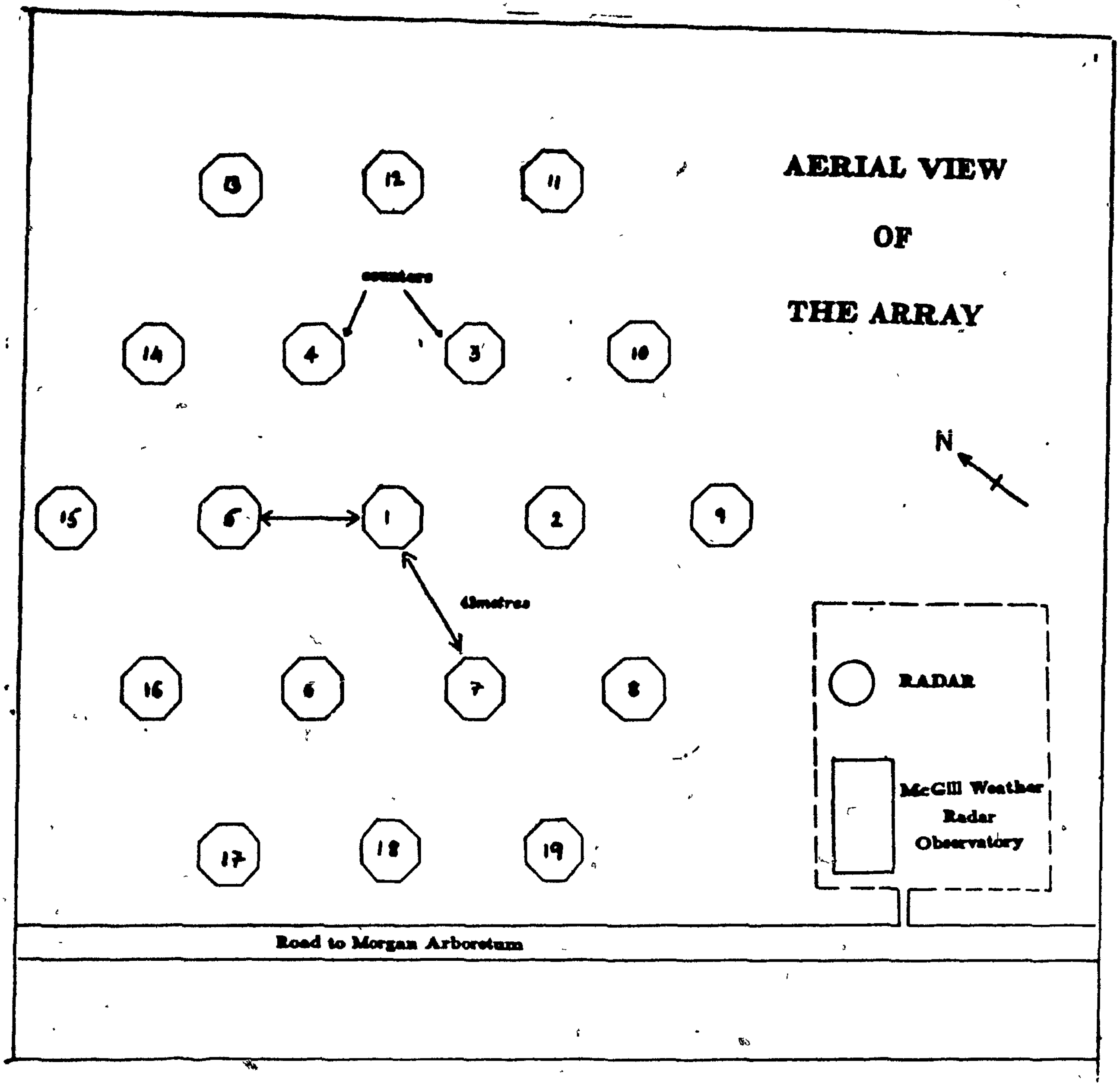

FIG 3.1: The LEDA array with nineteen detectors arranged in a hexagon. The electronics hut is located close to the central detector.

detectors does not have this advantage. The relatively large* grid size places constraints on the size(i.e the energy) of the shower that we are capable of detecting. As will be shown later,this array is not capable of detecting small($< 10^{15}eV$) showers. However, preliminary studies done by the Chicago group show definitely that the signal to noise ratio (γ-ray/nuclei) improves as we go to higher energies and this is definitely an asset[24]. The desire to have as large a collecting area as possible with a limited number of detectors was a main factor in the choice of grid size. The LEDA array was originally intended as an exercise to gain much needed experience with triggering an extended detector, operating out of doors, etc., for the DUMBO project (Deep Underground Muon Bundle Observatory). The project was not funded.

The hut containing the electronics is located near the central detector, which is labelled detector 1. The labelling scheme is shown in Figure 3.1. Each detector has two cables connecting it to the electronics hut. The signal cables are the RG58 coaxial cables and the high voltage cables are the coaxial RG59 type. Power to run the electronics and to maintain normal temperatures in the hut is drawn from the Radar center using three 14-gauge power cables specially ordered for this purpose.

Canadian weather being what it is, adequate precautions had to be taken to protect the equipment from it. The electronics hut is very well insulated with fibre glass and is equipped with a space heater and an air conditioner. The hut being only $1.22m \times 2.44m \times 1.83m (4' \times 8' \times 6')$ in dimensions, we found that the heat generated by the electronics when the experiment is 'on' is more than sufficient to keep the place

---

* **The array at Dugway, Utah proposed by the Chicago group has a grid size of 10 metres.**

warm. The detectors themselves do not need any special weather protection because both the 'active' components – the photo tube and the liquid scintillator were carefully chosen to perform well at low temperatures. It is necessary however, to protect the photo tubes and the detector as a whole from direct light and wind, rain and of course snow.

Section 3(b): The Counters

The assembled detector appears as shown in figure 3.2. The dish containing liquid scintillator 'sits' on a $1.22m \times 1.22m (4' \times 4')$ wooden platform which is firmly screwed on to four wooden legs that are weather treated and buried 1 metre into the ground. Each platform has a small hole at one corner to allow cables to pass through. The platforms are levelled at the time of installation and are covered with a piece of thick black plastic on the inside. On the layer of plastic is placed a piece of aluminium mylar cut to the shape of the scintillator dish. The dish is placed on the top of the layer of mylar. The light collecting cone is placed on the dish and the photo tube is placed on the cone looking down into the scintillator dish. The assembled detector thus has three parts: the dish, the light collecting cone and the phototube. This arrangement is covered with a cover ('the shroud') made out of black plastic to make it light tight. Great care is taken when the shroud is being made to ensure that there are no holes in it and it is tucked under the dish where possible or otherwise stapled to the platform so that the arrangement is as light tight as possible. Once this is completed, the detector is enclosed in a pyramid made of galvanized steel. This setup has the following advantage: any light that leaks inside and falls on the platform is absorbed by the black plastic. The few scintillation photons that do pass through the bottom of the dish (which is semi-translucent) however, are reflected back to the inside of the detector by the highly reflecting mylar layer and this increases the efficiency of the detector by about 20% (ref Chapter 2).

The pyramid has four sides, trapezoidal in shape with a vertical height of approximately 122 cm(4 feet) so that they can be cut without waste from a four feet wide roll of steel. The four pieces can be screwed together and as additional protection the top of the pyramid has a rectangular piece of steel $25cm \times 30cm$ (called the 'cap') screwed on to it. The pyramids are sealed at the joints with duct tape after they are assembled. The platform on which the counter sits has border along the edges which is beveled at an angle to match the pyramid and so the pyramid when placed, rests firmly on the platform. The pyramid is secured to the platform with wood screws. Figure 3.3 shows the various parts of the pyramid. The assembled pyramid weighs about 10 kilograms and can be easily removed by two people if any detector needs servicing.

The operation of filling the dish with scintillator takes place once the platform is installed. Liquid scintillator is known to perform poorly when contaminated with oxygen and so to avoid this the dishes are purged of air using dry nitrogen prior to filling. During the process of filling, a siphon is used and again nitrogen is used to push the liquid scintillator into the dish, thus eliminating any risk of oxygen contamination. Each dish is filled with 45 litres of liquid scintillator and this leaves a layer of nitrogen about 2cm thick in the dish between the scintillator surface and the window of the dish. The layer of nitrogen acts as a buffer and protects the dishes by accommodating the pressure due to expansion of the liquid scintillator.

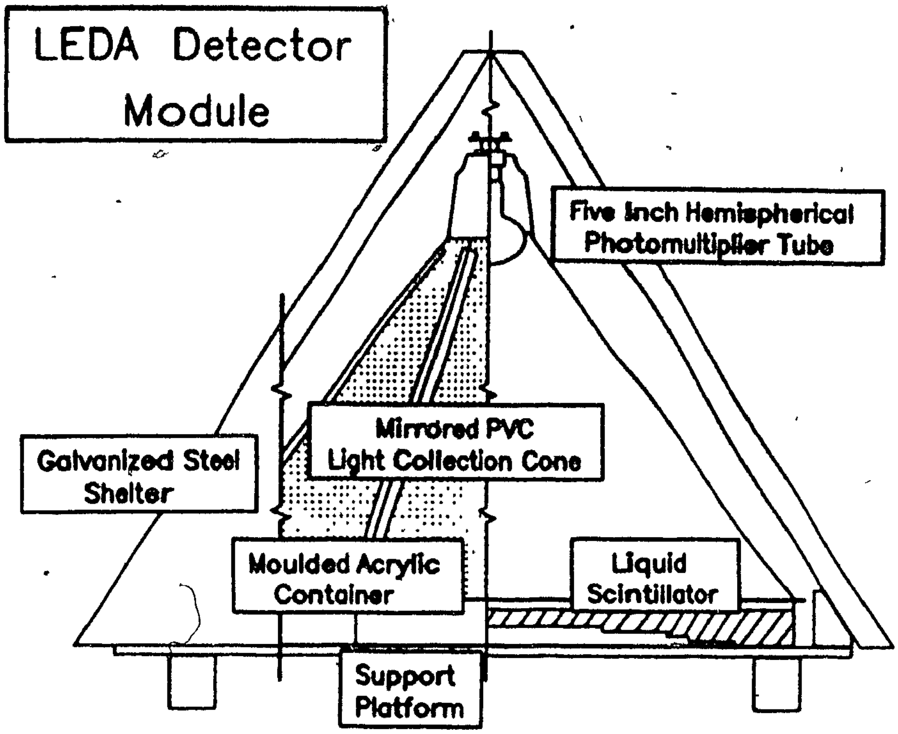

FIG 3.2: A cross sectional view of the prototype detector.

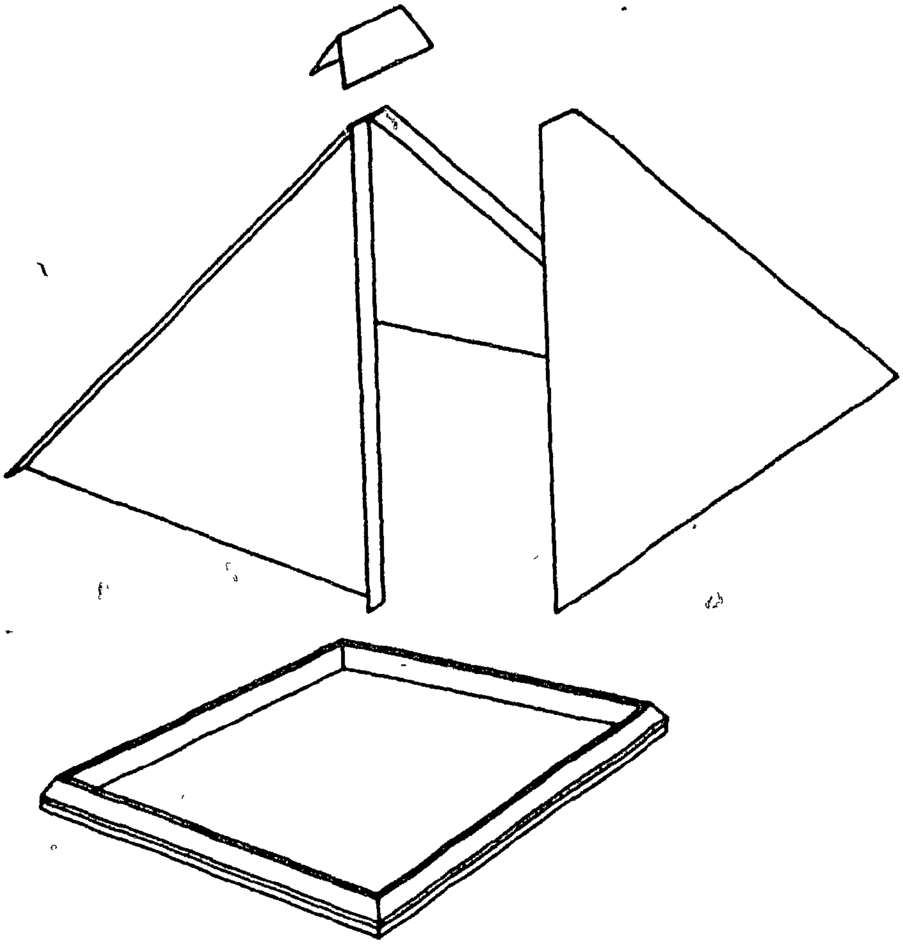

FIG 3.3: Various parts of the steel pyramid used to protect the detector from wind and snow.

Section 3(c): The Electronics

Particles in the shower front of an air shower travel in the form of a disk or a 'pancake' of finite thickness and spread, depending upon the depth of the atmosphere at the place of observation. Consider three collinear detectors placed a distance 'd' apart as shown in figure 3.4. A shower whose axis makes an angle θ with the vertical upon reaching the detectors would cause detector A to fire first and B to fire next after a time interval of $\frac{d}{c} \times sin\theta$, where c is the velocity of light. Only in the case of vertical incidence would each detector fire simultaneously. Showers with zenith angles up to 30° are accepted as 'good' showers since at larger angles, the amount of atmosphere traversed would be unacceptably high (Beyond 30° a shower of energy 3×10^{14}eV produces a shower of the same size as a vertical shower of one thirds that energy.[24]).

A sensible trigger for the hardware should have its threshold on one of the inner counters for the following reason: firstly, the outer counters are connected to the electronics with 100 m long cables, the inner counters use cables half that length. Signals travel in the RG58 cables with two thirds the velocity of light. So signals from the outer counters reach the electronics 250 ns later than those from the inner seven. Consequently, with the threshold for the trigger set on any one of the outer counters, numerous delays would be needed to ensure that signals from the inner seven reach the digitizing electronics after the event has passed the threshold test and gates have been generated. The second reason is related to the fact that the shower particles are concentrated near the core of the shower and such a requirement automatically biases the core of the shower to be inside the array. This fact, as will be seen later, is crucial for reliable estimation of the shower size and hence its energy.

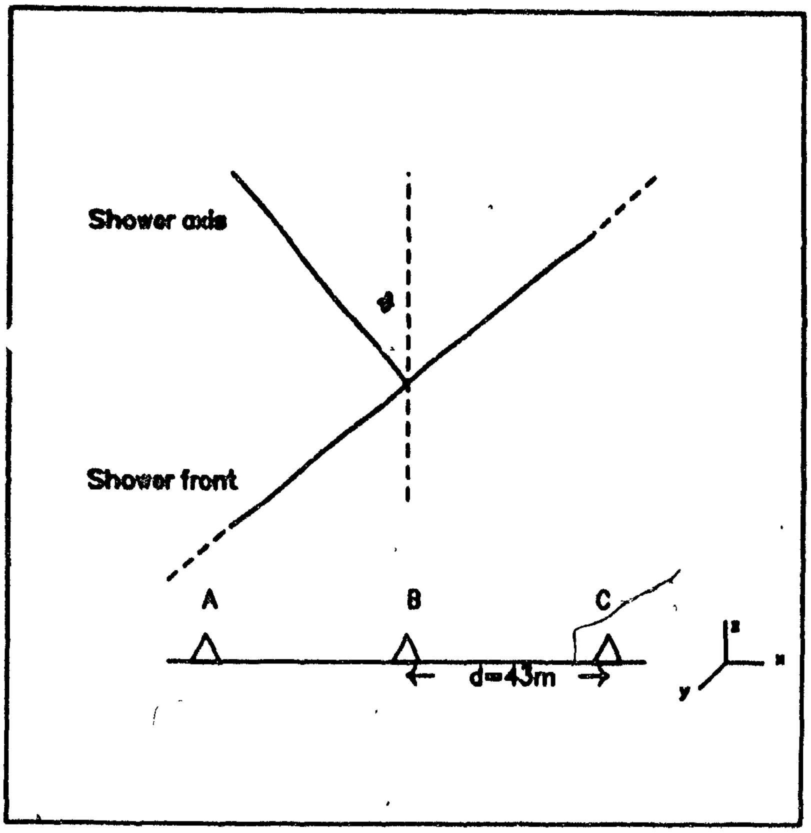

FIG 3.4: A shower front incident at an angle θ on an array of three colinear detectors

The disadvantage of having a simple hardware trigger is the high event rate which results. More details about this will be given in a later section in this chapter. The basic hardware trigger requires at least one inner counter to go above the discriminator threshold. Once this condition is satisfied, the on-line filter requires at least three counters in the array to receive a pulse height equivalent of half a particle. A data set that passes both these conditions is recorded on diskette. Raw data collected with this trigger is subjected to further off-line cuts during analysis using secondary hardware triggers that will be discussed later. The electronics used to record data consists of the following hardware components:

1. **The high voltage supply [LeCroy HV4032A]** is used to supply the phototubes with appropriate voltages. LeCroy HV4032A is a programmable, microprocessor controlled high voltage power system that is specially designed for photomultiplier applications. It houses 32 channels and is provided with a battery backed up memory that is capable of storing the voltages for 24 hours should the main power go off.

2. **4:1 signal splitter:** As is obvious from the name, the splitter is used to divide the signal into two parts, one four times the other. This is achieved with the help of appropriate resistors.

3. **Discriminators [LeCroy 623B]** : discriminators are used to filter out signals that are below a preset threshold. NIM 623B is an eight channel discriminator with a minimum threshold of -30mV and a maximum threshold of -1V. The threshold on each channel can be adjusted with a front panel screwdriver adjustment and it remains stable to <.2% per °C. The width of the discriminator output can be

adjusted via a front panel screwdriver adjustment and can range from less than 6 *ns* to greater than 150 *ns*, with a typical rise time of 2.1 *ns* . For an output of minimum width, the device responds to a second pulse within 9 *ns* of the leading edge of the first pulse.

4. **Delays** that signals from each counter have to pass through are calculated with the help of a Monte Carlo simulation of the shower process that will be described later. The required delays are achieved by taking appropriate lengths of RG58 cables and coiling them so that they fit into a specially constructed delay box. A delay of 100 *ns* is achieved by connecting two 50 *ns* delays in series. A 50 *ns* delay requires 10 *m* of RG58 cables.

5. **Gate Generator [LeCroy model 222]:** Dual gate and delay generator is used to provide the start or the gate pulses to start the ADC and the TDC. The gate width is adjustable with the help of a range switch and a potentiometer for fine adjustment. The width can range from 100 *ns* to 11 *s* . We use 650 nsec. Model 222 is packaged in a NIM standard housing and fits into the standard NIM bin.

6. **Fan in Fan out [LeCroy model 429A]:** The fan in fan out is simply a multi input logical OR gate. Model 429A can be fitted in a single width NIM module.

7. **Analog to Digital Converters(ADCs) [LeCroy model 2249W]:** Signals coming from the photomultipliers are integrated and scaled with the ADCs .This is achieved in the following way: an integrating capacitor is charged up with the signal of interest while a linear gate is on and then it is discharged at a constant rate while pulses from an oscillator are gated into a scaler. The final count of the scaler is proportional to the charge stored in the capacitor originally. The model

2249W is a 12-channel ADC capable of operating between gate widths of 30 *ns* and 10μs and maintains linearity to signals as large as -2V. The ADC is packaged in a standard width CAMAC module and can be plugged into the standard CAMAC CRATE.

8. **Time to Digital Converters(TDCs) LeCroy 2228A:** To fit a direction to the shower front, the times at which counters in the array fired have to be recorded and this is done using TDCs. The TDC works on the following principle: a common start pulse initiates a constant current source that charges up a capacitor. A stop pulse provided by the discriminated output of the photomultiplier terminates the charging. The charge on the capacitor is an analog measure of the time interval between the start and the stop pulses. This analog measure is digitized using the same technique (which is known as the Wilkinson rundown method) as used for the ADCs yielding a count proportional to the time interval. Model 2228A is an 8 channel TDC and measures time from the leading edge of the common start pulse to the leading edge of the individual stop pulses. Model 2228A has three selectable full scale time ranges of 100, 200 and 500 *ns* which have resolutions of 50, 100 and 250 *ps* respectively.

9. **Crate Controller [CAMAC 3912]:** The crate controller is an interface between the computer and the CAMAC crate that houses the ADCs and the TDCs. It occupies two slots at the right hand end of the the CAMAC crate. The crate controller is also equipped with an external event interrupt facility that enables it to record the occurrence of an event in real time, i.e in seconds past midnight.

10. **The computer** that processes and records data is the LSI-11 10-Bit microcom-

puter. The entire system which is the LSI-11, consists of the microcomputer, an RT11 operating system, a console for operator intervention, and is equipped with a two-diskette diskette drive.

A block diagram of the electronics is shown in figure 3.5. Signals arriving from each counter are split into two parts with the 4:1 signal splitter. For the inner seven, the $\frac{1}{5}$ part passes through a 100 ns delay to the ADC recording density information. For the outer twelve, the signals bypass the delay and are fed directly to the ADC. The $\frac{4}{5}$ part for the inner seven is split equally, one part of it going via a low level discriminator set at -30mV through another delay to the TDC. The other part passes through a high level discriminator set at -200mV to a seven fold OR(the Fan-in-Fan-out). Output from the OR is fed to the gate generator whose output is a pulse 600 ns wide that is the start pulse for the TDC and the gate for the ADC. The $\frac{4}{5}$ part from the outer counters passes through the low level discriminator and is fed directly to the TDC (to minimize time slewing effects[27]). Outputs from the ADC and the TDC are processed by the computer and accepted events are recorded on the data disk along with the time of occurrence of the event.

Appropriate delays, discriminator levels and gate widths required to operate the system were determined with the help of a Monte Carlo simulation which is described in the next section.

Shower Monte Carlo - Determination of the Gate Widths and Delay Requirements

Referring back to figure 3.4, a shower travelling with the velocity of light making

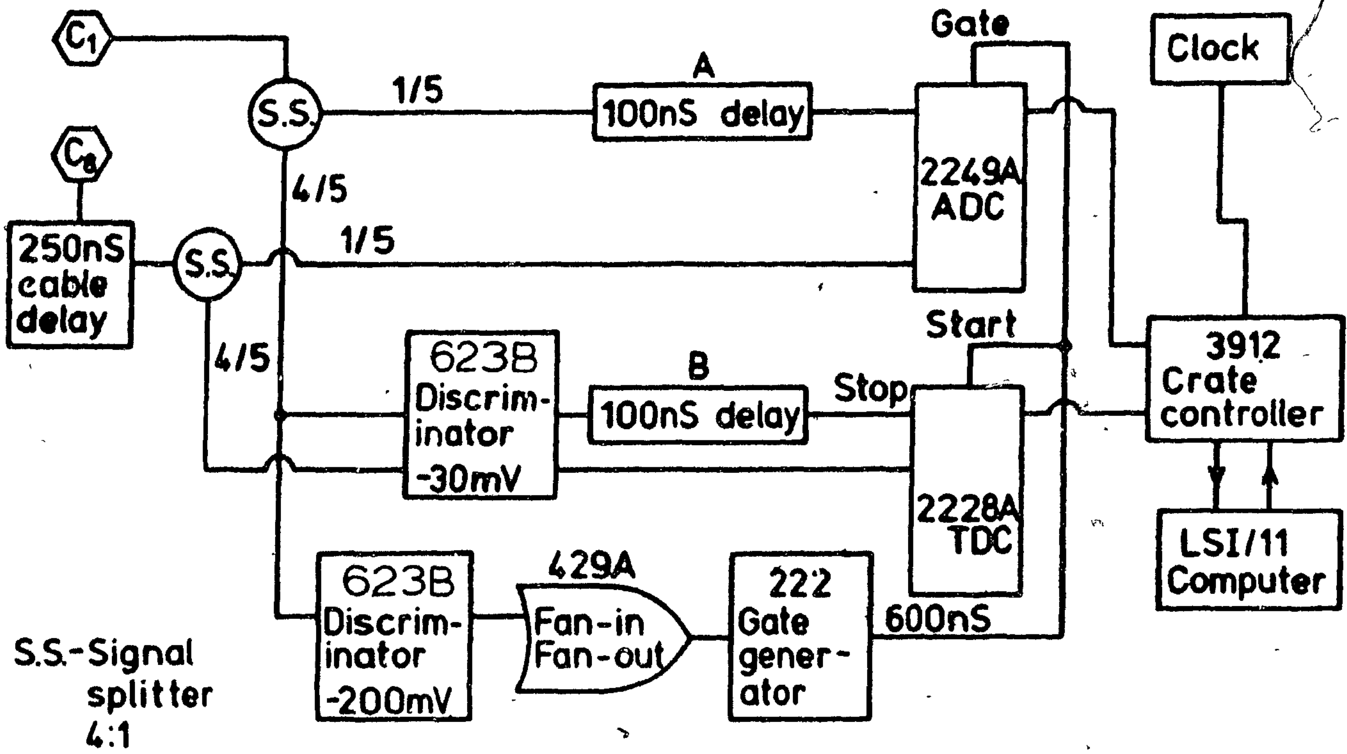

FIG 3.5: Schematic diagram of the electronics used to record data. C_1 and C_8 stand for inner seven and outer twelve counters respectively.

an angle θ with the zenith would have a velocity of $\frac{c}{sin\theta}$ along the x direction. For such a shower, the times at which the counters A and B fire will differ by $\frac{d}{c} \times sin\theta$. So, in order to accommodate showers with zenith angles $0 \leq \theta \leq 30°$, time shifts that have to be accommodated are $0 \leq t \leq \frac{d}{2c}$. In our case, since d is 43 metres, this gives $0 \leq t \leq 70ns$ for two neighbouring detectors. The gate must be wide enough to allow all signals to be recorded without chopping off the end of a pulse. In addition, some counters not in the trigger may produce pulses that arrive before the trigger. These pulses must be delayed appropriately so as to be properly recorded by the ADC and the TDC.

In the simulation, random showers with θ between 0 and 30 degrees and azimuthal angle ϕ between 0 and 360 degrees were generated uniformly, flat in $cos\theta$ and ϕ, and flat in rdr for $0 < r < 100m$ from the center of the array. Each set of values (θ, ϕ) determines a unit normal to the plane of the shower front and is given by:

$$\hat{n} = sin\theta\, cos\phi\, \hat{i} + sin\theta\, sin\phi\, \hat{j} + cos\theta\, \hat{k}$$

where $\hat{i}, \hat{j}, \hat{k}$ are unit vectors in the x, y, z directions respectively.

When the shower passes the origin, then the point on the shower front above a counter at $(x_c, y_c, 0)$ have the coordinates (x_c, y_c, z_c). A line from this point to the origin lies in the plane of the shower front and is hence orthogonal to the normal $\hat{n}$:

$$\hat{n}(x_c\hat{i} + y_c\hat{j} + z_c\hat{k}) = 0$$

or,

$$x_c\, sin\theta\, cos\phi + y_c\, sin\theta\, sin\phi + z_c\, cos\theta = 0$$

or,

$$z_c = -(x_c\, cos\phi + y_c\, sin\phi) tan\theta$$

The effective velocity of the shower in the z-direction is given by:

$$v_z = \frac{\Delta z}{\Delta t} = \frac{c}{cos\theta}$$

So, if the time at which the shower front passes the origin is defined as time $t = 0$, then a counter at $(x_c, y_c, 0)$ would be hit at:

$$t_c = \frac{z_c}{v_z} = -(x_c cos\phi + y_c sin\phi)\frac{sin\theta}{c}.$$

The Monte Carlo generated events, populated counters and checked to see if the shower satisfied the trigger conditions. The trigger condition requires at least one inner counter to have a minimum of N_1 particles and at least N_t counters in the array to have at least $N_2\,(N_2 < N_1)$ particles. When a shower was accepted, the time at which each counter in the array fired was determined. Since the trigger is provided by a counter in the inner circle, the counter in the inner seven that passed the threshold cut and recorded the lowest time is taken as the counter that started the experiment for that shower. This time is taken as zero time and is subtracted from all times. The new times are histogrammed and the results appear as shown in figure 3.6(a) and 3.6(b) corresponding to counter 1 and counter 11 respectively.

As expected, there is a distinct difference between the histograms corresponding to the inner seven and the outer twelve. Each counter in the inner seven shows a sharp peak at zero time corresponding to the events when that counter was the first to fire. Negative times indicate events when the shower front crossed the counter before it

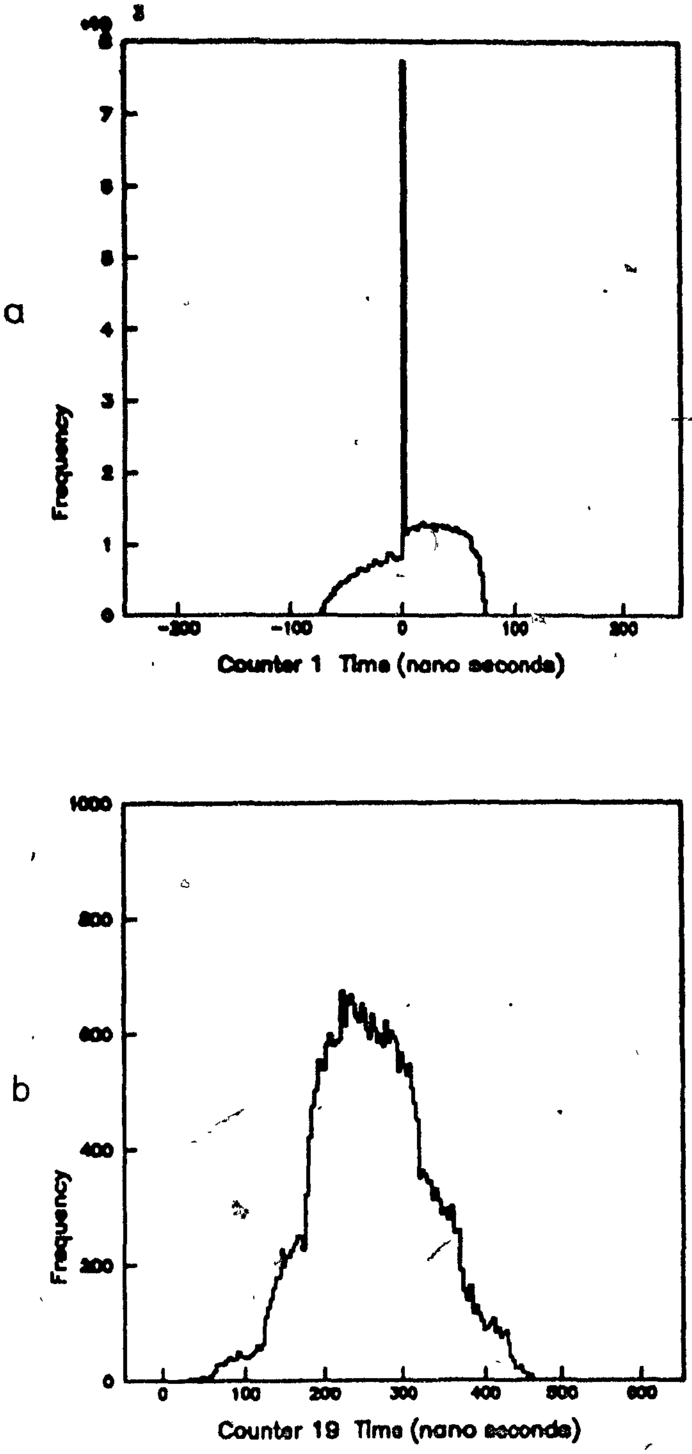

FIG 3.6: Monte Carlo of the times recorded by (a) a counter in the inner circle and (b) a counter in the outer circle of detectors in the array.

passed the origin, populating the counter with particles sufficient to pass the low level trigger but not the high level. All counters in the outer twelve have positive times only because of the extra 250 *ns* that signals from these counters have to pass through in order to ensure that they arrive after the ADC gate pulse and the start for the TDC. Notice that there is a time difference of ~250 *ns* between the earliest time of the inner counter and the outer one. From the histograms it is also clear that to accommodate all signals, the gate must be approximately 500 *ns* wide. To accommodate non zero-width pulses, an additional 100 *ns* is added to the width. The signals arriving from the inner counters require a delay of 100 *ns* to be recorded.

Dead Time Problem

The combination of the hardware and the software trigger that filters data is relatively simple: it requires that at least one inner counter pass the high threshold discriminator (which is set at a level corresponding to 5 particles) and at least five counters of the nineteen receive at least half a particle. Data collected with these conditions is subjected to further cuts with another set of off-line trigger conditions at the time of analysis. Application of cuts in this manner has one serious disadvantage: it results in a very high event rate. The indiscriminate passing of data results in a loss of 'good' data due to the finite time taken by the system to reset itself after receiving a trigger pulse. This interval is called the 'dead time' of the system. The high level discriminator serves to reduce this problem and to bring the trigger rate to a more reasonable level. A good trigger rate would allow the computer to process an event before the next event was fed to it. To arrive upon such a trigger rate, a scaler was used to count the trigger rate and a graph was plotted between the trigger rate and the rate at which the computer processed the data. The trigger rate was varied by changing the discriminator threshold. The graph that resulted is shown in figure 3.7. The processing rate reaches saturation as the trigger rate goes beyond 80 per second. A trigger rate 10 per second was chosen as a resonable compromise between a low energy threshold and low dead time. This trigger rate requires a discriminator threshold of -300 mV and this was chosen as the threshold for the high level discriminator.

Section 3(d)Computer Program for Data taking

Figure 3.8 shows a block diagram of the computer program that is used to collect data. The initialization cycle involves, among other things, calculation of the ADC, TDC addresses, opening and naming the output file and setting up the mailbox. The mailbox is a sort of interface between the foreground and the background programs. The foreground program is the main program that actually collects the data following the steps shown in the line diagram. The background programs are not shown; these consist of a group of programs that, among other things, allow data transfer from the micro computer to the VAX. (Data accumulated over 24 hour period is transferred via a phone link to the VAX 785 located at the physics department.) Once the initialization is completed, the ADC, TDC buffers and the Inhibit circuits on the modules are cleared. With the application of a gate pulse the inhibit circuit prevents additional charge from entering the ADC, until that set of information has been processed. At this stage, the system is ready to accept data and it waits until an interrupt in the form of a Look-At-Me(LAM) signal is sent by the ADC.

With the arrival of the first interrupt, further interrupts are disabled until the data is processed. The program then executes the next three steps applying the trigger

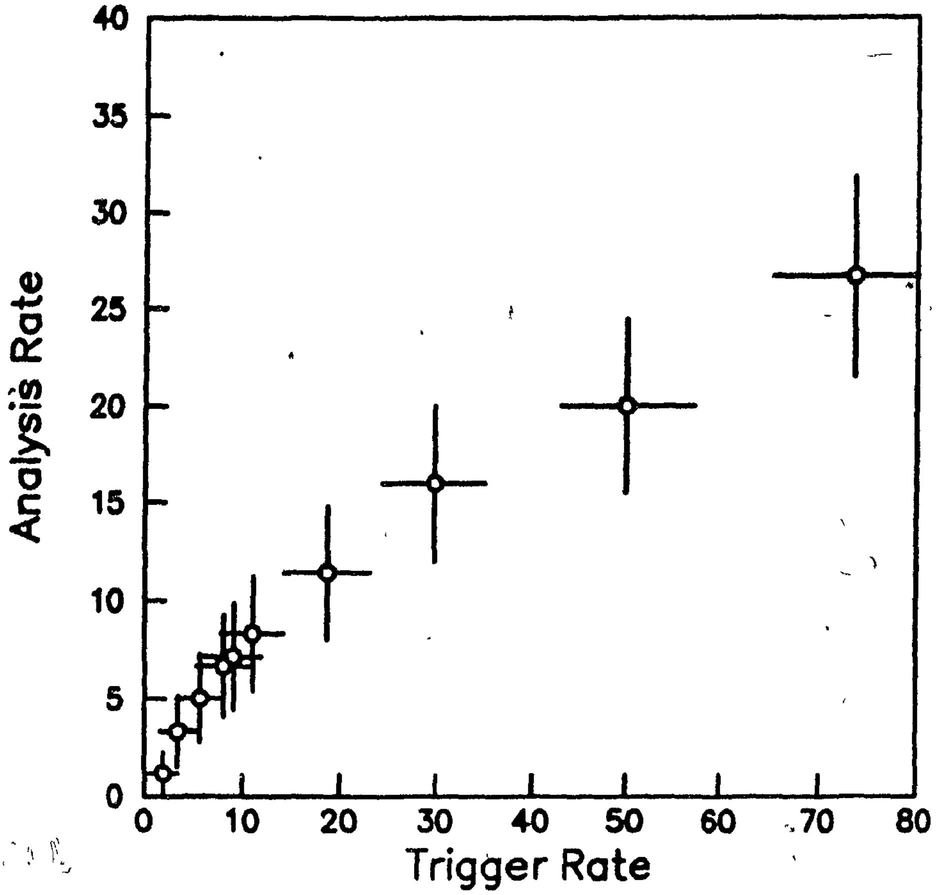

FIG 3.7: A plot of the computer analysis rate versus the trigger rate of the electronics.

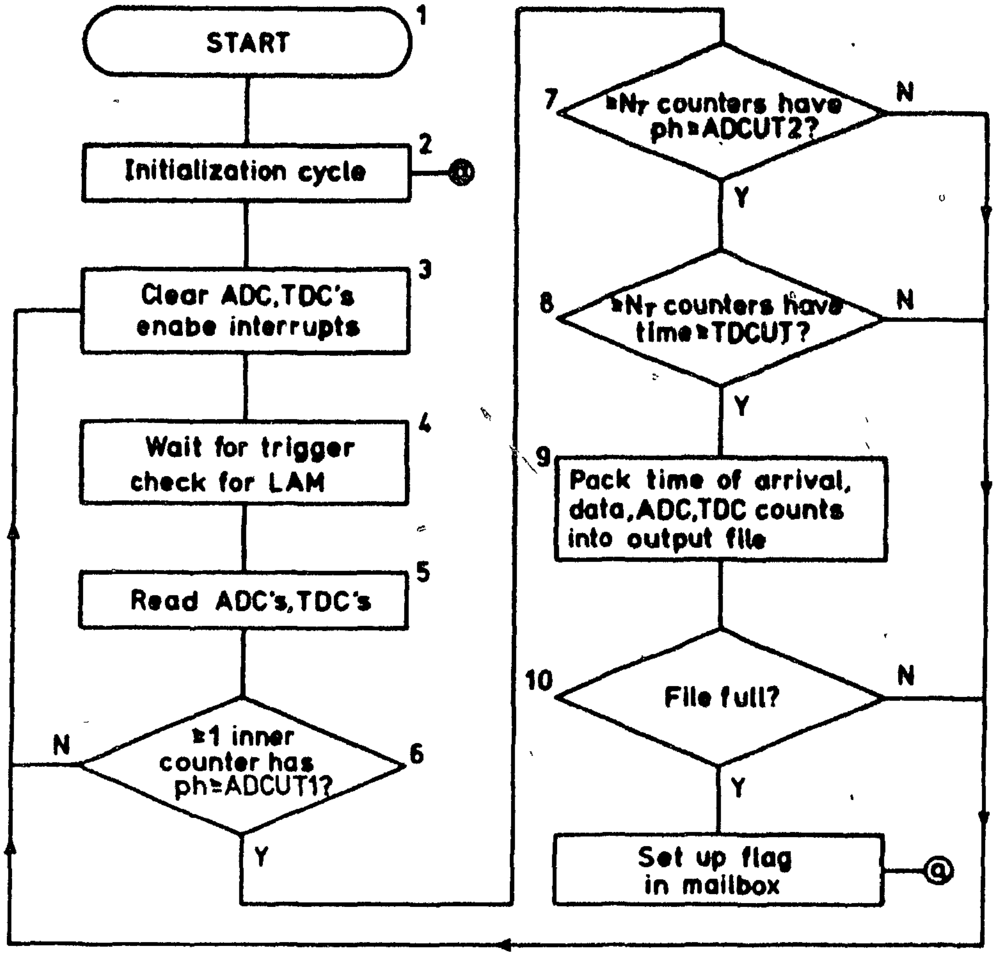

FIG 3.8: A flow chart diagram of the computer program used to collect data

conditions to test whether or not the data set received is acceptable. A signal set, to be accepted as 'good' data, must pass all three cuts; failure at any of the three stages results in the buffer being cleared and the system being reset to await the arrival of another set of data. If a signal passes all the cuts, then the ADC and TDC information along with the time of arrival are packed into the output file. Steps from 3 to 10 are repeated until the output file is full, when a flag is set up in the mailbox and the program returns to step 2 and opens a new output file. The flag is read by a background program and the file is stored temporarily on the data disk in the diskette drive until it can be collected and copied to the VAX via a modem and a telephone line. Since files stay on the data disk only temporarily, the disk can never get full and data collection continues with virtually no interruption.

Section 3(e): Preliminary Data Collection

Before proceeding to collect actual 'shower' data, several sets of preliminary data need to be taken to calibrate and standardize the detectors in the array. These involve:

1. Determination of the ADC pedestal;
2. Determination of the single particle spectrum of each detector;
3. Standardization of the response of all detectors in the array;
4. Determination of the noise cuts required by signals arriving from individual detectors;
5. Timing scans for each detector.

The last of the list given above is not described here because it does not apply to that aspect of the problem which is being dealt with in this thesis. Timing scans form part of another thesis written on the timing characteristics of the LEDA array[27]. Time data are necessary to determine the arrival direction of the primary. The times at which each detector in the array fired upon shower incidence is recorded and during analysis, converted to distances by multiplying with the velocity of light. A plane is fitted to this data and the direction of the normal to the plane gives the direction of the shower axis..

1. Determination of the ADC Pedestals

The pedestal of an ADC channel is the number of counts obtained when a gate pulse is applied to the channel and its analog input is terminated in a 50Ω. The effect of the pedestal is to boost the digitized output by the amount of the pedestal, resulting in outputs that are systematically higher than the real values. During analysis, this quantity must be subtracted from the pulse height recorded by the corresponding channel of the ADC. The pedestal is intrinsic to each channel of the ADC and for the Lecroy 2249W ADCs that we use, the pedestal can be adjusted to a low value with the help of trimming potentiometers provided for that purpose. The pedestal obtained from an ADC channel depends on the width of the gate applied and on the temperature of the surroundings*. That is, the pedestal of the ADC is not a constant quantity and it requires measurement frequently. Also, the pedestals from individual channels even when adjusted, show some fluctuation about the set value due to noise in the electronics making the process of setting difficult and liable to errors. So, rather than set ADC pedestals to values ~0, we set it to a low value, around 10, and used a simple program to record the ADC counts of each channel with the gate pulse on and the photo

---

* Lecroy ADC manual

multiplier voltage off. The pedestal data thus collected was histogrammed and mean of the distribution taken as the pedestal corresponding to that ADC channel. Figure 3.9 shows the histogrammed pedestal data for channel 2 of the ADC, corresponding to counter 3 in the array.

2,3. Determination of the Pulse Height Spectrum of each Detector

All the pulse height spectra described so far were determined with the help of two external trigger counters, placed vertically below the photo tube, underneath the scintillator dish. Though feasible, this procedure is somewhat impractical to be carried on in a field where detectors spread as far as 90 metres from the electronics hut. To find a more efficient way of determining the spectra, a study was done in the laboratory using the 'model' detector to determine the 'self triggered' counter pulse height spectrum and to compare its parameters with those of the 'externally triggered' counter. Figure 3.10(a) and (b) shows the results of the study for counter 11. The self triggered spectrum has a lower peak and higher standard deviation, but the mean of both the spectra are certainly comparable. This is the primary quantity that we are interested in, and this indicates that the pulse height spectrum can be obtained without the help of external trigger counters.

Having determined this, the next step was to standardize the detectors in the array so that all the detectors had approximately the same values of the pulse height spectrum peaks. This was done in the following way: pulse height spectrum for each detector were obtained for 8 different values of the photo tube voltage. Each spectrum was fitted to a Landau distribution and the values of the peak in the spectrum obtained from the fit was plotted as a function of the high voltage on the photo tube. The resulting plot

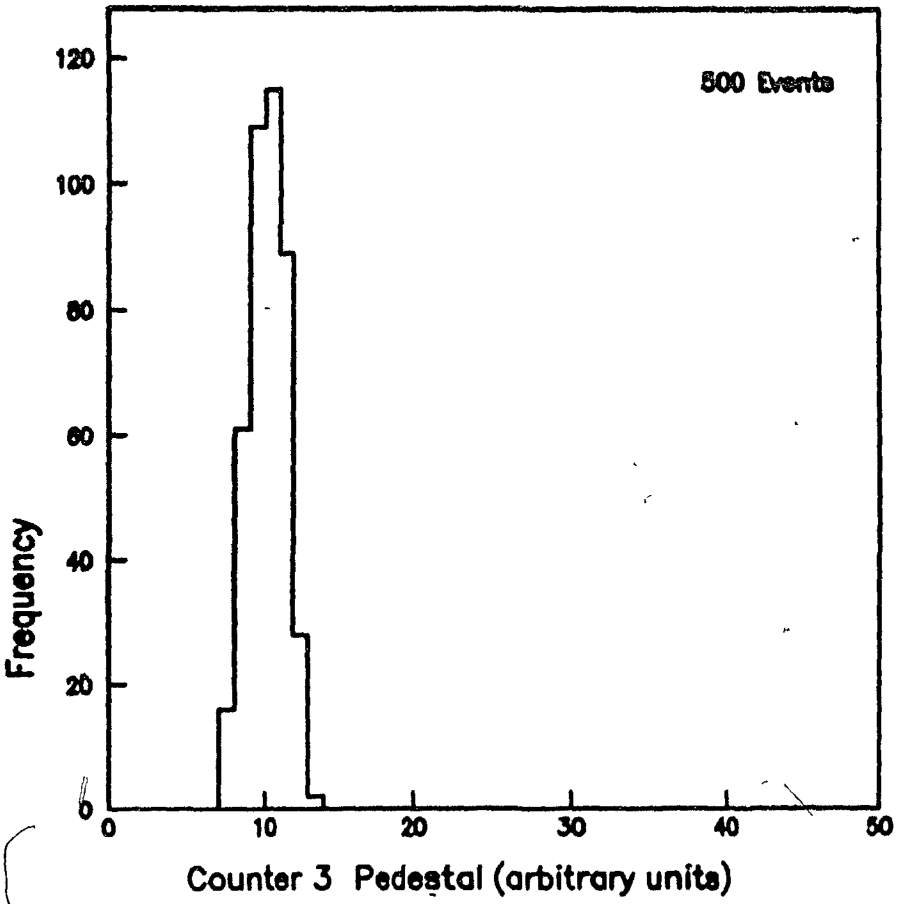

FIG 3.9: A histogam of the pedestal data recorded for counter 3 in the array.

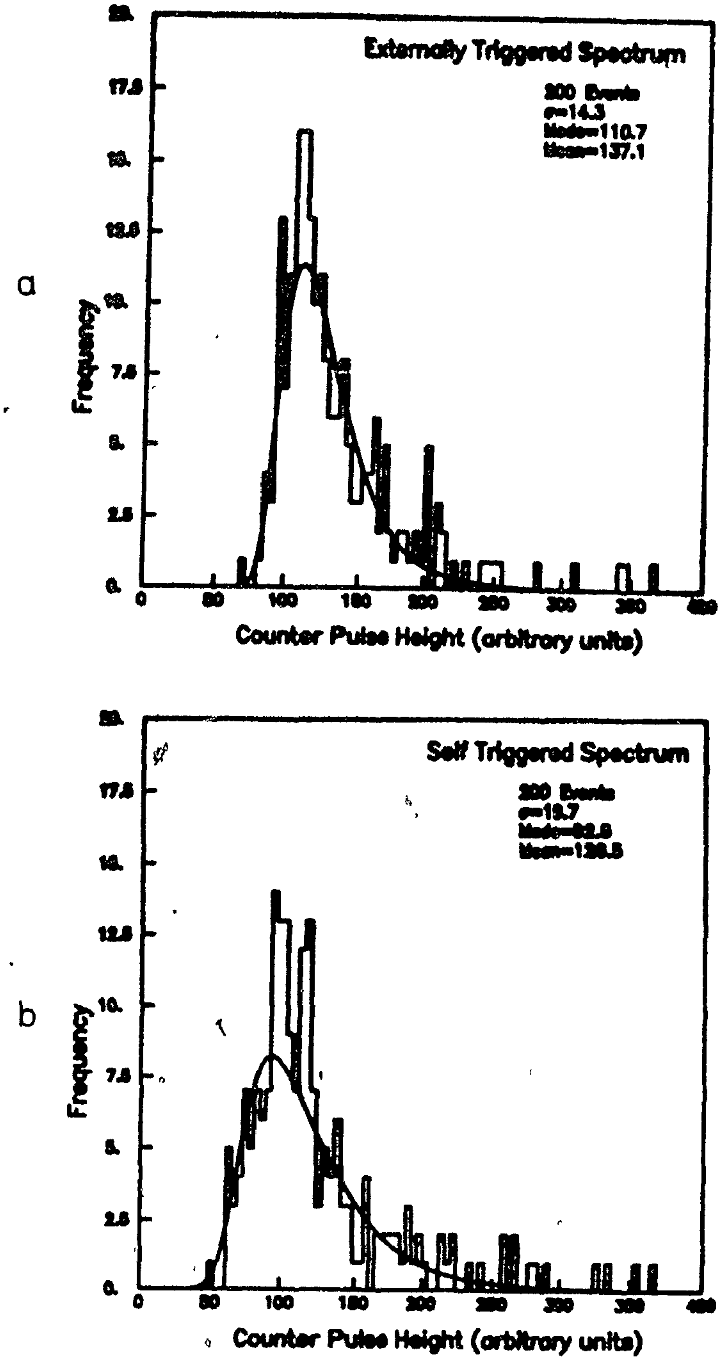

FIG 3.10: (a) Pulse height spectrum for counter 11 obtained by using an external trigger; (b) Pulse height spectrum for counter 11 obtained without an external trigger. A noise cut at 50 ADC counts has been made.

was fitted to a curve of the form:

$$ph = a + bv + cv^2,$$

where,

ph = mode of the pulse height spectrum,

v = voltage.

a,b,c = output parameters

Figure 3.11 shows the results for counter 1. The output parameters a,b,c were used to determine exactly the voltage v required to obtain a peak in the spectrum at 100 ADC counts.

4. Determination of Noise Cuts

The pulse height spectrum as shown in figure 3.12 shows a small secondary peak around 60 ADC counts along with the real peak. This secondary peak is the noise peak and is due to several factors like the photo tube dark current, the stray radio signals picked up by the long connecting cables used, etc. Clearly, noise is dependent to some extent upon the high voltage applied at the photo tube. Noise is an important factor in studies like the one described under the previous heading, because of the fact that observations are taken with voltages low enough to result in actual peaks that are close to the noise peaks. The need to determine the noise spectra arises out of the desire to obtain better fits to the pulse height spectrum and hence obtain a lower chi-squared. The noise cut for counter 11 can be seen in figure 3.12. The method of determining the noise cuts is fairly crude but efficient: the pulse height spectrum is obtained and the noise level determined by eye, and then in subsequent analysis, all points that

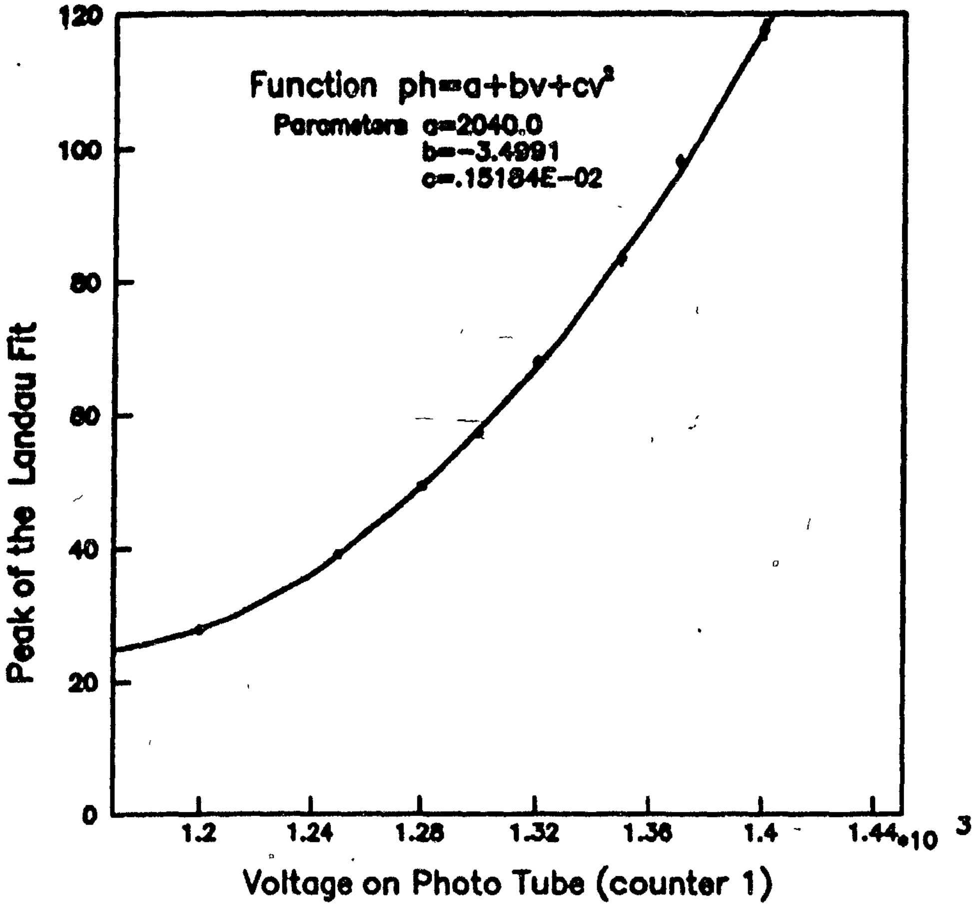

FIG 3.11: A plot of the peak of the pulse height spectrum for counter 1 as a function of the voltage applied on the photo tube.

fall below this threshold are rejected. Since this quantity depends so critically on the applied voltage, noise levels have to be determined whenever the photo tube voltage is changed.

Section 3(f): Description of the data set used

Once the preliminary data has been collected and the detectors in the array standardized, shower data is ready for collection. The data collection program has already been described in Section 3(d). Data is stored on floppy disk in the following manner:

1 The first four bytes contain the real*4 variable which indicates the time of arrival of the shower in seconds elapsed after midnight.

2 The next three bytes contain the pattern of counters hit by the shower and the total number of counters that were hit.

Byte #	Bit #	Interpretation
1	0-7	counter 1-8 fired?
2	0-7	counter 9-16 fired?
3	0-2	counters 17-19 fired?
3	3-7	# of counters that fired

3 The ADC and TDC values for each counter that was hit is stored in three bytes per hit counter— so there are (3×the number of hit counters) in this section.

Byte #	Bit #	Interpretation
1	0-7	low bits of ADC
2	0-3	high bits of ADC
2	4-7	low bits of TDC
3	0-7	high bits of TDC

This condensed form of data is packed into 20cm (8″) floppy disk. Each disk has the capacity for holding 10 files of data — each file contains an average of 10,000 such

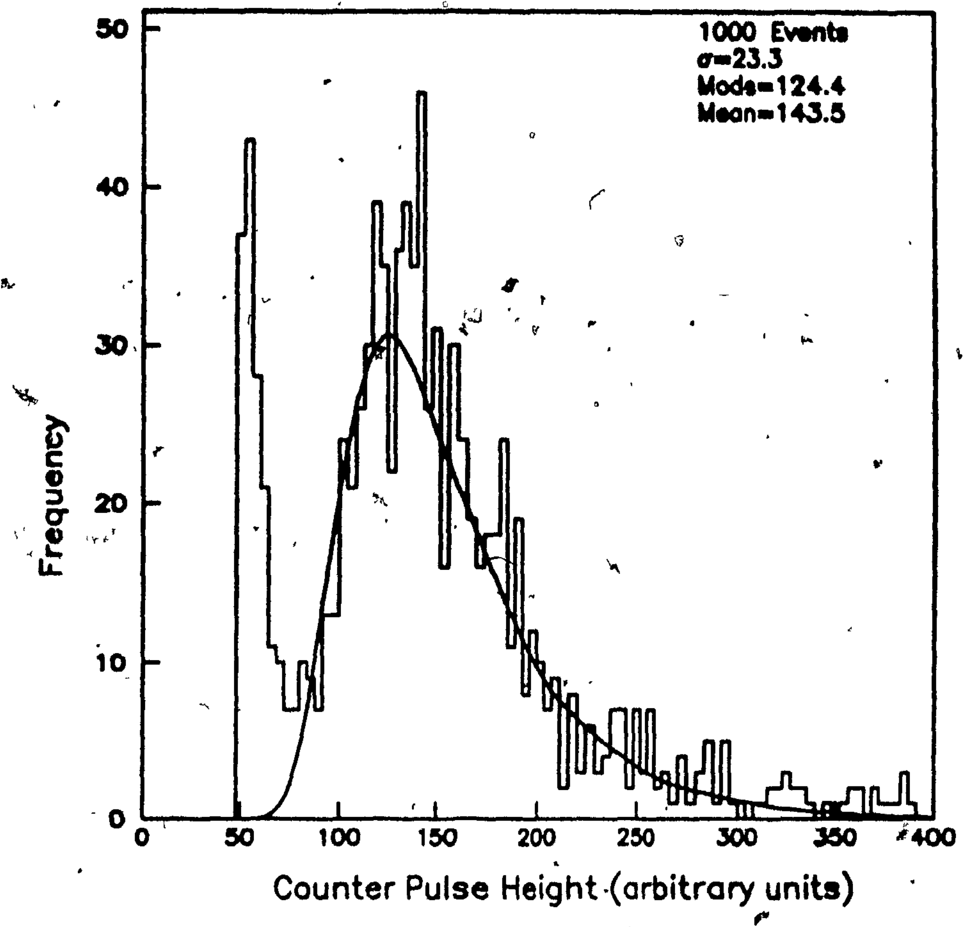

FIG 3.12: Raw pulse height spectrum obtained from counter 11 showing distinctly the presence of a noise peak around 60 ADC counts.

events with a typical trigger requirement that $\geq$5 counters fire in a shower for it to be accepted. It takes 40 hours for a disk to be filled. The event rate is ~4 showers per minute. The data is not, however, accumulated on floppy disks. It is collected at roughly 24 hour intervals via a phone link between the LSI 11 and the VAX 785 in the Physics department. Once a file is ready to be transfrerred, it is flagged so that is can be overwritten whenever space is required on the disk. No dead time is introduced in the process of data collection since the transfer program runs in the background mode. The process of data transfer takes approximately 8 minutes per file and presently requires operator initiation. Since data is collected each day without fail, the floppy disk never gets full and data is collected constantly.

4. DATA ANALYSIS

General

The shower data that is accumulated over a period of time is divided into blocks. Each block of data has a set of 19 single particle spectra corresponding to the nineteen counters in the array. As mentioned in Chapter 2, the number of particles that traverse a counter is obtained by dividing the ADC pulse height data by the mean of the single particle spectrum for that counter. Figure 4.1 shows a plot of the single particle means for counter 1 over a period of 60 days. It is clear that this quantity does vary somewhat over time. Ideally, single particle line (henceforth SPL) data for each counter should be taken each day or even more frequently if possible. Unfortunately, due to funding restrictions the additional electronics required to automate the process of SPL data collection could not be installed and hence this part of the experiment requires operator intervention. Owing to the the distance between the Physics department and the experiment location, a field trip every day is not possible. So at present, SPL data are collected once a week and the means of the spectra are stored in a file that can be accessed when shower data corresponding to that week are being analysed. At the time of writing this part of the thesis, shower data has been collected almost continuously for 5 months and analysed to determine the shower size and the core position of each accepted shower. See figure 4.2. The computation of the shower parameters i.e, its size and core location is performed by applying the technique of Likelihood Maximization to accumulated data. In the two sections that follow, the basic principle of the technique and its application for our case is described in detail.

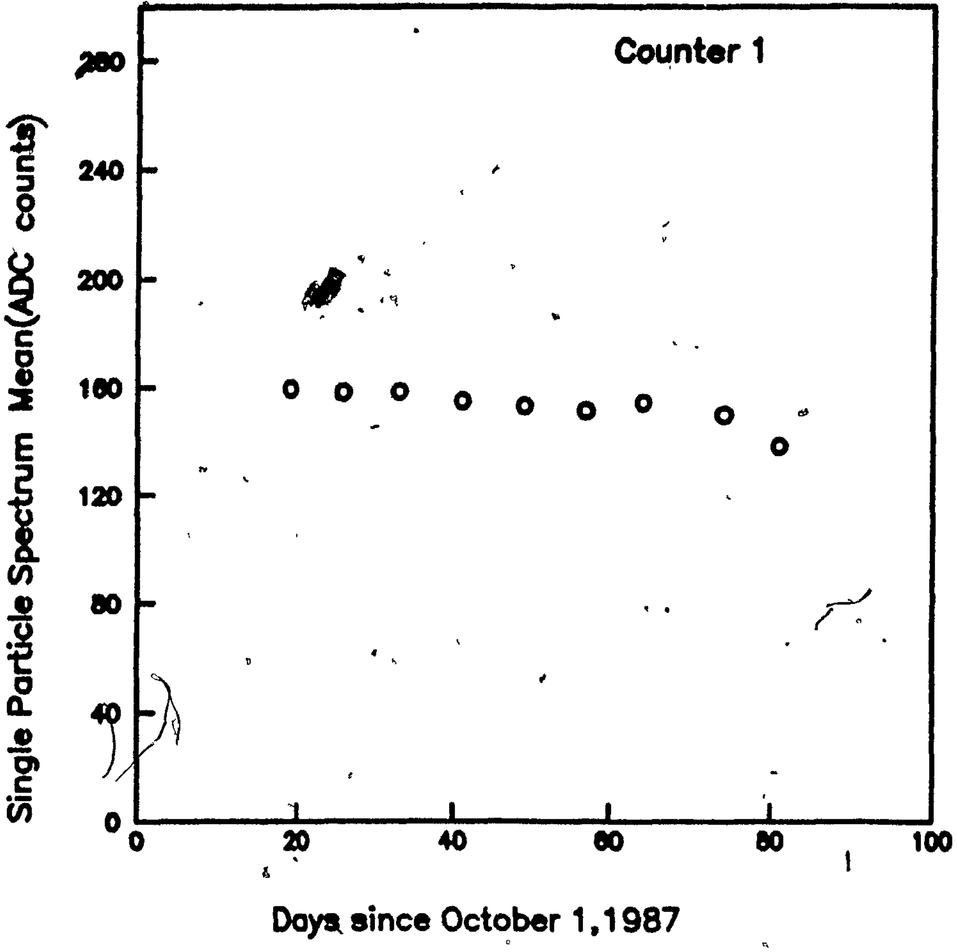

FIG 4.1: A plot of the means of the single particle spectra obtained for counter 1 over a period 60 days.

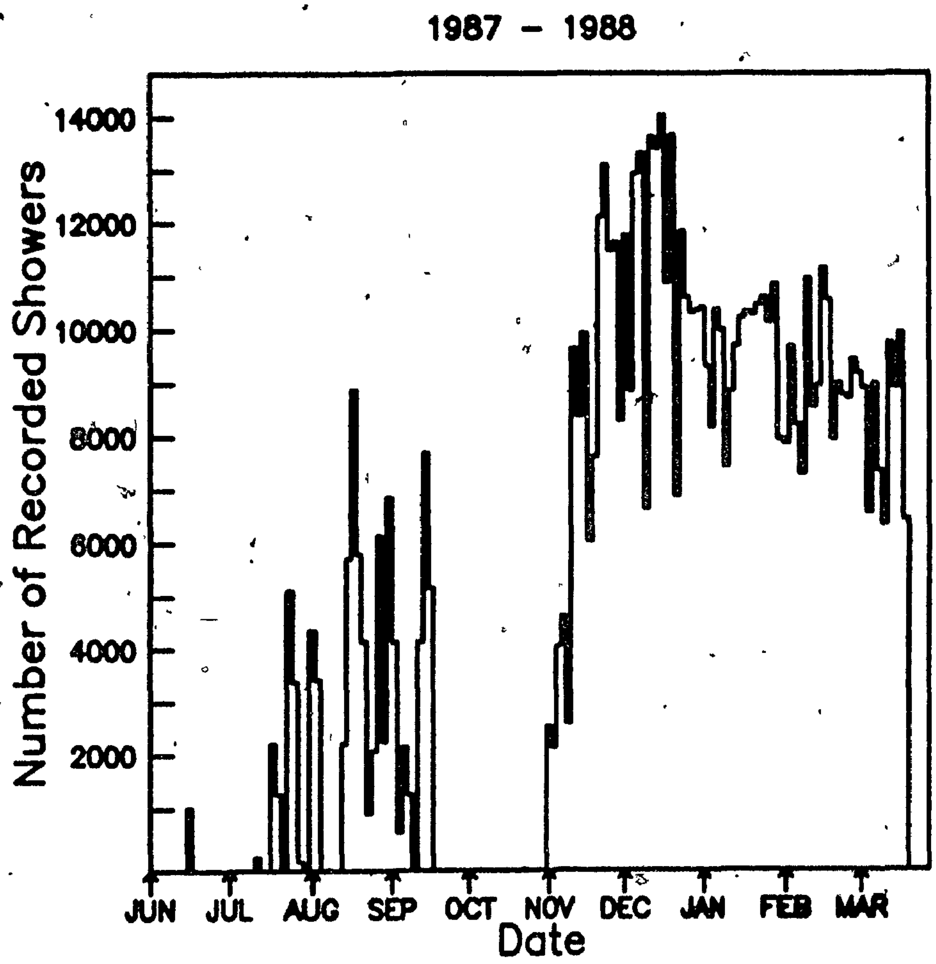

FIG 4.2: A histogram of the total number of showers recorded by the data collecting system since June 1987. The binwidth is 2 days.

Section 4(a): The Maximum Likelihood Method

For the purpose of parameter fitting, the maximum likelihood (ML) method is considered the most powerful tool. This is specially true for parameter fitting of cosmic ray shower data where other techniques like χ^2-minimization have failed repeatedly to give reasonable results. A more detailed comparison of the two fitting techniques will be given later in this chapter.

Consider the distribution function y which is a function of two parameters a and b. Suppose again that we have some experimental data on the distribution consisting of a set of values x_i for each event that is observed. So,

$$y_i = f(a, b; x_i) \tag{1}$$

Assuming that the distribution function y is a reasonably good one for our experiment, we seek to find out the answers to two questions: (*i*) What values of the parameters a and b provide the best description of the data set used? (*ii*) To what limits of accuracy can a and b be determined? To arrive upon the answers to these questions, in the likelihood method the distribution function is rewritten as:

$$y = N_1 \; f(a, b; x) \tag{2}$$

where N_1 is the normalization factor such that:

$$\int_{x_l}^{x_h} y \, dx = 1$$

where, x_l and x_h are the low and high limits on x. In short, the function y is normalized so that the function (2) behaves as a probability distribution. For the i^{th} event, the probability density for observing the event is given by:

$$y_i = N_1 \; f(a, b; x_i)$$

which is a function of the parameters. The likelihood function is defined as the product of the y_i for all the n events in our sample. i.e.,

$$\mathcal{L}(a, b) = \prod_{i=1}^{n} y_i$$

So, $\mathcal{L}$ is the joint probability density for obtaining the observed set of values of x_i for any specific value of a and b. Thus,to obtain the best values of the parameters, the likelihood function is maximized. The normalization factor is very important because it ensures that the likelihood function has an absolute maximum, since y_i can no longer be indefinitely increased by making the parameters larger. In many cases, the logarithm of the likelihood function is a more convenient function to maximize;

$$l = log\,\mathcal{L}$$

$$l = \sum_{i=1}^{n} log\, y_i.$$

It is also common to *minimize* the negative of the logarithm of the likelihood function. The best values of the parameters then are those that minimize $-l$. The errors on the parameters are determined by several methods. The most direct method is to perform a Monte Carlo of the events and directly use the sigmas of the distributions of fit parameters minus the thrown parameters provided the experiment is capable of being reproduced well using Monte Carlo simulations. A second technique is to keep all but one of the parameters fixed (thus reducing it to a one parameter estimate problem) and then to determine the change in that parameter required to reduce l from its value at the maximum by .5,

$$l(a_0 + \delta a) = l(a_0) - \frac{1}{2}$$

If the distribution of $\mathcal{L}$ in that parameter is not Gaussian, two values a_1 and a_2 are obtained such that

$$l(a_i) = l(a_0) - \frac{1}{2}, \qquad i = 1, 2$$

then, in the range $a_1 < a < a_2$, the true value of a has 68% probability of being within the range. This is the 'one standard deviation confidence interval' of the likelihood function.

The χ^2-Minimiztion Method Compared to the Likelihood Method

Taking the same distribution function (1) in the form of a histogram, and denoting by y_i^{obs} the entry in the i^{th} bin of the histogram, the χ^2-minimization tries to fit the data by constructing and minimizing

$$\chi^2(a_j) = \sum_{i=1}^{nbins} \frac{[y_i^{obs} - y_i^{th}(a_j)]^2}{\sigma_i^2}$$

where the a_j are the j parameters in the theoretical expression and σ_i are the assumed errors of y_i^{obs}.

The greatest advantage of the ML method is immediately apparent — the input data are individual events and so there is no need to first construct a histogram. So, in cases where the event density is too low(as is the case in our experiment) to make a histogram, the likelihood method is superior to χ^2-minimization method. Again, if the χ^2-surface is not regular in the parameters, the surface can have several minima and the minimization can converge at a secondary minima instead of converging at the global minimum. The ML method does not search any surface for the maximum and so this problem does not apply.

Since the ML method absolutely requires the function to be normalized, this could present difficulties in case of complicated functions involving many parameters. Both the ML and the χ^2 methods are based on the basic *assumption* that the function used gives a satisfactory description of the data observed. In our case this is not a problem because the function used has been tried and tested for a long time. The application of the χ^2 method for parameter fitting of shower data has been studied by several groups[28, 29] without much success in the limits of a small number of detected particles, the χ^2 surface is not a smooth function of the core location and so it can have several local minima. So, unless elaborate precautions are taken to ensure that all local minima are rejected and convergence occurs only at the global minima, more often than not the minimization terminates at the local minimum yielding unreliable results. This problem would disappear when the number of detected particles is high but at this point, the method would not be of much use to us since, as will be seen later, our statistics on showers of very large size is quite low.

Section 4(b): Maximum Likelihood Technique Applied to Shower Data[30]

In this case, the density of shower particles is assumed to have a lateral distribution along the plane of the shower front given by the NKG function:

$$\rho = \frac{N}{2\pi} \frac{exp[\frac{-r}{r_0}]}{r_0(r+1)} = N \times f,$$

where, N is the number of particles in the shower and r is the distance between the shower axis and the counter in the plane of observation. So, a shower of size N upon incidence at a point (X,Y) would deposit m_i particles in a counter situated at (x_i, y_i) and this is given by,

$$m_i = N f_i \qquad i = 1...19$$

and,

$$r_i = \sqrt{(X - x_i)^2 + (Y - y_i)^2 - \{l(X - x_i) + m(Y - y_i)\}^2}$$

where, l and m are the direction cosines of the shower axis in the X and Y directions respectively.

Defining

(i) P(E/S) as the probability that an event (a shower) of the type S characterized by the parameters N,X,Y would give rise to an event of type E characterized by $\{n_i\}$. n_i is the actual number of particles observed in counter i when the expected number was m_i. This probability is given by

$$\left[\frac{exp(-m_i)\, m_i^{n_i}}{n_i!}\right];$$

(ii) P(S/E) as the posterior probability i.e., the probability that an event of type E was caused by a shower of type S;

(iii) P(S) as the *a priori* probability of occurrence of of a shower of type S (taken equal to $N^{-2.5}$);

(iv) P(E) as the *a priori* probability of the occurrence of an event of type E. This quantity is not a function of the array characteristics, it is taken as a constant and ignored in the calculations;

the probability density function corresponding to y of Section (a) that is maximized is given by:

$$P(S/E)=P(E/S)\ P(S)/P(E)$$

Substituting,

$$P(S/E) = \left[\frac{exp(-m_i)\, m_i^{n_i}}{n_i!}\right] N^{-2.5}$$

The best values of X, Y, N, are obtained by **minimizing the negative logarithm of the posterior probability :**

$$F(X,Y,N) = \sum_i -log_e\left[\frac{exp(-m_i)\, m_i^{n_i}}{n_i!}\right] + 2.5 log_e N \qquad (3).$$

Substituting $m_i = N f_i$,

$$F(X,Y,N) = N\sum_i f_i - \sum_i n_i\, log\, f_i - \left(\sum_i n_i - 2.5\right) log\, N - \sum_i log\, n_i! \qquad (4)$$

For fixed (X,Y), the value of N that leads to a minimum for the function is given by:

$$N_0 = \frac{\left[(\sum_i n_i) - 2.5\right]}{\sum_i f_i} \qquad (5)$$

Using the above formulae, the parameters are obtained by using the popular grid search method[18]. The parameter search is started at the 'centre of mass' of the hits which is determined simply calculating :

$$x_{cm} = \frac{\sum_i x_i n_i}{\sum n_i} \quad , \quad y_{cm} = \frac{\sum_i y_i n_i}{\sum n_i}$$

A 3×3 grid is then constructed with its centre at (x_{cm}, y_{cm}). At each of the nine points on the grid, N_0 is calculated and used in equation (4) to compute F(X,Y,N).

If the smallest value of F(X,Y,N) does not occur at the centre of the grid, a new one is constructed with its centre positioned at the site of the minimum of the function. The procedure is repeated until a point is reached when the position of the function minimum and the grid centre coincide. A smaller grid is constructed with the same centre and the procedure is repeated. The shrinking of the grid is stopped when the grid size reaches the detector dimensions since no further increase in accuracy can be achieved. An estimate of the quality of the fit is obtained by computing the quantity χ^2 /degrees of freedom(DOF) given by:

$$\chi^2/DOF = \frac{\left[\sum_i (n_i - m_i)^2/n_i\right]}{(s-3)}$$

where, s is the number of counters that participated in the event. The quantity χ^2/DOF has an expectation value of 1.

Section 4(c): Monte Carlo of Fitting Routine

To test the reliability of the fitting technique, a series of Monte Carlo calculations was performed and the known input parameters were compared with the parameters obtained from the fit. As before, showers were generated uniformly in $cos\theta$ and ϕ over a radius of 100m from the centre of the array. Knowing X, Y and N for each shower generated, the number of particles that each counter in the array would detect was calculated using the NKG function. This number was Poisson smeared to take statistical fluctuations into account and realistic trigger conditions were chosen to filter data. A shower that passed the trigger cuts was subjected to the fitting procedure described above, taking the centre of mass of the shower as the starting point for the grid search. The grid size was chosen as 20m and it was shrunk by half four times when the grid size equalled 1.25m (recall that the detector area is 1m^2). The trigger conditions were chosen to show bias towards showers that fall near the centre of the array for the following reason. Since the starting point for parameter fitting is the centre of mass of the shower, with a shower falling near the centre of the array this position can be determined with considerable accuracy. However, with a shower that falls towards the edge of the array this estimate would not be as accurate since there would not be any input from the points outside the array that nevertheless received majority of particles in the shower. The result would be a false centre of mass and consequently the parameters determined would not have a high degree of accuracy.

To understand the effect of the trigger conditions for the LEDA array, a plot was made of the trigger efficiency of the array as a function of the shower size for vertical showers. Trigger efficiency is just the ratio of the number of showers generated to the number of showers that pass the trigger conditions imposed. Efficiency plots obtained for three trigger conditions are shown in Figure 4.3. To be able to fit a plane to the shower front to find out the direction of arrival of the shower, a minimum of three counters must participate in the shower. Data is biased towards the centre of the array by requiring that at least one inner counter receive at least N_{C1} particles before a shower is accepted. In figure 4.3, the numbers (2-1-3,etc) indicate the trigger conditions used on the Monte Carlo data. The first number indicates the minimum number of particles that at least one of the inner counters must receive. The minimum number of particles N_{C2} that at least N_T counters in the array must receive are indicated by the second and the third numbers. The trigger condition finally chosen required $N_{C1}=4$, $N_{C2}=1$ and $N_T=5$ since with this condition, the trigger efficiency for showers of size

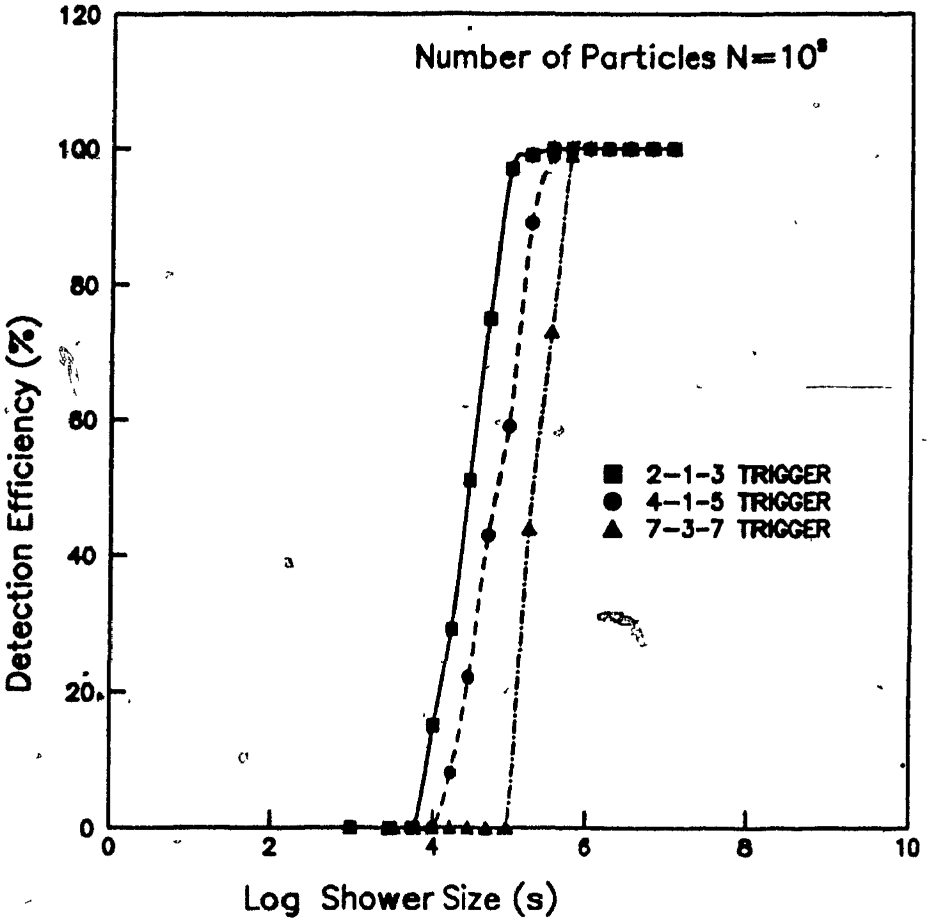

FIG 4.3: Results of the Monte Carlo study of the trigger efficiency of the LEDA array for showers of different energies and trigger conditions. The numbers 2-1-3, etc., represent the minimum number of particles in one of the inner seven counters, the minimum number of particles required in a minimum number of counters in the array respectively.

4.25 is approximately 50%. A looser trigger condition would result in unacceptable dead time whereas a tighter trigger condition decreases the efficiency for smaller sizes and hence raises the energy threshold of the shower. Further cuts are applied to the data during parameter fitting to eliminate 'bad' events. A shower is rejected if its centre is greater than a certain distance from the array centre for reasons already discussed. An additional cut is imposed on the χ^2/DOF of the fits as well as on the total number of particles that must be detected. This last cut is necessary to speed up the program by rejecting events that would not result in fitted showers with size above the threshold of 4.25. A final cut on fitted showers requires the shower core to be at a distance not more than 50m from the array centre. The reasons for application of such multi-step cuts are discussed under 'Fitting efficiency' in this chapter.

The results obtained from the fitting program are shown in Figures 4.4 to 4.11(a value of r_o equal to 75m was used in the calculations). Figure 4.4 is a plot of the radial distribution function used for fitting the parameters. For selected showers, the quality of the fits can be viewed in the form shown in Figure 4.5(a) and (b). In 4.5(a), the array layout is depicted as the set of 19 small circles. The radius of the larger superimposed circle is a function of the number of particles received by that counter. The dashed concentric circles are contours of constant number of particles decreasing outward with the centre located at the position of the shower core. Figure 4.5(b) shows the theoretical curve fitted to the data. Figure 4.6 is a plot of the difference between the thrown point of incidence of the shower in the X-Y plane and the point of incidence as calculated by the fitting program. Ideally, this should be zero. In our case, with a radial cut of 75 metres, the difference rarely exceeds 10 metres. The resolution of the array was studied by comparing the known thrown parameters with the parameters returned by the fitter. The results are shown in Figures 4.7 to 4.11. The array resolution improves at high energies. This could be because at high energies, more counters are populated with higher number of particles and the resulting statistics result in a better estimate of the shower centre of mass. In X and Y, the array resolution is of the order of 7m at low energies and 3m at high energies. In shower size determination, the error ranges from a factor of .3 at the low end to a factor of .05 at the high end. Figures 4.7(a) to 4.11(a) are the results of the Monte Carlo simulation of 500 showers of size 5.8(630957 particles). Figure 4.11 is a histogram of *uncut* χ^2/DOF for the fits and it has an expectation value around one.

Fitting efficiency plots

The number density spectrum obtained as a result of the analysis of actual shower data has to be corrected for the fitting efficiency to obtain the real number spectrum. A shower that passes trigger cuts need not necessarily be passed by the fitting routine. Figure 4.12 is a plot of the trigger efficiency of the array for the actual 4-1-5 trigger that is applied on the shower data along with the fitting efficiency plot. The fitting efficiency plot shows the percentage of showers that upon passing the trigger cuts, also pass the fitting routine cuts. The cuts that are imposed in the parameter fitting part of the program require *(i)* the χ^2/DOF of the fits to be less than 3; *(ii)* the fitted shower to lie within 50 metres of the array centre.

The first constraint rejects 'bad' fits. The final constraint rejects events that pass the first two cuts but are bad fits nonetheless. Referring back to figures 4.7 to 4.11, it is clear that as the distance from the array centre increases, so do the errors in parameter

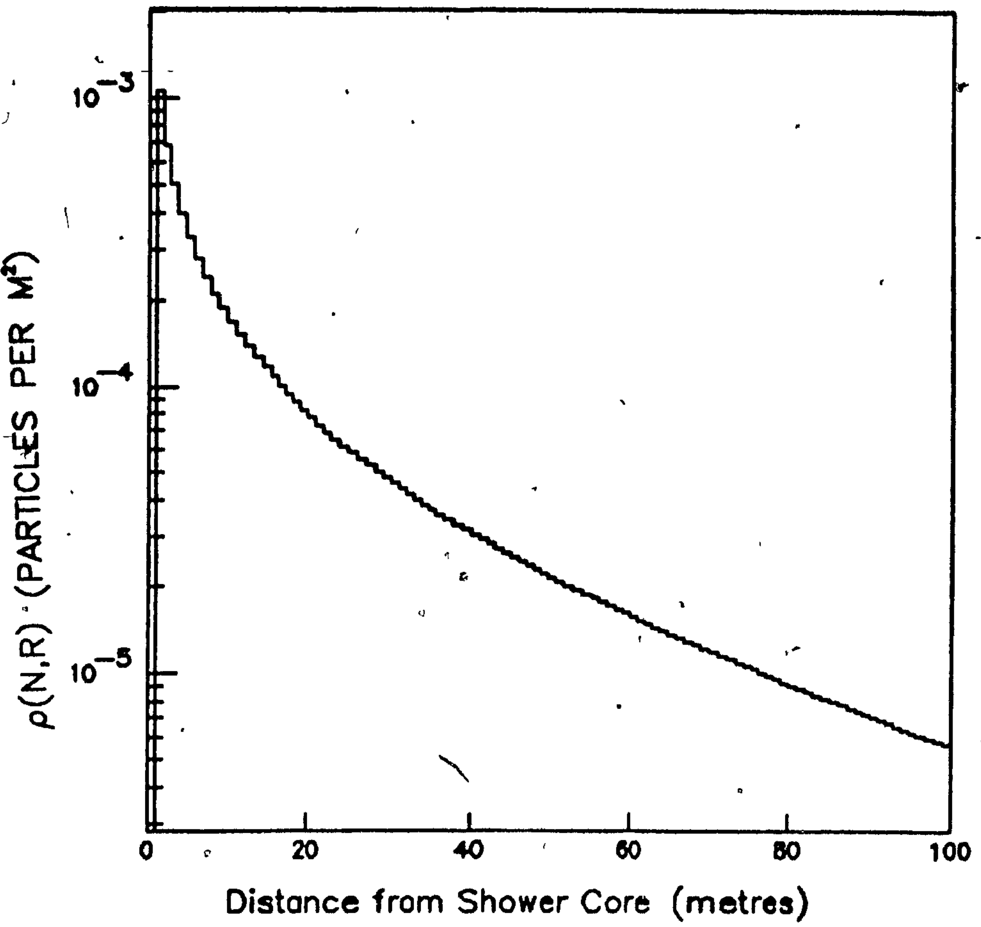

FIG 4.4: The radial distribution function *f* of section 4(b) is plotted as a function of the distance from the shower core

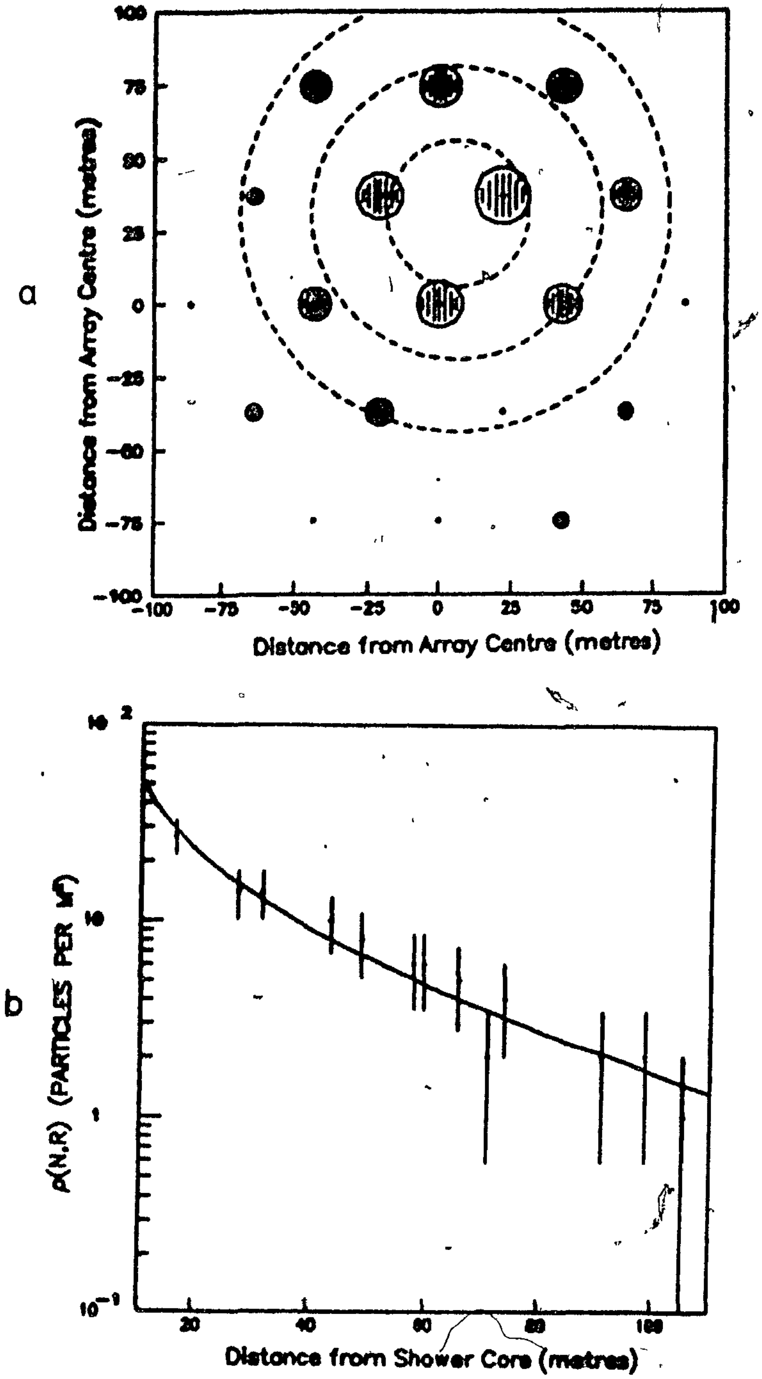

FIG 4.5: (a) An estimate of the quality of the fit is obtained by potting the array layout and superimposing counter positions with circles that have their radii proportional to the number of particles received by that counter as calculated by the fitted parameters of the distribution function. The dotted circles have as their common radii the calculated core of the shower. (b) The distribution function ρ of section 4(b) is plotted as a function of the distance from the shower core. The superimposed points are the number of particles actually populating the detectors. The shower size used is 5.5.

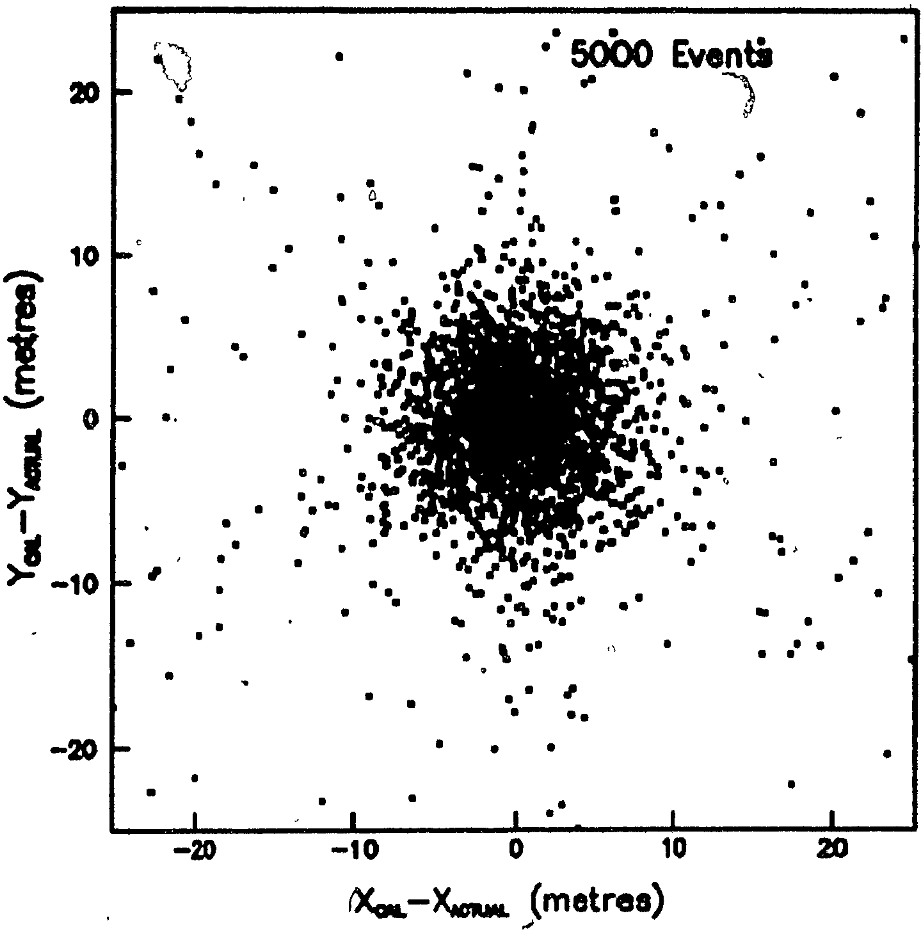

FIG 4.6: The difference between the thrown X and Y coordinates of the shower core and the X and Y of the calculated shower core.

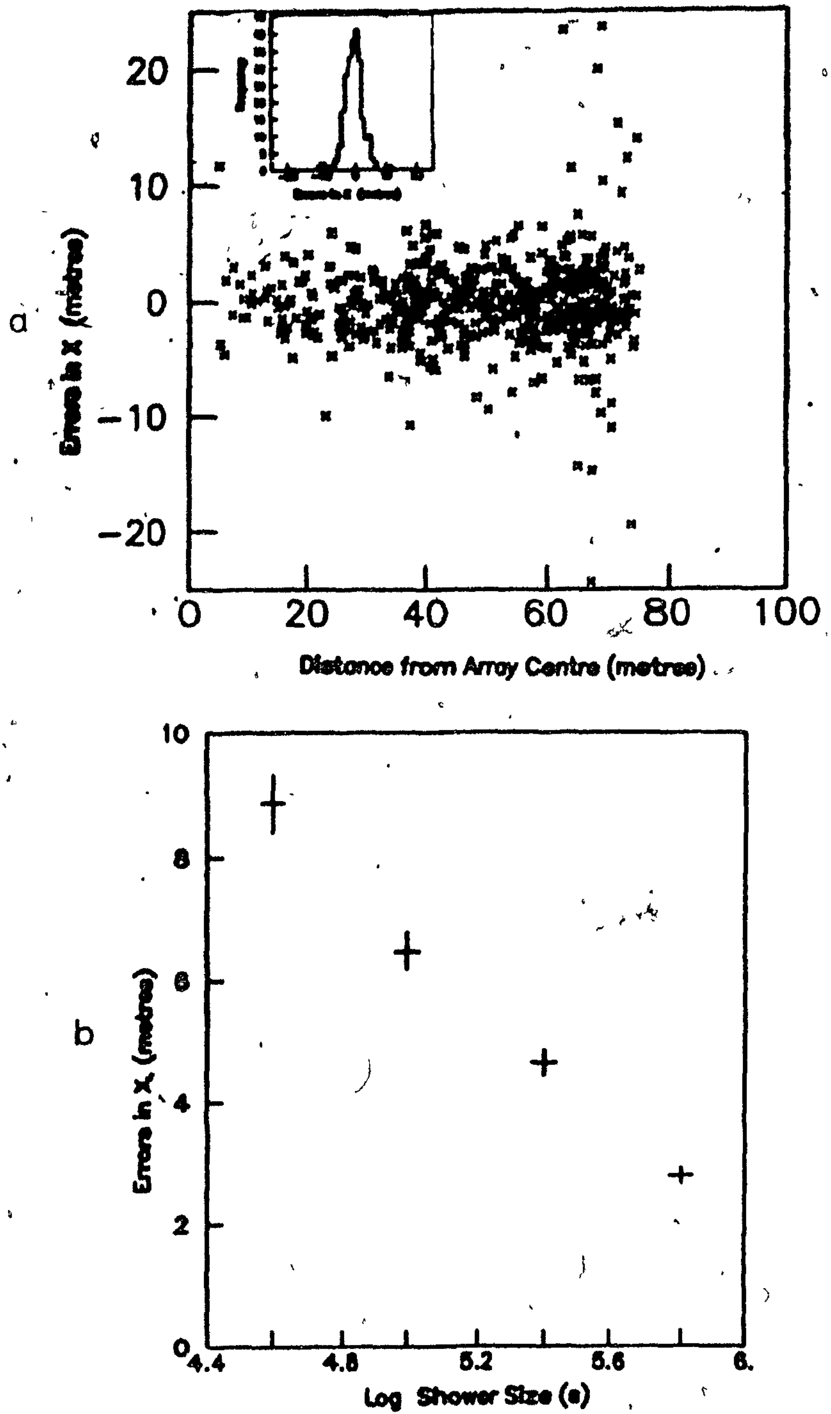

FIG 4.7: (a) Monte Carlo calculation of the error in the X coordinate of the shower core as a function of the distance of the core from the array centre. The inset is a y-projection of the scatter plot. (b) The mean error in X is plotted as a function of the shower size.

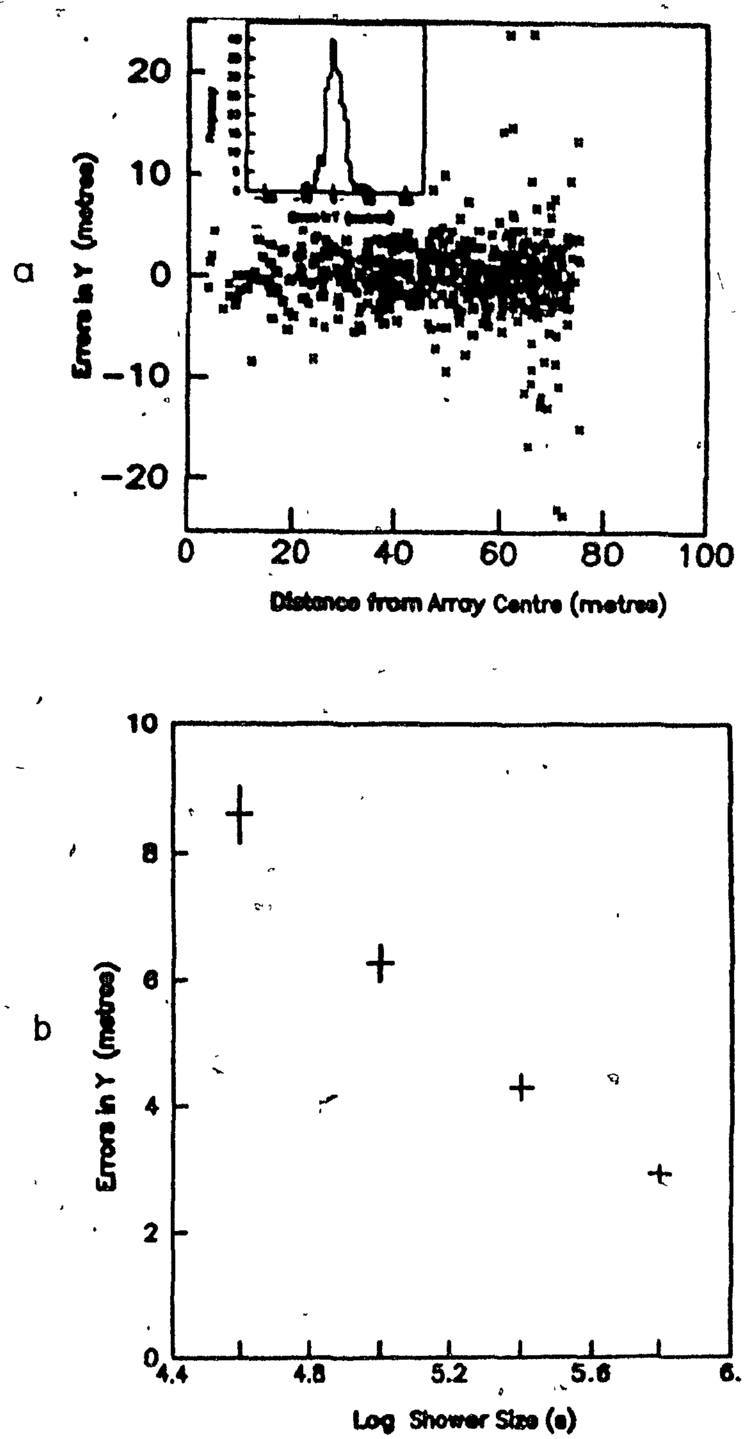

FIG 4.8: (a) Monte Carlo calculation of the error in the Y coordinate as a function of the distance of the shower core from the array centre. The inset is a y-projection of the scatter plot. (b) The mean error in Y is plotted as a function of the shower size.

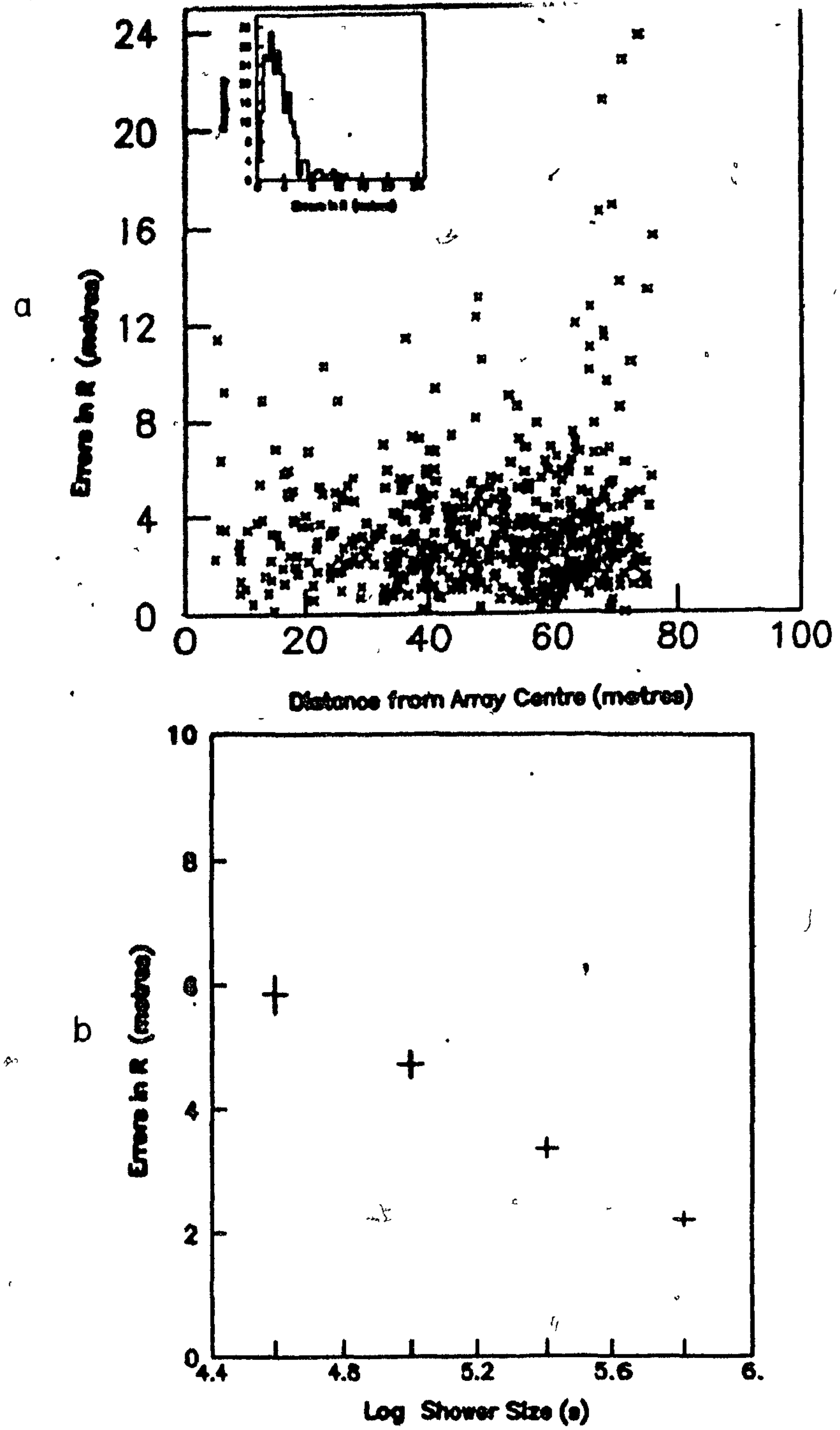

FIG 4.9: (a) Monte Carlo calculation of the difference between the actual and the calculated distance between the position of the shower core and the array centre as a function of the distance between the calculated core and the array centre. The inset is a y-projection of the scatter plot.(b) The mean error in R plotted as a function of the shower size.

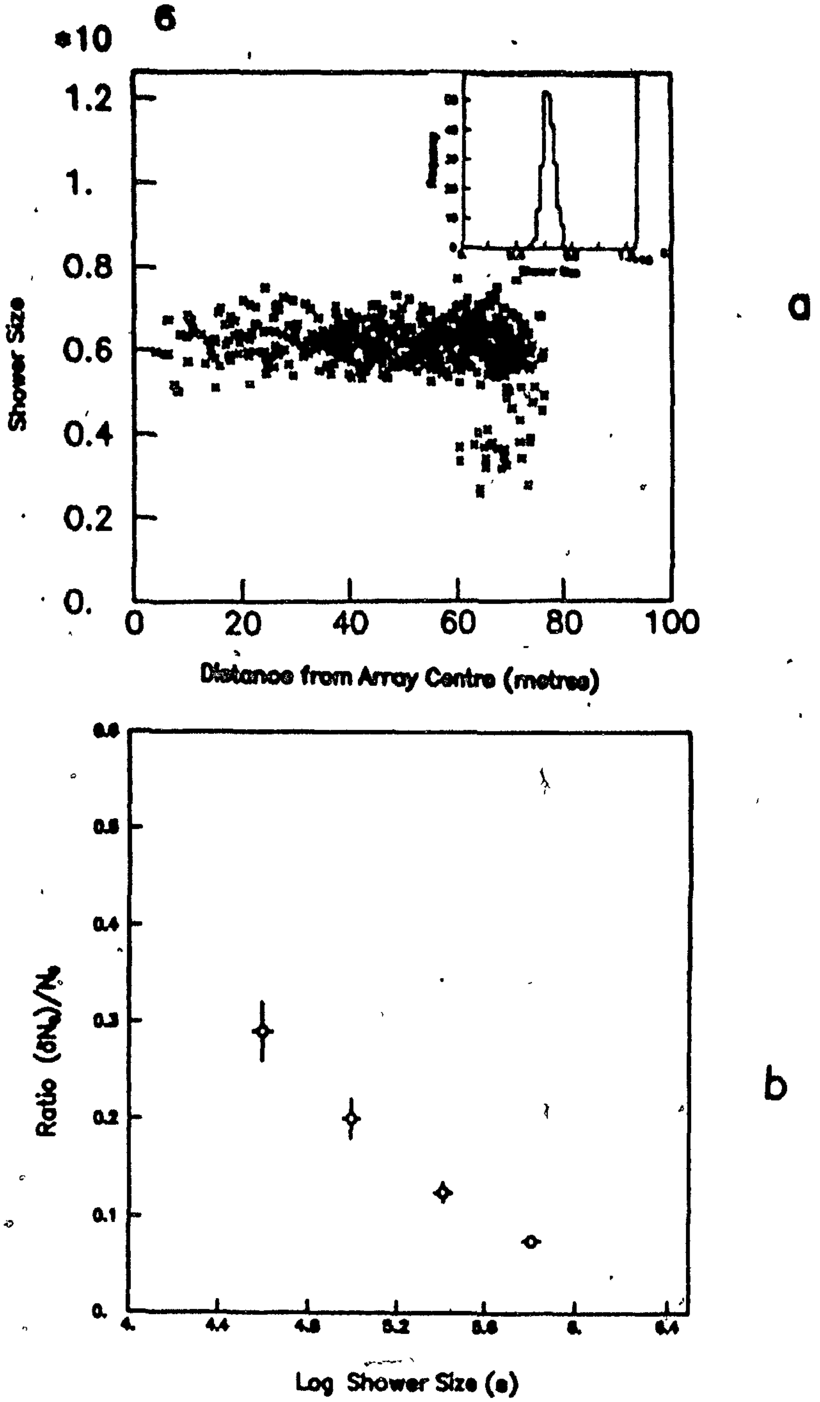

FIG 4.10: (a) The the number of particles in the thrown shower is plotted as a function of the distance of the shower core from the array centre. The inset is again a y-projection.(b) The mean error in the calculation of the shower size is plotted as a function of four different shower sizes.

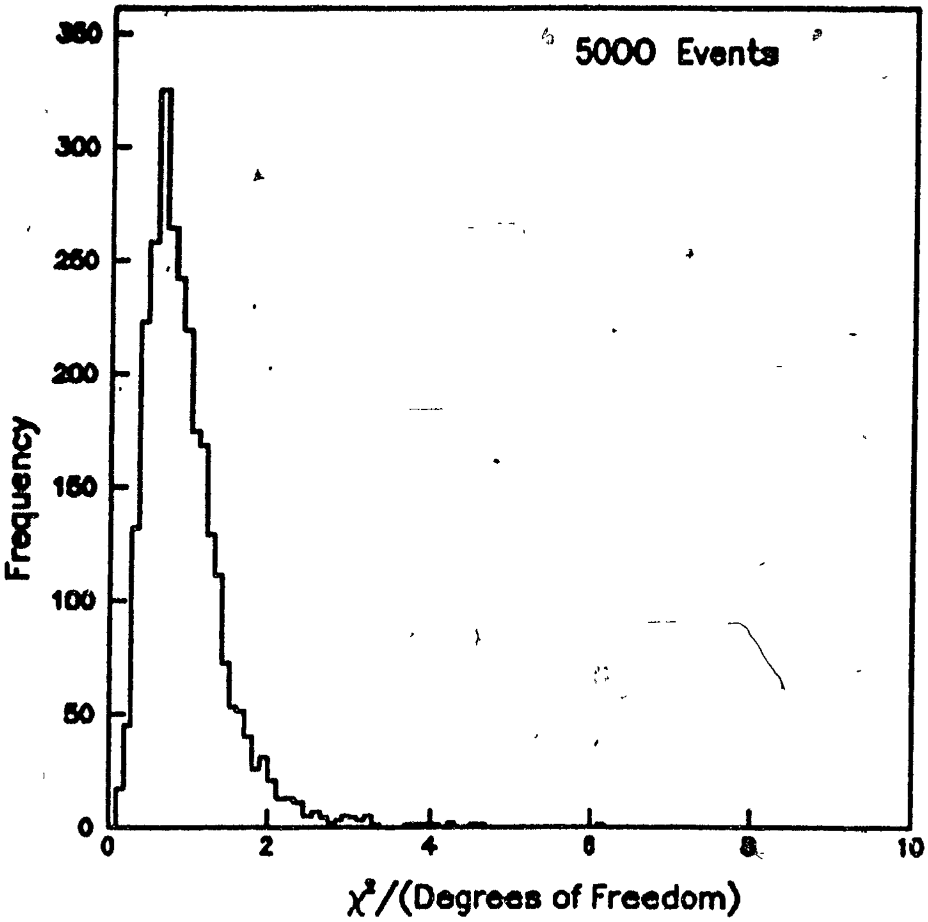

FIG 4.11: Histogam of the raw χ^2/degrees of freedom for the fits obtained from Monte Carlo calculations.

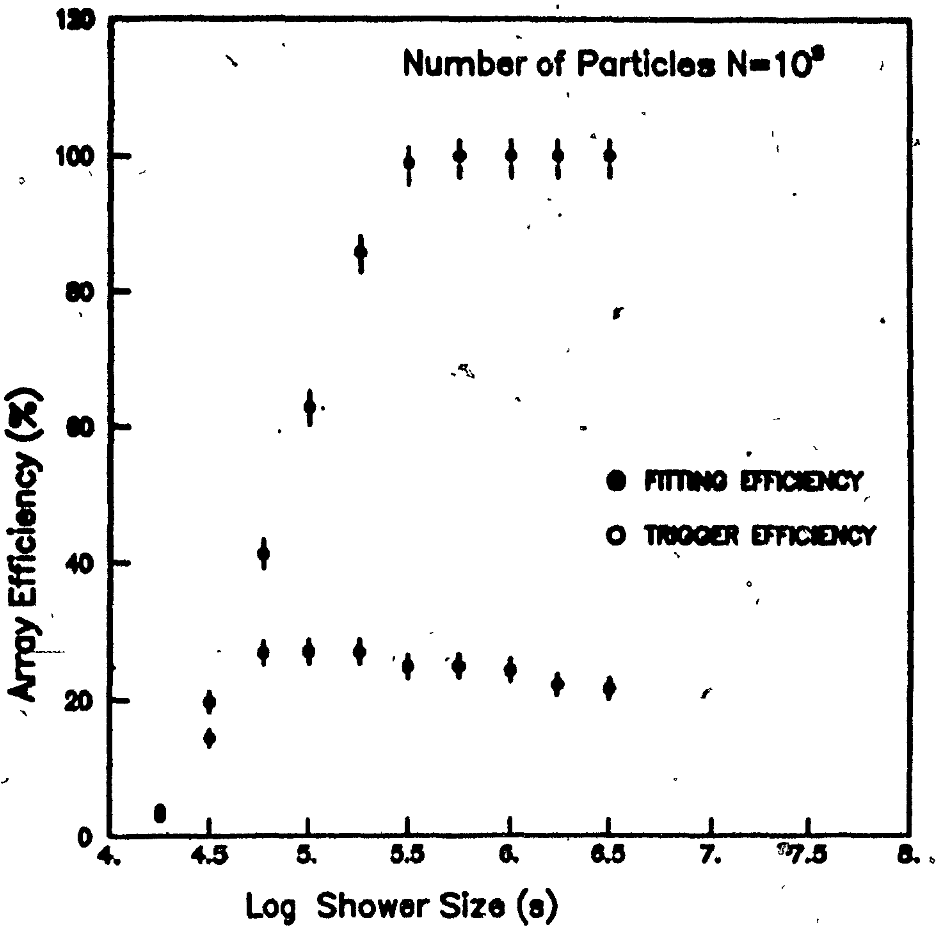

FIG 4.12: Monte Carlo estimation of the fitting efficiency of the LEDA array for different shower sizes. Also shown for comparison is the trigger efficiency of the array for trigger cuts 4-1-5. The fitting cuts are described in the text.

estimation. Beyond a radius of 50m from the array centre, there is an abundance of badly fitted events.

Because showers are thrown out to R=100m but the analysis requires R<50m to ensure good fits the maximum fitting efficiency is only 25%. For purposes of flux measurements we can say that the array is essentially 100% efficient over an area of radius 50m for shower size >4.75. It is worth remembering that there is no correction made for the triggering deadtime.

Section 4(d): Analysis of shower data

Having decided upon the trigger and the fitting cuts that are required for parameter fitting for the array, the cuts were incorporated into the program that decodes real shower data for analysis. As mentioned at the beginning of this chapter, shower data are divided into blocks with a set of nineteen single particle means corresponding to each. This ensures that the conversion from ADC counts to number of particles is consistent over time. The data presented in this thesis represents 6 such blocks spanning a period of 60 days with a total of 400,000 raw showers(showers that passed the hardware trigger).

The ADC data are converted to particle data by dividing by the SPL means; the TDC data are converted to distances by multiplying by the velocity of light and this data is used to fit a plane $ct = ax + by + c'$ where c is the velocity of light and a, b and c' are constants of the plane, to obtain the direction coordinates of the shower axis. Showers with θ greater than 30° are rejected. To get rid of the ϕ dependence of the shower, the array is rotated by ϕ about the z-axis. The data set is then subjected to the trigger cuts and the shower parameters estimated exactly as described in the previous section.

The outputs that correspond to figures 4.5(a) and (b) are shown in figures 4.13(a) and (b). Figure 4.14 is a plot of the χ^2/DOF for the fits. Figure 4.15 is a plot of the position of the shower cores in the X-Y plane obtained from the fits. Finally, figure 4.16 is the histogram of the raw size spectrum representing the number of showers that had size between N and N+dN.

To obtain an estimate of the errors in the three fit parameters, the method described in Section 4(a) is applied. The error in N is obtained by keeping X and Y of the shower fixed and estimating the change δN in N required to cause a change in F(X_0,Y_0,N) by .5 (see in equation (4)). The error in X and Y are obtained similarly. Figures 4.17(a), (b) and (c) show the error estimates obtained for the three parameters for real data as well as Monte Carlo. The errors obtained for real data are remarkably consistent with the errors obtained from Monte Carlo. The one standard deviation confidence interval for X ranges from ±6 at low energies to ±3m at high energies. The corresponding errors in Y range from ±5 to ±3. This is because the detectors in the array are placed closer in y than in x. The shower size can be determined to within factor that ranges from .3 to .07.

Section 4(e): Differential Size and Energy Spectra

The efficiency of the array influences the shower size spectrum obtained from raw data. Since Monte Carlo of the shower data shows that the array efficiency is low for showers of size lower than 4.75, the number of showers in that range that are detected are a factor of 1/efficiency lower than the number that would have been detected if the

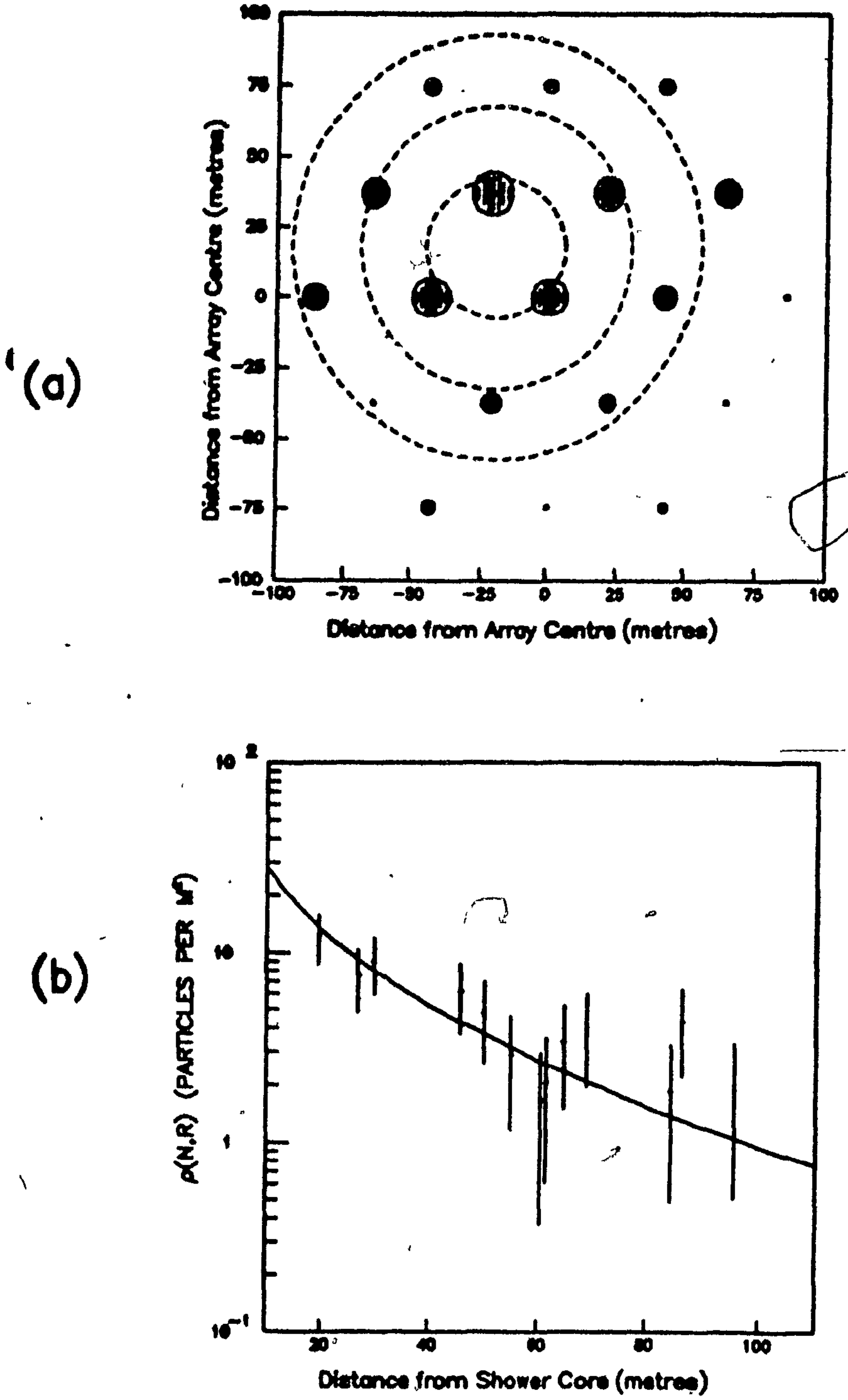

FIG 4.13: Plots similar to figure 4.4(a) and (b) obtained from the analysis of real data.

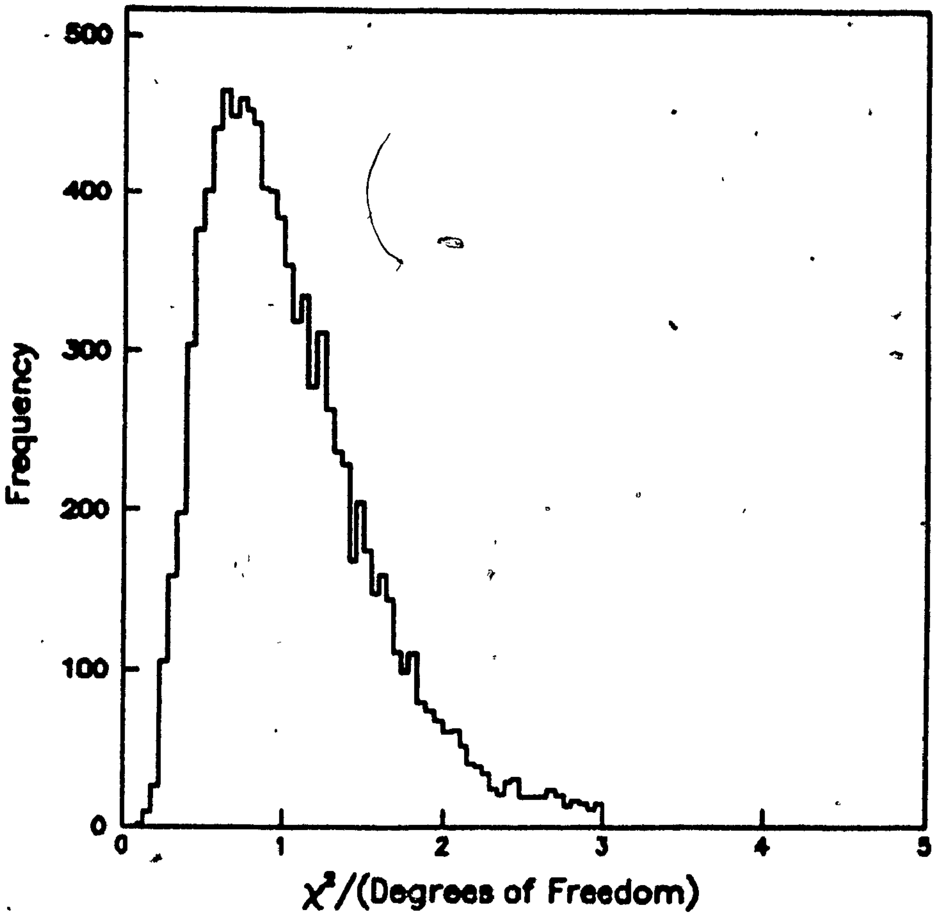

FIG 4.14: A histogram of the χ^2/degrees of freedom for the fits calculated for real shower data. The cut on the data requires the χ^2/DOF to be less than 3.0

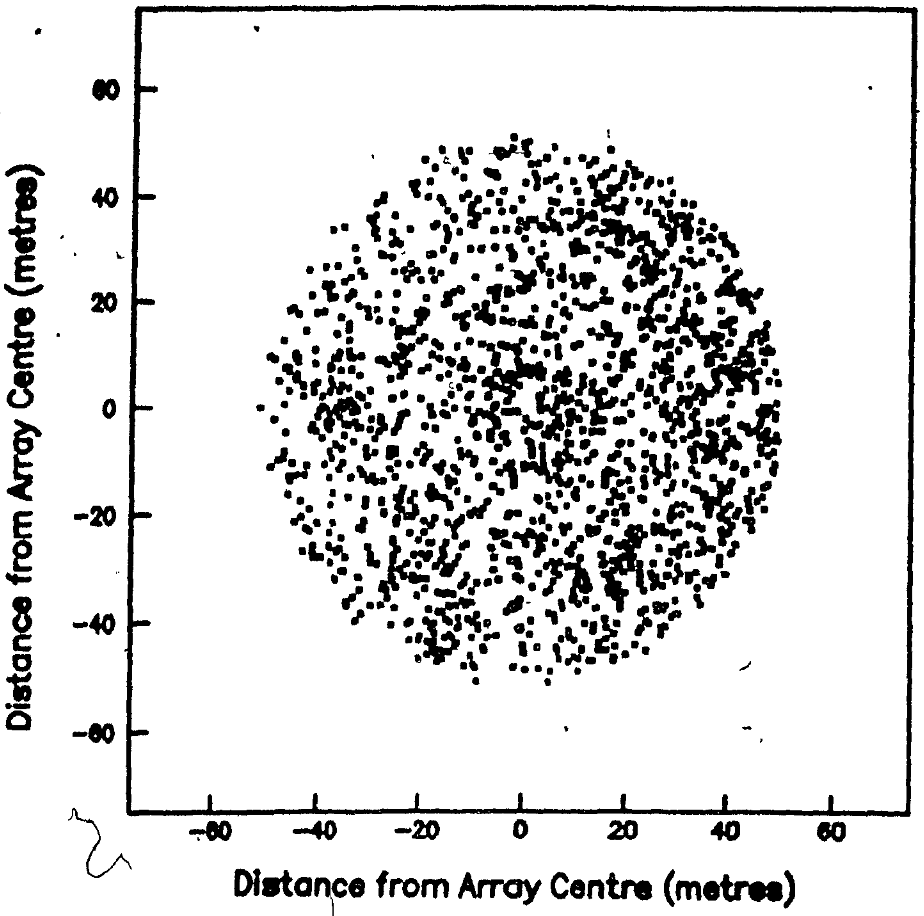

FIG 4.15: Shower core positions as obtained from analysis of real data.

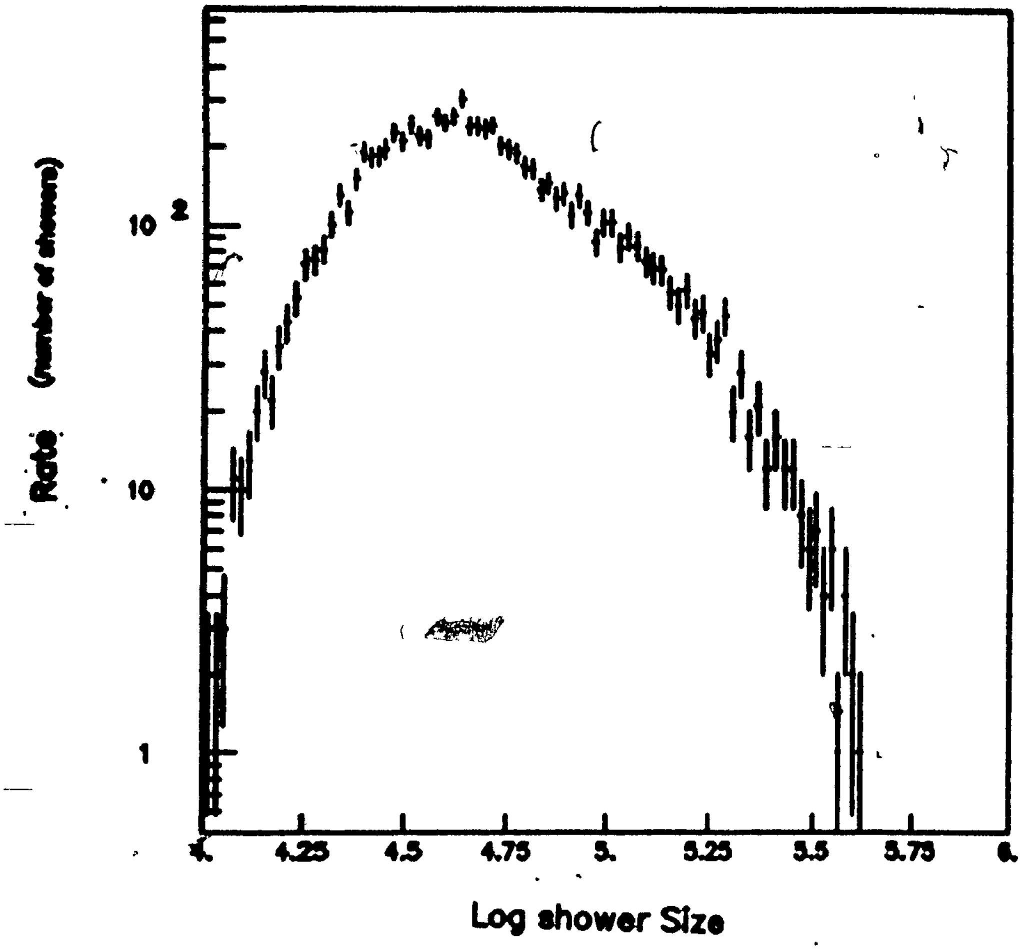

FIG 4.16: Histogram of the raw shower size spectrum obtained from the analysis of 400,000 recorded showers. The ordinate axis represents the number of showers that were calculated as having their sizes between log N and log N+dlog N. The bin size along the x-axis is ,02. Units of rate are total number of showers observed.

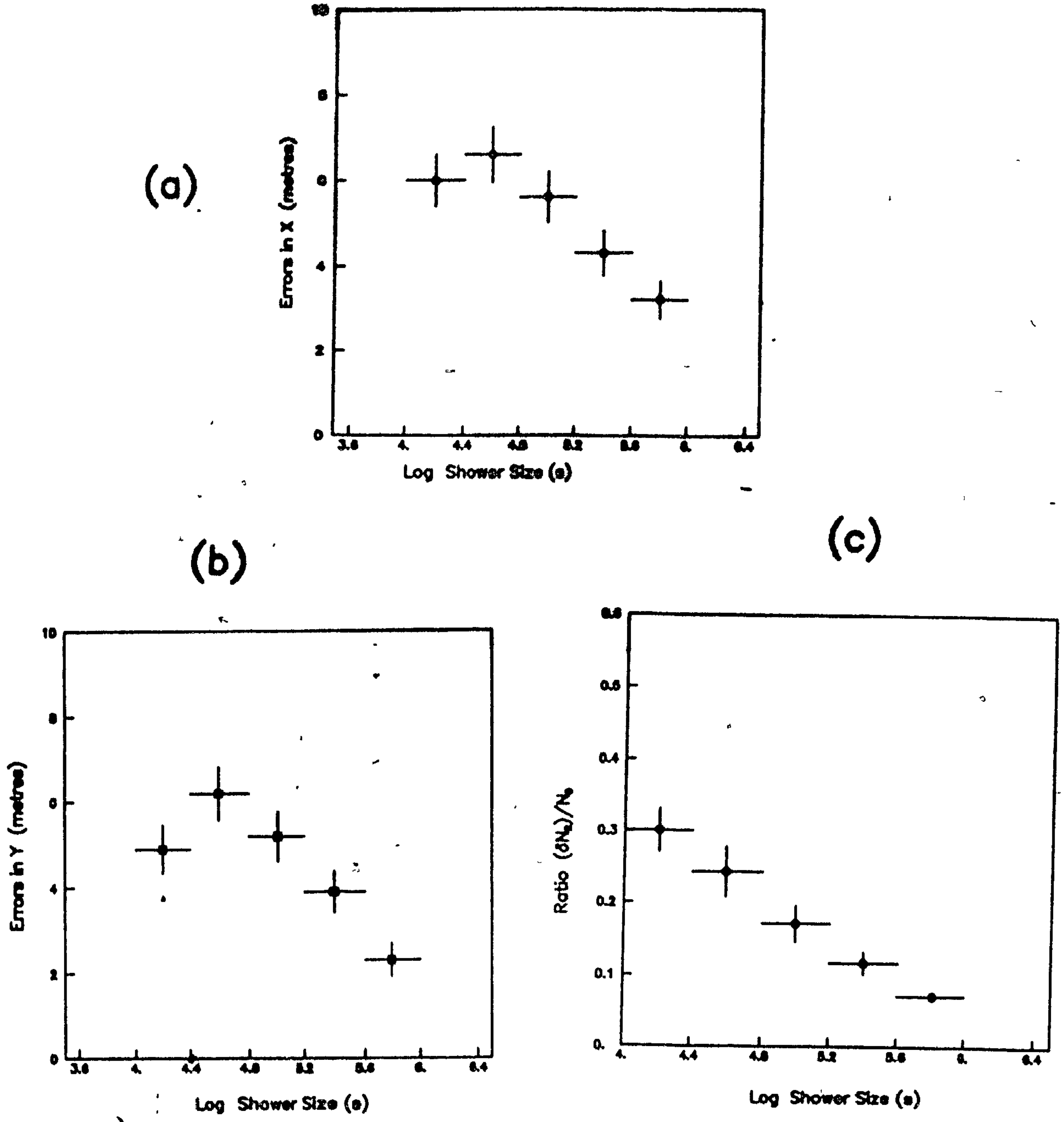

FIG 4.17: Estimation of the errors in the three fitted parameters obtained by the method described in section 4(a). (a) The error in X; (b) the error in Y; (c) the ratio of the error in N/δN, and N are plotted as a function of the shower size.

array was 100% efficient at low energies. So the raw shower size spectrum shown in figure 4.16 has to be corrected for the efficiency of the array to obtain the real spectrum. The efficiency corrected flux is shown in figure 4.18.

The differential size spectrum is defined as the number of showers per unit time, per unit solid angle, per unit area that had a size between N and N+dN. Since only showers with zenith angles less than 30° are accepted during analysis, the total solid angle for the array is a constant. The area of the array should be so chosen that any shower that falls within that area has practically 100% chance of being accepted. Since the number flux is corrected for the array efficiency this means that any shower that falls within a radius of 50m from the array centre has would meet this condition. So the effective acceptance area of the array is $\pi \times 50^2\, m^2$. The total time for which data was collected is calculated separately for each block of data by summing the time intervals between events . These are distributed according to

$$n(t) = C\, exp(\frac{-t}{\tau})$$

where $n(t)$ represents the frequency of events, t the time interval since the last event, τ the event rate and C a constant as shown in figure 4.19. This is expected from probability theory and indicates that there are no problems with data collection. The differential number spectrum is obtained by dividing the corrected flux shown in figure 4.18 by the product of the area, the total time and the total solid angle. Figure 4.20 shows the differential number spectrum for the data analysed. The conversion from number spectrum to energy spectrum was obtained by us by re-scaling the size spectrum by 10^{10}. However, this conversion may not be exact since the relation between shower size and its energy is not as simple as we assume. Figure 4.21 shows the differential

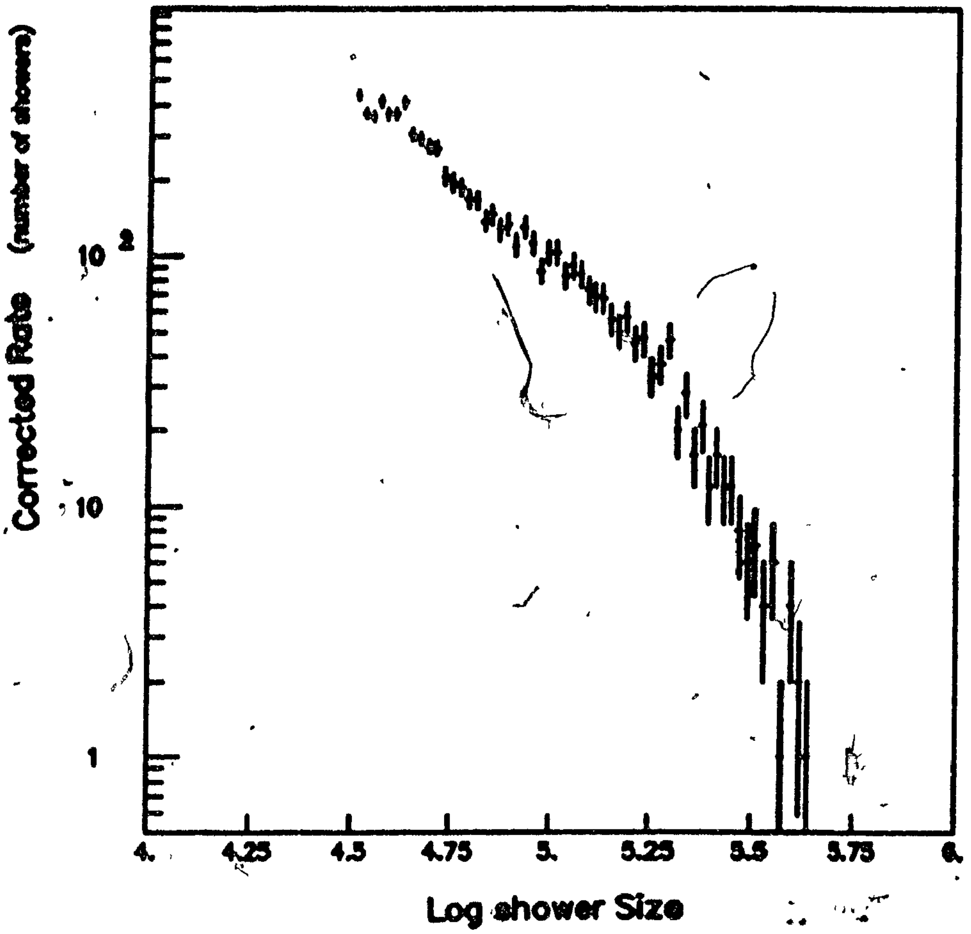

FIG 4.18: The efficiency corrected shower size flux. The units of rate are total number of showers observed. The binwidth along the abscissa is again .02 in the log scale.

energy spectrum corresponding to figure 4.20. The integral size (energy) spectrum is defined as the number of showers per unit time, per unit area, per unit solid angle that had size (energy) greater than N (E). Figure 4.22(a) and (b) show the integral size and energy spectra that correspond to differential spectra shown in figures 4.20 and 4.21 respectively.

Section 4(f): Discussion of Results

The differential spectra shown in figures 4.20 and 4.21 show evidence of the 'knee' discussed in section (e) of chapter 1. The slope γ of the spectrum below $N=10^{5.125}$ in figure 4.20 has a value of 2.11; above, γ changes to 3.06. The slopes of the spectra above and below the knee are in the same range as the slopes obtained by the Sydney group[18] and the Durham[17] and the change in the slope is consistent with the expected slope. The differential size spectrum obtained by the Sydney group has a slope of 2.14±.04 below the knee and a slope of 2.91±.08 above the knee. The differential flux obtained by us is a factor of ~2 smaller than the flux obtained by that group.

There could be several reasons for these differences. During analysis, no compensation is applied for saturated counters. The ADCs overflow at a count that corresponds to around 15 particles. In effect, a counter that is populated with more than 15 particles, during analysis is considered as having received only 15. A shower that is incident directly on a counter or very close to it could populate that counter with enough particles so as to cause the ADC to overflow . The loss of information would result in a smaller shower size being fitted, provided all the cuts are still passed. A more subtle saturation effect is where the photo tube goes non linear at high light levels. This has not yet been studied in detail for our counters.

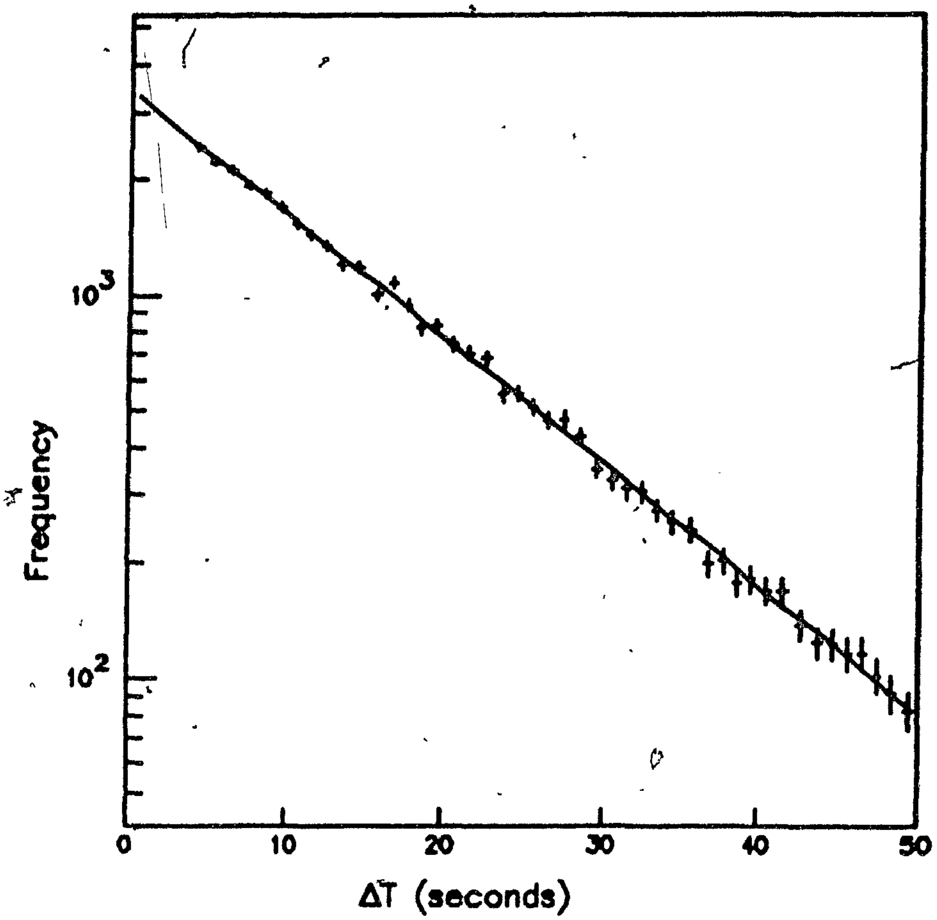

FIG 4.19: A histogram of the time elapsed since the last shower as recorded by the data collection program. The ordinate axis is logarithmic. The ΔT distribution should follow an exponential distribution if the data collection is normal.

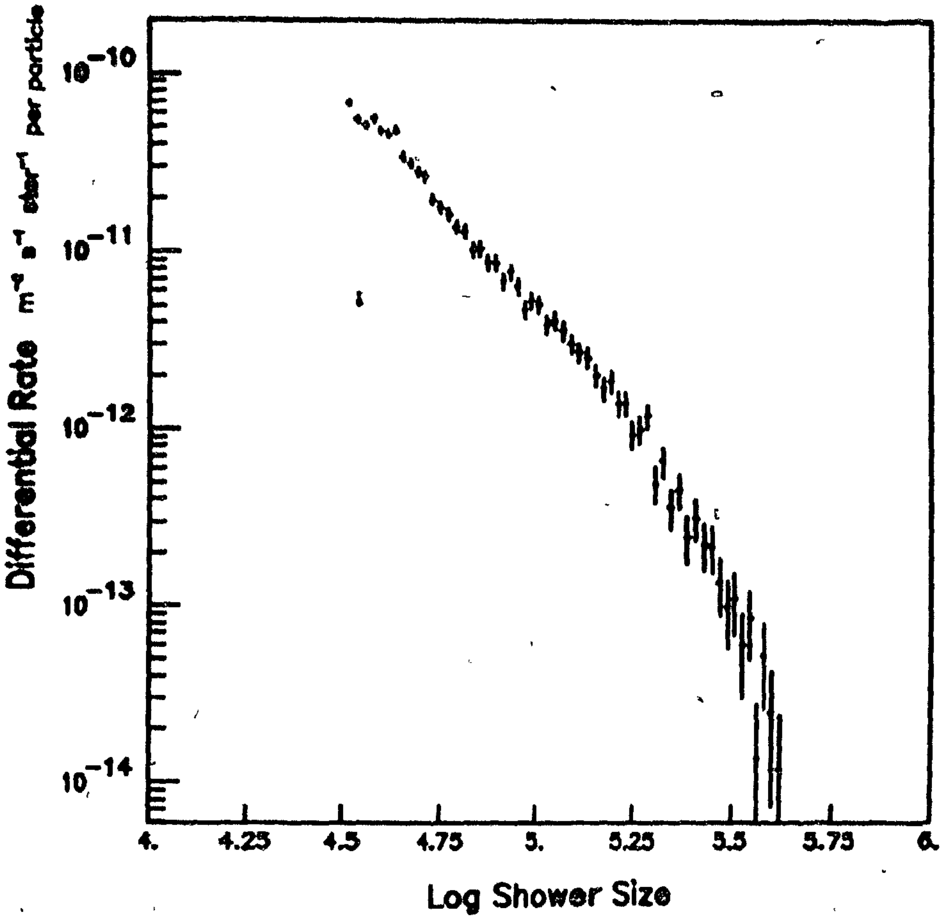

FIG 4.20: Differential size spectrum obtained from analysis of shower data. The ordinate axis shows the number of events per unit area, per unit time, per unit solid angle, that had sizes between log N and log N+dlog N where dlog N in this case is the corresponding bin size (.02) of the histogram.

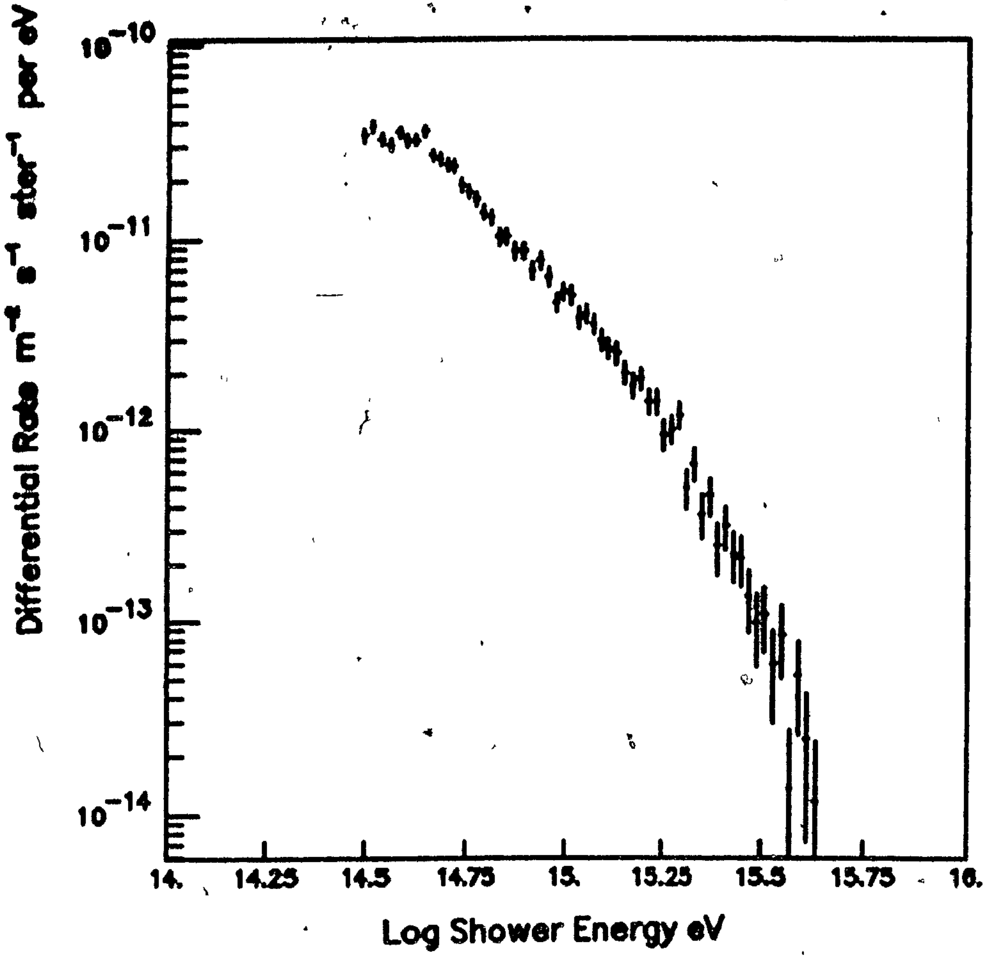

FIG 4.21: Differential energy spectrum corresponding to the differential number spectrum shown in the previous figure. The relation $E=10^{10}\times N$ is assumed.

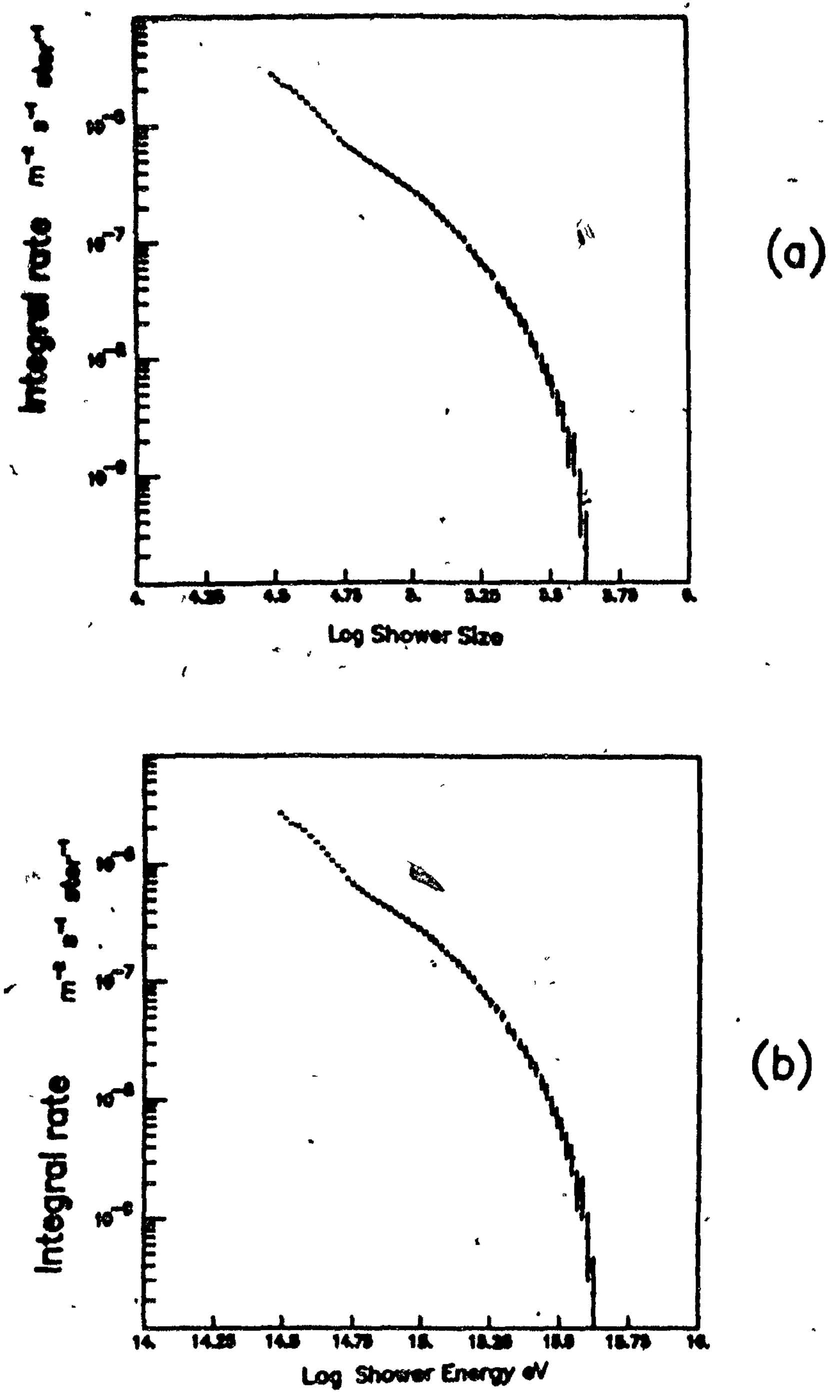

FIG 4.22: (a) The integral shower size spectrum (b) The integral energy spectrum of cosmic rays obtained from the LEDA array.

During the conversion of raw flux data to number spectrum, the solid angle of the showers is taken as a constant assuming a flat distribution in $\cos\theta$. This is only an approximation as there is some variation expected over this larger $cos\theta$ range. Ideally, the weighting factor for each bin in $\cos\theta$ should be calculated separately by estimating the effective solid angle for that bin. A preliminary result obtained by having a higher cut on $\cos\theta$ instead of the cut of .866 (so that the assumption of no $\cos\theta$ variation is more valid) has shown higher flux than that shown in figure 4.20. Again, the effect of the dead time of the electronics has been ignored in obtaining the spectra. This factor, however is not negligible and would change the spectra if taken into consideration.

Figure 4.23 is plots of the differential size spectrum showing data points for the Sydney group along with the data points obtained from the LEDA array (altitude 43 metres above sea level). Though the flux obtained is lower than expected, the spectra obtained from the array shows a a general agreement on the discontinuity of the slope.

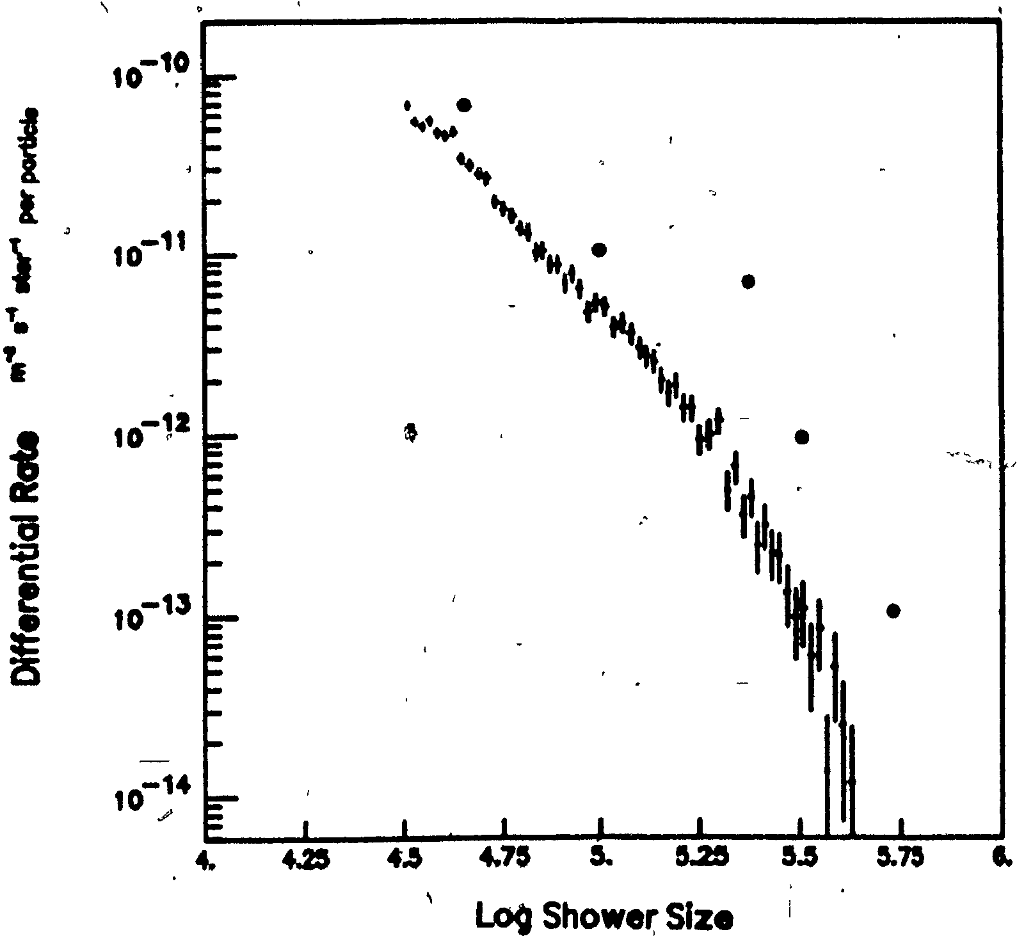

FIG 4.23: The differential size spectrum of cosmic rays obtained from the LEDA array compared with the spectrum obtained from the Sydney Air Shower Array[18]. Binwidth along the x-axis is .02(log scale).

5. CONCLUSIONS

The purpose of this study was to test the performance of the LEDA array as a calorimeter. Preliminary results are promising. The energy resolution of the array ranges from .3 to .05 over the energy range from $10^{14.5}$ to $10^{16.0}$. The remarkable similarity between the predicted and the actual resolution of the array is an indication of the quality of the fitter. The angular resolution of the array is estimated between to be of the order of 1°.

The present fitting program though accurate, is not capable of parameterising the shower age. The effect of the shower age is make the lateral distribution flatter in R and this would certainly improve the quality of the fits obtained. The shower age is an important parameter and there is definitely some loss of accuracy when it is not taken into account. Another important factor is the triggering deadtime. Present analysis doesnot correct for loss due to finite triggering deadtime of the electronics discussed in chapter 3. Correction for this factor would change the time factor in the calculation of the differential and the integral spectra and would result in an overall change in the flux. The deadtime problem is presently under study.

The difference in the fluxes observed by other experiments and by us is a function of the several parameters discussed in the last chapter. Preliminary results of data analysis done with a higher cut on $\cos\theta$ has shown an increase in the low energy flux, showing that the assumption of a flat distribution in $\cos\theta$ when $\theta < 30°$ is not necessarily true. This is definitely one of the problems that requires a more detailed investigation. It is also important to integrate into the fitting routine, a subroutine to compensate for saturation of the ADC. This factor could account partly for the low flux at high energies.

There are several steps that could be taken to improve the performance of the array. The low efficiency for small shower sizes can be increased by increasing the detector density near the centre of the array. The single particle spectrum plays an important role in the conversion of ADC counts to particle number. The reliability of these conversions depends upon the frequency with which the SPL data are collected. The most reliable method to estimate of the SPL mean with the use a of a laser source and fiber optic cables to connect the photo tubes to the recording electronics. Such an arrangement combined with a laser filter, could also be used to determine the gain of the photo multiplier tubes accurately hence to achieve higher accuracy in data conversion. A less expensive way of achieving the same goal would be calibrate each detector separately with a pulsed laser. The most inexpensive proposition would be the installation of the required electronics to the enable SPL data collection to be automated.

REFERENCES

[1] Baltrusaitis, R.,M. et al., Phys. Rev. Lett.(USA),(1985), **54**, 1875-7

[2] Hess, V. F., Phys. Zeits., (1911), **12**, 998.

[3] Rossi, B., Proc. Int. Conf. Phys., (1935), **I**, 238.

[4] Clay, J., Proc. Amsterdam, (1927), **30**, 1115.

[5] Shapiro, M. M.,(ed), Composition and Origin of Cosmic rays,(1983), 47-64.

[6] Shapiro, M., M.,(ed), Composition and Origin of Cosmic rays,(1983), 1-24.

[7] Julisson,E.,Meyer,P., Müller, D.,Phys Rev Lett, 29 1972 (445-448)

[8] Gibbs, G. B., NIM, (1988), **A264**, 67-73

[9] Weekes, T. C.,NIM, (1988), **A264**, 55-63

[10] Blatrusaitis, R. M., et. al,NIM ,(1988),**A267**, 87-92,

[11] Kevins, P., et al., Sci. Am.,(1985), **253**,no.5, 60

[12] Kamata ,J.,et al , Progr Theoret. Phys. (Koyoto),(1958), **Suppl. 6**, 93-100.

[13] Nishimura,J., Handbuch der Physik,(1967), **46/2**,1967, 1.

[14] Cocconi, G., Handbuch der Physik,(1967),**46/1**,1967, 215-.

[15] Griesen, K., Progr, in Cosmic Ray Physics,(1956), **II**, Chap.I.

[16] Hayakawa, S., Cosmic Ray Physics, Publishers John Wiley and Sons.

[17] Rada, W. S.,et al., NIM, (1977), **145**, 283-287,

[18] Sun, L., et al., NIM, (1984), **223**, 173-179

[19] Hillas, A.M., Phys. Rep.(Section C of Phys Lett) (1975), **20**, no 2, 59-136

[20] Shapiro., M. M.,(ed), Composition and Origin of Cosmic Rays, (1983),125-148

[21] Bell et al, J. Phys, (1974), **A7** 420-436)

[22] Personal communication from Bicron.

[23] Grieder, P. K. F., NIM, (1967), **55**, 295-300.

[24] Mead, J. B., et al., NIM, (1965), **36**, 13-228

[25] Clay, W., Gregory, A. G., NIM, (1978),**153**, 467-471

[26] Gibbs,K. C., NIM, (1988),**A264**, 67-73.

[27] Timing Capabilities of the LEDA cosmic ray detector; Masters Thesis by Bultena, S., (1988) McGill University

[28] Poirier, J., NIM, (1987), **A267**, 280-82.

[29] Smith, A. C., NIM, (1977), **A260** 289-293

[30] Brennan, M. H., et al., NATURE, (1958), **4640**, 905-911